DISSERTATION

STRENGTH ANALYSIS AND COMING OUT OF STEEL SHAFT

FOR CERAMIC ROLLER USED IN THE FURNACE UNDER

BOTH THERMAL AND DISTRIBUTED LOADS

DEDI SURYADAI/12584108

KYUSHU INSTITUTE OF TECHNOLOGY

2015

DISSERTATION

STRENGTH ANALYSIS AND COMING OUT OF STEEL SHAFT
FOR CERAMIC ROLLER USED IN THE FURNACE UNDER
BOTH THERMAL AND DISTRIBUTED LOADS

By
Dedi Suryadi
(Student Number: 12584108)

Supervisor: Prof. Nao-Aki Noda

Kyushu Institute of Technology
Graduate School of Engineering
Department of Mechanical Engineering
2015

Acknowledgements

First of all, I would like to give the ultimate thanks to Allah the almighty for everything He has given in my life.

In this time, I would like to express the deepest appreciation to my supervisor Professor Nao-Aki NODA for his guidance, encouragement, and support and for helping me complete my work. His helpful suggestions have meant a lot to me and to my research. His support gave me the inspiration to complete this doctoral research. I also want to thank Dr. Yoshikazu SANO for his kind help and support through the last three years and for his advice for this study.

The contributions and insightful observations of my committee members, Prof. Kenji MATSUDA, Prof. Kenji KOUSA, and Prof. Koju HIRAKI, are also most appreciated and acknowledged. Also, I would like to thank Dr. Yasushi TAKASE for his help during my research work. Special thanks to all of Kyushu Institute of Technology's professors and administrative staff with whom I have had the opportunity to take courses. I would also like to thank all Fracture Mechanics and Elasticity lab-mates, all MAKITA members, and all those who have helped me carry out my work.

I want to express my sincere gratitude to *my wife and my family* who have given me great continuous support, time and encouragement more than I need throughout my years of study.

Kitakyushu, 7 September 2015

Dedi Suryadi

Abstract

Advanced ceramic material has been introduced as a discipline only during the last 40 years. Recently, ceramic is widely used for large structural because of outstanding properties such as high wear resistance, high corrosion resistance, and high temperature resistance. In this study, the ceramic roller is considered to be used in the furnace whose temperature is more than $1,000^{o}C$. Here, the roller consisting of ceramics sleeve is connected to steel shaft.

First, suitable joint selection for ceramic roller is discussed in detail. Since ceramic have hard-formability and brittleness, ceramic should be used combining with other material. Here, three types of joints are considered, namely, adhesive bonding as Model 1, metal bonding as Model 2, and shrink fitting as Model 3. For Model 1 and Model 2, interlayer material is necessary to be considered to bond ceramic sleeve and steel shaft. Interlayer material used for Model 1 is epoxy, and the one for Model 2 is BA03/WC. For Model 3, ceramics sleeve and steel shaft are assumed to be connected with small shrink fitting ratio. Each model is investigated under room temperature and high temperature by finite element model analysis. Then, the maximum stress appearing at the joint for each model is evaluated. It is found that all types of joints can be used at room temperature. However, under high temperature, only the shrink fitting joint can be used.

Next, a new ceramic roller structure used in the heating furnace is discussed. Attention should be paid for the risk of fracture due to the thermal expansion of the steel shaft that is much larger than the one of ceramic. To consider the thermal stress approximately, a simple double cylinder roller consisting of outer ceramic and inner

steel is considered. The results show that the maximum stress can be reduced by using the small thickness of the steel shaft. Next, real roller is analyzed. The results show that the maximum tensile stress can be reduced by using tapered thickness shaft because of the smaller rigidity at the high temperature portion. It is also found that the plastic deformation of the shaft does not appear for the short tapered shaft. Finally, an application of ceramic roller to a real furnace in a steel manufacturing company is considered. It is found that tapered shaft geometry with high chrome steel can be used in a real furnace.

Failure analysis if performed for coming out of the steel shaft from ceramic sleeve, which is connected by shrink fitting. Since the ceramic sleeve is brittle, only low shrink fitting ratio can be applied. The coming out behavior of the roller during rotation is analyzed by the finite element method. The roller rotation is replaced by shifted load in the circumferential direction on the fixed roller. It is found that the load rotation can be approximated by the discrete load shifting at the interval angle $\theta_0 = 12^o$ within 1% error. The effect of the shrink fitting ratio on the coming out of the shaft is discussed as well as several other parameters, such as Young's modulus of the shaft, the friction coefficient, magnitude of the load, and geometry of the shaft. The results show that the coming out of the shaft appears under smaller shrink fitting ratio $\delta/d \leq 0.2 \times 10^{-3}$ and does not appear under larger shrink fitting ratio $\delta/d \geq 0.4 \times 10^{-3}$. Also, the coming out happens easily for smaller Young's modulus of the shaft $E_{sh} \leq 100$GPa, smaller friction coefficient $\mu \leq 0.1$, and larger distributed load $w \geq 45$N/mm. The speed of coming out can be prevented by increasing the shaft thickness t $\geq$ 20mm and contact length L $\geq$ 300mm.

Table of Contents

Title page

Acknowledgments

Abstract

Table of Contents

List of Figures

List of Tables

Nomenclature

1. Introduction

2. Ceramic/Steel Joint Selection for the Ceramic Roller Used under Room Temperature and High Temperature

3. Proposal for New Hearth Roller Consisting of Ceramic Sleeve and Steel Shaft Used in the Heat Treat Furnace

4. Failure Analysis for Coming out of the Shaft from Shrink-fitted Ceramic Sleeve

6. Summary

List of Figures

List of Table

Nomenclature

Roman symbols

d   inner diameter of the sleeve [mm]

T   sleeve thickness [mm]

t   shaft thickness [mm]

L   contact length [mm]

w   distributed load on the roller surface [N/mm]

a   outer diameter of the sleeve [mm]

b   inner diameter of the sleeve [mm]

N   number of cycle

Esl   Young's modulus of the ceramic sleeve [GPa]

Esh   Young's modulus of the steel shaft [GPa]

uzA   displacement at point A [mm]

uzC   displacement at point C [mm]

h   thickness of inner cylinder

L/d   fitted length ratio

T(z)   Temperature along contact position of shaft

Greek symbols

δ Diameter difference [mm]

ρ Mass Density [kg/m^3]

v Poisson's ratio

μ Friction coefficient

δ/d Shrink fitting ratio

θ_0 Interval of load shift angle in the simulation

σ_r Radial stress on the contact part [MPa]

σ_θ hoop stress on the contact part [MPa]

$\sigma_{\theta solid}$ hoop stress on the contact part for solid inner cylinder [MPa]

τ_{rz} Shear stress at z-direction [MPa]

σ_{al} allowable stress of the ceramics

$\sigma_{\theta max}$ maximum hoop stress

$\sigma_{\theta s}$ hoop stress due to shrink fitting

$\sigma_{\theta b}$ hoop stress due to distributed load

$\sigma_{\theta a}$ stress amplitude [MPa]

$\sigma_{\theta ave}$ average stress [MPa]

$\sigma_{0.2}$ 0.2% proof stress for SCM415

Chapter 1

Introduction

1.1   Background

Advanced ceramic has attracted attention in wide engineering fields in the last five decades [1-4] because ceramic has some advantageous properties such as high temperatures resistance, high melting point, high hardness, and high compressive strength [5]. The usage of advanced ceramic for engineering applications has been promoted since 1970s as electrical insulator [4], automotive engines [6-10], tribology components [11, 12], cylinder head plates, pistons and turbocharger rotors [13, 14], gas turbine engines[15, 16], machine tools [17], hot rolling mills and low-pressure die casting machine. However, under both thermal and mechanical loadings, structural ceramic is not very popular until now compared to functional ceramic widely used [18]. As an example, intense efforts have been done to develop ceramic gas turbine during 1950s-1990s [15, 16], but only ceramic coatings are in use now. This is because all ceramic components may be too brittle to design turbine component. Generally speaking, the manufacturing and processing technologies of advanced ceramic have progressed very relatively slowly.

Recently, advanced ceramic applications subjected to thermal and mechanical loads have been studied by several authors. Study on treatment of molten metal, ceramic die cast sleeves and ceramic stalks in the low-pressure die casting machine have been successfully carried out [19-22]. Similar ceramic structures under high temperature environment in continuous galvanizing line [23, 24], in the continuous pickling line [25, 26], and in the heating furnace [27] have also been considered.

In this thesis, we will focus on hearth rollers used in the heating furnace whose atmosphere temperature is more than 1,000°C. Conventional rollers have ceramic coated steel sleeve and shafts connected each other by shrink fitting. Although the inside of the roller is cooled by water circulation to reduce the temperature, the roller coating deteriorates in short period due to the thermal expansion difference between ceramic and steel. Then, finally, the conventional rollers are changed very frequently because of the wear induced by the hot conveyed strips. Therefore, a new roller consisting of ceramic sleeve and steel shafts at both ends will be considered. All ceramics sleeve may prevent most of defects observed at coated ceramic, which can extend the roller life.

In this thesis, in chapter 2, appropriate joint selection will be investigated for ceramic sleeve and steel shaft. Here, ceramic sleeve is assumed to be joined to steel shaft. The major problem in ceramic/metal joints is different thermal expansion coefficient at high temperature. The thermal stress often causes not only low strength in bonded joint but also a fracture in the ceramic. Even though shrink fitting joint has been discussed for ceramic roller [28-30], application for other types of joints was not considered previously. Therefore, in this study, three types of joints will be compared, namely, adhesive bonding, metal bonding, and shrink fitting.

In chapter 3, the ceramic sleeve roller will be considered focusing on thermal and bending stress at joint portion. Here, ceramic sleeve is connected to steel shaft by shrink fitting. Effects of roller geometry and the material difference will be considered in order to reduce the thermal stress and mechanical stress. Finally, the most suitable geometry and materials will be proposed by considering the use at steel manufacturing machinery.

In chapter 4, the coming out behavior of the steel shaft from the ceramic sleeve

will be considered during operation because only low shrink fitting ratio can be applied

for those structures. Previously, Truman and Booker investigated micro-slipping

between the gear hub and shaft connected by shrink fitting [31]. Antony analyzed

contact separation for rotating thermos-elastoplastic shrink fit assembly [32]. However,

few failure studies are available for coming out of the shaft from the shrink-fitted

ceramic sleeve. The finite element method is applied to simulate the coming out

behavior. Then, several mechanical factors will be considered to understand the coming

out of the shaft.

1.2   Classification of advanced ceramic

Advanced ceramic such as alumina, aluminum nitride, zirconia, silicon carbide,

silicon nitride and titania-based materials, each with their own specific characteristics,

offer a high-performance, economic alternative to conventional materials such as glass,

metals and plastics. Physical properties such as hardness, strength, wear resistance,

corrosion resistance and thermal stability are considered while choosing a material.

Each of these can be optimized depending on the choice of material.

There are five important classes of advanced ceramic for large structure as

follows [10].

1. Alumina ceramic (Al_2O_3)

Alumina Ceramic is the most widely used fine ceramic material. This material

offers a combination of good mechanical and electrical properties such as high electrical

insulation, high mechanical strength, high wear and chemical resistance. Its high

dielectric properties are beneficial in electronic products. Alumina can be formed using

several ceramic processing methods and can be processed machined or net-shaped to

produce a variety of sizes and shapes. Furthermore it can be readily joined to other ceramics or metals using specially developed metallizing and brazing techniques. Alumina ceramic is often classified into high alumina (80% alumina oxide) and porcelains (having less than 80% aluminum oxide). High aluminas are used in many mechanical devices and electronics. Strength and other properties generally improve as the percentage of alumina is increased.

2. Zirconia ceramic (ZrO_2)

Zirconia oxide has the highest strength and toughness at room temperature of all the advanced ceramic materials. The fine grain size allows for extremely smooth surfaces and sharp edges. Zirconia offers corrosion and chemical resistance at high temperatures above the melting point of Alumina. Zirconia exist in three different crystal structures such as monolithic (stable at room temperature and become up to about 1170^0C), tetragonal (stable up to 2370^0C) and cubic. Three types of zirconia ceramic used in the technical applications are cubic, partially stabilized and tetragonal zirconia. Cubic zirconia has low fracture toughness and strength. Partially stabilized zirconia (PSZ) has larger fracture toughness. Tetragonal zirconia has highest toughness and strength compared to cubic and partially stabilized zirconias.

3. Sialon ceramic (SiAlON)

SiAlONs are ceramic alloys based on the element silicon (Si), aluminium (Al), oxygen (O), and nitrogen (N) to solve the problem of silicon nitride (Si3N4) being difficult to fabricate. The combination of silicon nitride and aluminum oxide produces a material with the excellent strength, hardness, fracture toughness and low thermal expansion of silicon nitride, enhanced by corrosion resistance, good high temperature strength and oxidation resistance imparted by the aluminum oxide.

4. Silicon carbide ceramic (SiC)

Silicon carbide has the highest corrosion resistance of all the advanced ceramic materials. It also retains its strength at temperatures as high as 1400°C and offers excellent wear resistance and thermal shock resistance. Silicon carbide is formed in two ways, reaction bonding and sintering. The advantage of silicon carbide for reaction bonded is low cost, and the other side, silicon carbide for hot pressed is high strength but high cost for finished components, which is due to the difficulty in machining process. Advantage of sintered type is that most of the machining can be used easily. Reaction bonded SiC is made by infiltrating compacts made of mixtures of SiC and carbon with liquid silicon. Sintered SiC is produced from pure SiC powder with non-oxide sintering aids. Conventional ceramic forming processes are used and the material is sintered in an inert atmosphere at temperatures up to 2000ºC or higher.

5. Silicon nitride ceramic (Si_3N_4)

Silicon nitride ceramic is superior to other ceramic materials due to its thermal shock resistance. It also offers an excellent combination of low density, high strength, low thermal expansion and good corrosion resistance and fracture toughness. Silicon nitride ceramic is produced in two main ways; reaction bonded silicon nitride (RBSN), and hot pressed silicon nitride (HPSN) and sintered silicon nitride (SSN). RBSN is made by direct reacting compacted silicon powder with nitrogen, and produces a relatively low-density product compared with hot pressed and sintered silicon nitride, however the process has only a small volume change allowing net shape forming. The HPSN and SSN material is made with sintering aids and offers better physical properties suitable for more demanding applications. Among non-oxide ceramic Si_3N_4 has been most widely studied based on its natural exhibit a potential up to temperature

Table 1.1 Mechanical and physical properties of advanced structural ceramic [10]

Material	Density (g/cm^3)	Flexural strength (MPa)	Fracture Toughness (MPa.m$^{1/2}$)	Elastic Modulus (GPa)	Poisson's ratio	Hardness (GPa)	Thermal expansion coefficient (1/K)	Thermal conductivity (W/mK)
Silicon nitride								
sintered	3.2	600	4.5	276	0.24	14	3.4	28
hot pressed	3.2	800	5.0	317	0.28	20	3.2	30
reaction bonded	2.5	210	3.6	165	0.22	10	2.8	6
sintered reaction bonded	3.3	825	-	297	0.28	19	3.5	30
HIPed	3.2	1000	6.0	310	0.28	20	3.5	32
Sialon	3.2	650	5.0	297	0.28	18	3.2	22
Silicon carbide								
Hot pressed	3.2	550	3.9	449	0.19	25	4.5	70
Sintered	3.1	400	3.0	427	0.19	27	4.8	80
Reaction-bonded	3.0	350	3.5	385	0.19	17	4.4	90
CVD	3.2	500	2.6	450	-	30	5.5	150
Alumina (%)								
85	3.4	296	3.5	221	0.22	10	5.3	15
90	3.6	338	3.5	276	0.22	11	6.1	17
96	3.7	352	4.5	303	0.21	12	6.3	23
99.8	3.9	552	4.5	386	0.22	15	7.1	30
Zirconia								
Cubic	5.9	245	2.4	150	0.25	11	8.0	1.7
TZP	6.1	1020	11.0	210	0.24	13	10.6	0.4
PSZ	6.0	750	8.1	205	0.23	12	8.3	2.1

of 1,500^{o}C [33]. In this present research, Si$_3$N$_4$ will be used.

1.3   Mechanical and thermal properties of ceramic

Table 1.1 shows the mechanical and thermal properties of ceramic [10]. Brief explanation on the properties of ceramic is provided as follows.

1. Hardness and elasticity

Hardness of ceramic is normally expressed by the size of the indent made by pressing a diamond indenter against the ceramic surface. When a solid is stressed (force/area), the solid is deformed in accordance with Hooke's law, which is expressed

as (stress) = (elasticity) × (deformation). The elasticity (Young's modulus, E) is obtained by dividing the stress by the deformation (elongation/length). The hardness of material relates to resistance of material to abrasive wear. Because of their high hardness, ceramic is suitable for application requiring resistance to abrasive and erosive wear.

2. Strength

The theoretical strength of a material is expressed by the force required to separate the atoms that constitute the material. The strength of ceramic intended for structural materials ranges from 400 to 800 MPa. The actual strength of materials is lower than the expected values because the stress is concentrated at defects (cracks) inside the material. The strength decreases as the size of the defect increases. Defect sizes are statistically distributed in materials. Therefore, the strength of a material varies and is evaluated statistically (Weibull distribution). The strength of a material is expressed accurately by the mean value or the Weibull distribution function obtained by testing many samples to failure. The strength is classified into bending strength, tensile strength, and compressive strength, which are measured by different methods.

3. Fracture toughness

Materials contain defects (cracks) and the material fracture is caused by the stress concentrated at the tip of a crack. The value of the stress concentration is expressed by the stress intensity factor K. The crack starts to extend rapidly, leading to breakage, when K reaches a certain value. The value at this point is the critical stress intensity factor or the fracture toughness value K_C, which expresses the toughness (or fragility) of the material. Stress s at this point is the fracture strength (strength) of the material.

Strength depends on the length and shape of the crack as well as the fracture toughness value.

4. Specific heat capacity

A solid material, when heated, experiences an increase in temperature signifying that some energy has been absorbed. The summation rules of specific heat capacities of oxides are applicable in an approximate sense to multiple oxides over a wide range of temperatures while not being limited to high temperatures. In actual materials, thermal changes due to property changes such as thermal vibration, defect formation, electron thermal excitation and phase transition properties affect the change in heat capacity, and therefore, precise measurements and analyses are performed.

5. Thermal expansion.

The expansion of substances responding to temperature change is characterized by the coefficient of thermal expansion. When an interatomic potential develops in a material becomes asymmetric, thermal expansion occurs responding to the temperature increase. Ceramic materials that are to be subjected to temperature changes must have coefficients of thermal expansion that are relatively low, and in addition, isotropic. Otherwise, these brittle materials may experience fracture as a consequence of non-uniform dimensional changes in what is termed thermal shock. When various components consisting of difference materials are subject to changes in temperature, design specifics need to be considered due to differences in thermal expansion.

6. Thermal conductivity

Thermal conductivity values for a number of ceramic materials range between approximately 2 and 50 W/m-K. Porosity in ceramic materials may have a dramatic influence on thermal conductivity; increasing the pore volume will, under most

circumstances, result in a reduction of the thermal conductivity. In fact, many ceramics that are used for thermal insulation are porous. Heat transfer across pores is ordinarily slow and inefficient. Internal pores normally contain still air, which has an extremely low thermal conductivity—approximately 0.02 W/m-K.

1.4   Review on ceramic rolls structures

The use of ceramic tube for die casting has been studied by some authors [19-22]. In 2005, the using ceramic tube (stalk) for low pressure die casting was proposed by Bonollo et al. [19]. Here, a technical and economical term of low pressure die casting was considered. Low pressure die casting was characterized by several advantages, including high yield, excellent control of operative parameters, good metallurgy and technology quality. However, ceramic tube effect in the die casting was not studied sufficiently.

Next, Noda et al. studied on the thermal stress for ceramic stalk in the low pressure die casting machine in 2009 [20], and for ceramic stalk having protuberance dipping into molten metal in 2010 [21]. Previously, the tube was made of cast iron resulted in spoiling the quality of product because of the partial melting of molten metal. Therefore, ceramic tube was proposed to improve the life time. The thermal stress was investigated when the tube was dipped into the crucible by varying dipping speeds and dipping directions. It was found that for vertical tube with or without protuberance, dipping slowly may be suitable to reduce thermal stress because dipping fast causes large temperature difference in the thickness direction, which results in large thermal stresses. However, for horizontal tube, dipping fast may be suitable to reduce thermal

stress even though it causes larger temperature difference in the thickness direction of the tube. Moreover, since the molten metal cannot flow into the stalk with protuberance very much, the inner heat transfer coefficient α of stalk with protuberance is much lower than the inner α of simple tube.

Moreover, Ryan [22] studied on how to reduce thermal stress of ceramic tube for low pressure die casting. It is found that managed pre-heating is shown to best reduce stress in the riser tube, with a preheat temperature of 350C or greater predicted to protect the tube from damage during insertion in the melt and the critical initial cast. Thermal stress for all ceramics rolls used in molten metal was also investigated by Noda et al. [27]. The best way to reduce thermal stress on the ceramic roller is obtained. First, the thermal stress in hollow cylinder can be reduced by dipping them into molten zinc fast u=25mm/s. Second, for solid cylinder, the thermal stress could be reduced by dipping into molten zinc slowly.

Noda et al. [28] successfully conducted research on ceramic roller used in the hot rolling mills. Here, a ceramic sleeve and two short solid shafts were connected by shrink fitting whose inner diameter of sleeve d=210mm. Ceramic roller was considered under room temperature. The results shows that for large shrink fitting ratio $\delta/d \geq 2.0 \times 10\text{-}3$, the stress due to distributed load $\sigma_{\theta b}$ becomes constant independent of δ/d. as shown in Figure 1.1. The constant value coincides with the results when the sleeve and shafts are perfectly bonded. In other word, if $\delta/d \geq 2.0 \times 10\text{-}3$, the sleeve and shaft can be treated as a unit body.
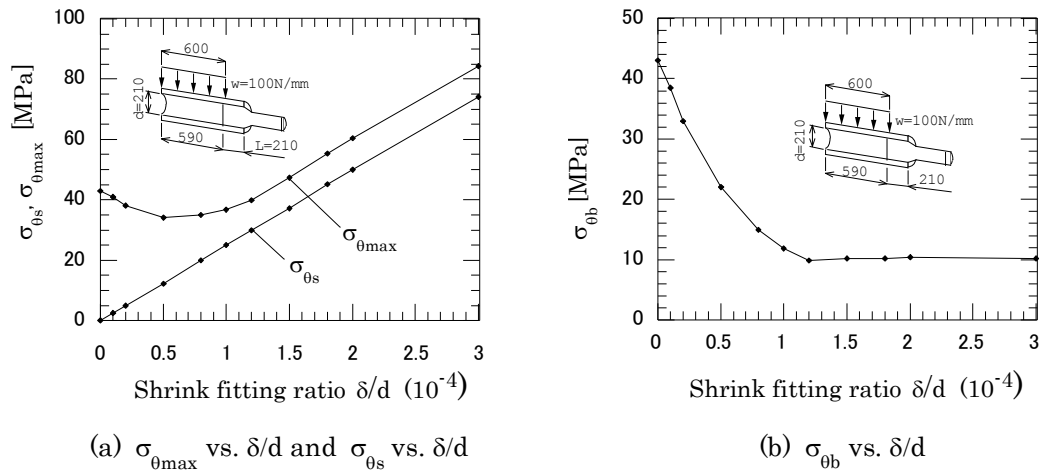
(a) $\sigma_{\theta max}$ vs. δ/d and $\sigma_{\theta s}$ vs. δ/d (b) $\sigma_{\theta b}$ vs. δ/d

Figure 1.1 σ_θ vs. δ/d when L=210mm

($\sigma_{\theta max} = \sigma_{\theta s} + \sigma_{\theta b}$, $\sigma_{\theta s}$=stress due to shrink fitting, $\sigma_{\theta s}$=stress due to distributed load)

Application of large ceramic structures to steel manufacturing machinery is suitable for several steel manufacturing rolls [25 and 26]. Here, new roll structure used in the continuous pickling line was considered. Some steps have been carried out including static strength analysis as well as fatigue strength analysis for ceramic rolls.

Besides stress analysis for large ceramic structures, separation conditions for shrink fitting system used for ceramic roller in hot rolling mills was also analyzed because steel shaft sometimes has to be exchanged for reconstruction [29]. It is found that the separation time becomes shorter if the atmosphere temperature went up more quickly. Generally, the separation time was influenced by several factors such as shrink fitting ratio, outer diameter of the sleeve, thickness of the fitted shaft and fitted length. Thermal stress was also indicated in this study by Li et al [30].

1.5   Objectives and scope of the present work

The objectives of this research are: (1) to select appropriate joint for

ceramic/metal roller, (2) to design ceramic roller used in the heating furnace, and (3) to investigate effect of the shrink fitting ratio on the coming out of the shaft from the ceramic sleeve as well as some other parameters. The scope of the present work will be carried out through following stages.

The first stage is study on ceramic sleeve/steel shaft joint subjected to both bending load and thermal load. Since it is impossible to use ceramic for whole body because of their low toughness, ceramic sleeve must be joined to other material such as steel. Here, three types of joints are considered, that is, adhesive bonding, metal bonding, and shrink fitting.

In the second stage, design of ceramic sleeve connected to steel shaft by shrink fitting is studied with shrink fitting ratio of 0.2×10^{-3}. Attention should be paid at contact part because thermal stress appearing on the contact part is large due to thermal expansion mismatch between ceramic and steel. In order to reduce thermal stress and bending stress at this part, therefore, design of joint portion of the roller is considered by varying geometry of the shaft. Then, an application of ceramic roller to steel manufacturing machinery is also consider in this stage.

In the third stage, simulation of coming out of the shaft from the ceramic sleeve is carried out. The coming out phenomenon is indicated by z-displacement of the steel shaft as well as shear stress distribution along contacting shaft surface.

1.6   Thesis outlines

This thesis consists of five chapters. Chapter 1 provides the problem statement and motivation of the study. Also, it provides a review of the recent research on ceramic rolls. The objectives and thesis layout are also available at the end of this chapter.

In Chapter 2, suitable joint selection for ceramic roller is discussed in detail. The roller consists of ceramic sleeve and steel shaft subjected to both distributed load and thermal load. The appropriate joint method is considered in terms of joint strength. In this chapter, three types of joints are considered, namely, adhesive bonding, metal bonding, and shrink fitting. Then, each model is investigated under room temperature and high temperature. All models are performed by finite element model analysis. Finally, stress appearing on the joint part of each model is evaluated and compared.

In Chapter 3, a new ceramic roller structure used in the heating furnace is discusses. Although all ceramics sleeve has high temperature resistance and high corrosion resistance, attention should be paid for the risk of fracture due to the thermal expansion of the steel shaft that is much larger than the one of ceramic. To consider thermal stress approximately, a simple double cylinder roller consisting of outer ceramic and inner steel is considered. Then, the effect of the inner cylinder thickness on the thermal stress σ_θ appearing at the outer cylinder will be investigated. The finite element analysis shows that tapered shaft thickness is desirable for the ceramic hearth roller. Finally, an application of ceramic roller to steel manufacturing machinery is considered by changing geometry and material.

In chapter 4, failure analysis for coming out of the steel shaft from ceramic sleeve connected by shrink fitting is investigated. Since the ceramic sleeve is brittle, only low shrink fitting ratio can be applied. The coming out behavior of the roller during rotation is analyzed by the finite element method. The effect of the shrink fitting ratio on the coming out of the shaft is discussed as well as several other parameters, such as Young's modulus of the shaft, the friction coefficient, magnitude of the load, and geometry of the shaft.

Finally, Chapter 5 provides the major conclusions, the most significant outcomes and contributions and suggestions for future works.

References

[1]. Barsoum, M.W., Fundamentals of ceramics, *Tailor&francis,* Boca Raton, FL, 2003

[2]. Carter, C.B. and Norton, M.G., Ceramics materials, *Springer*, new York, 2007

[3]. Chiang, Y.M., Birnie, D.P., and Kingery, W.D., Physicla ceramics, *John wiley&sons*, New York, 1997

[4]. Richerson, D.W., Modern ceramic engineering: properties, processing, and use in design. *CRC pres*, Salt Lake City, UT, 1992

[5]. Davidge, R. W., Mechanical behavior of ceramics, Cambridge university press. John Wiley&Son, UK, 1979

[6]. Larsen, R. P. and Vyas, A.D., The outlook for ceramics in heat engines: 1900-2010, SAE Paper No. 880514, *Society of Automotive Engineers*, Dearborn, MI, 1998

[7]. Wray, P., Advanced structural ceramics: Tech Monitoring, *SRI International*, Japan, 1991

[8]. Hori, Y., Miyakawa, Y., Asami, S., and Kajihara, T., $Si_3 N_4$ Ceramic Valves for Internal Combustion Engines, SAE Technical Paper 890175, 1986

[9]. Ogawa, Y., Machida, M., Miyamura, N., Tashiro, K. et al., Ceramic Rocker Arm Insert for Internal Combustion Engines, SAE Technical Paper 860397, 1986

[10]. Ogawa, Y., Ogasawara, T., Machida, M., Tsukawaki, Y. et al., Complete Ceramic Swirl Chamber for Passenger Car Diesel Engine, SAE Technical Paper 870650, 1987

[11].   Jahanmir, S., Friction and wear of ceramics, *Marcell Dekker*, New York, 1994

[12].   Woydt, M., and Habig, K. H., High Temperature Tribology of Ceramics, Tribol. Int. 22, pp. 75-88, 1989

[13].   Matsubara, H., Miyashita, K., Iguchi, Y., Tanaka, S. et al., Superior Charging Technology by Screw Supercharger and High Technology Turbocharger for Automotive Use, SAE Technical Paper 890455, 1989

[14].   Kawase H, Kato, K et al., Development of ceramics turbocharger rotors for high temperature use, ASME paper no 91-GT-270, 1991

[15].   Kanazawa, N., Niwa, K., and Sugimoto, T., The automotive ceramic gas turbine development results in Japan, Industrial Ceramics, 19, pp. 179-183, 1999

[16].   Mikami, T., Tanaka, S., Tagashira, K., and Koga, S., Application of ceramics to THE CGT301, A 300 kw class ceramic gas turbine, Industrial Ceramics, 19, pp. 184-188, 1999

[17].   Whitney, D. E., Ceramics cutting tools: Materials, Development, and Performance, Noyes Publication, New Jersey, USA, 1994

[18].   U. Dworak, High-tech ceramics: Viewpoints and perspectives, ed. by K. Gernot, Academic Press Limited, London, 1, 1989.

[19].   Bonollo, F., Urban, JR., Bonatto, B., and Botter, M., Gravity and low pressure die casting of aluminium alloys: a technical and economical benchmark, *Alluminio E Leghe,*, **6**, pp.23-32, 2005.

[20].   Noda, N.A., Hendra, Takase, Y., Li, W., Thermal stress analysis for ceramics stalk in the low pressure die casting machine. Journal of Solid Mechanics and Material Engineering,, **3**, pp.1090-1100, 2009.

[21].   Noda, N.A., Hendra, Li, W., and Takase, Y., Thermal stress and heat transfer coefficient for ceramics stalk having protuberance dipping into molten metal. Journal of Solid Mechanics and Material Engineering, 4(8), pp.1198-1213, 2010.

[22].   Ryan, M.J., et al: Prestresse sialon aluminum-casting riser tubes. *JACS*, **49**(2013), 44.

[23].   Ogawa, E., et al., Proceedings of 8th International Conference on Zinc and Zinc Alloy Coated Steel Sheet, Hdg Process Technologies, (2011), 1.

[24].   Miki, E., High corrosion resistance and cost reduction by spraying methods, *Plant Engineer*, **21**(1), pp. 8, 1989.

[25].   Noda, N.A., Sano, Y., Takase, Y., Li, W., and Sakai, H., Application of large ceramics structures to steel manufacturing machinery, *International Journal of Engineering Innovation and Management*, **1**, pp.77-82, 2011.

[26].   Ogawa, E., et al., Practical evaluation of large ceramics rolls for continuous hot dipping steel sheet production line, Hitachi Metals Technical Review, **28**(2012), 50-54

[27].   Noda, N.A., Yamada, M., Sano, Y., Sugiyama, S., and Kobayashi, S., Thermal stress for all-ceramics rolls used in molten metal to produce stable high quality galvanized steel sheet, *Engineering Failure Analysis*, **15**, pp.261-274, 2008.

[28].   Noda, N. A., Hendra, Takase, Y., and Tsuyunaru, M., Maximum stress for shrink fitting system used for ceramics conveying rollers, *Journal of Solid Mechanics and Materials Engineering*, 2(8), pp.1410-1419, 2008.

[29].   Li, W., Noda, N. A., Sakai, H., and Takase, Y., Analysis of Separation Conditions for Shrink Fitting System Used for Ceramics Conveying Rollers,

Journal of Solid Mechanics and Materials Engineering; 5(1), pp.14-24, 2011.

[30].   Li, W., Noda, N. A., Sakai, H., and Takase, Y., Thermal Stress Analysis for Shrink fitting System used for Ceramics Conveying Rollers in the Process of Separation, *Key Engineering Materials*, 452-453, pp.241-244, 2011.

[31].   Truman C. E., Booker J. D., Analysis of a Shrink-fit Failure on a Gear Hub/Shaft Assembly, *Engineering Failure Analysis*, 14, pp. 557-572, 2007.

[32].   Antoni N, Contact Separation and Failure Analysis of a Rotating Thermo-elastoplastic Shrink-fit Assembly, *Applied Mathematical Modelling*, 37, pp.2352-2363, 2003.

[33].   Hagen, K., Silicon nitride for high temperature applications, Journal of the American Ceramics Society, 93(6), pp.1501-1522, 2010.

Chapter 2

Ceramic/Steel Joint Selection for the Ceramic Roller Used under Room Temperature and High Temperature

2.1   Introduction

Ceramic can be used as a roller material at high temperature because of its high temperature resistance, corrosion resistance, and wear resistance. However, the brittleness of the ceramic restricts the machine design of structures, and therefore the ceramic has to be joined frequently to metals.

In this study, a steel conveying roller is considered to be used in the heating furnace whose atmosphere temperature is 1,200^{o}C as shown in Figure 2.1. The roller consists of ceramic sleeve and steel shafts, which is subjected to both distributed load and thermal load. Joint selection is very important for ceramic roller to realize its full potential. The major problem in ceramic/metal joints is different thermal expansion coefficient at high temperature. The thermal stress often causes not only low strength in bonded joint but also a fracture in the ceramic.

Many researchers have conducted research on ceramic rolls and rollers used under high temperature. Ceramic materials have been applied to cylindrical large components successfully, for example, stalk in the low-pressure die casting machine [1,2], conveying roller in the hot rolling mills [3], rolls in the galvanizing line [4-6], in the furnace [7], rolling rolls, and die cast sleeve [8]. However, only few studies are available for joint selection of the ceramic roller.

In this study, therefore, in order to obtain the most suitable joint for ceramic roller, three types of joints will be studied, namely, adhesive bonding, metal bonding, and shrink fitting. Here, the strength analysis of the roller joints under room temperature and at high temperature will be investigated. Then, the maximum stress appearing at joint portion for each model will be evaluated and compared.
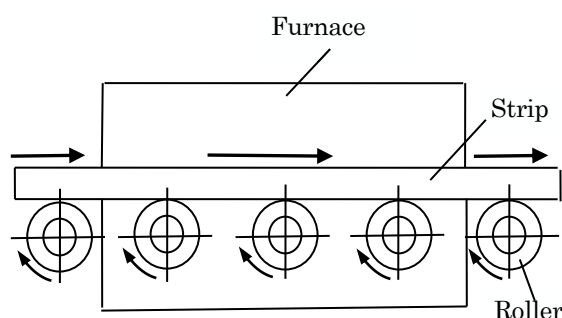
Figure 2.1 Layout of hearth roll for heating furnace

2.2   Models and boundary condition

Ceramic/metal joints are studied in this study for the roller used in the heating furnace under high temperature. Figure 2.2 shows the dimensions of the roller. It is seen that the total length of the roller is 3,800mm and the outer diameter is 300mm. In this study ceramic/metal joints are considered for the roller used in the heating furnace whose temperature is 1200°C. Figure 2.3 shows thermal boundary conditions on the roller. As shown in Figure 2.3(a), the heating is applied on the outside surface of the sleeve with temperature 1,200^{o}C, while air cooling is applied on the inside surface of roller. The room temperature is assumed as 20°C. Here, the roller is subjected to distributed load of w=30N/mm as shown in Figure 2.3(b). The roller is simply supported at both ends.

Table 1.1 represents the material properties of the roller where the sleeve is ceramic silicon nitride (Si$_3$N$_4$) and the shaft is SCM415. Tensile strength of ceramic 500MPa in Table 2.1 is estimated as the half value of the bending strength 1000MPa [9,10]. Considering thermal expansion mismatch between ceramic and steel, the appropriate joint method is considered in terms of joint strength.
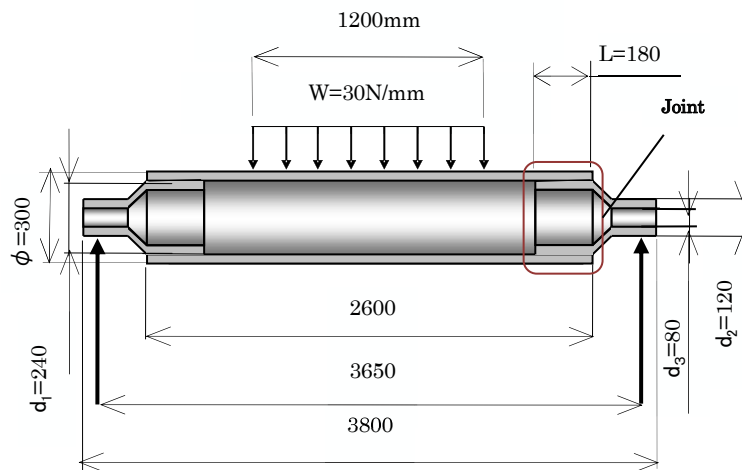
Figure 2.2 Dimensions of the roller (mm)
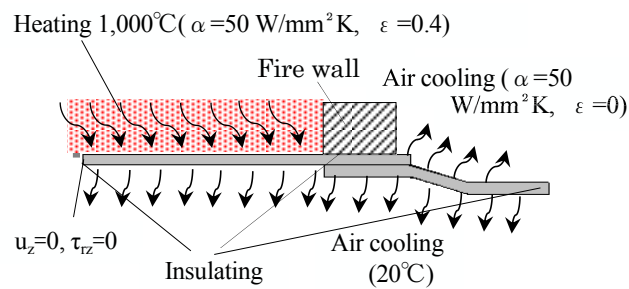
(a) Thermal boundary condition
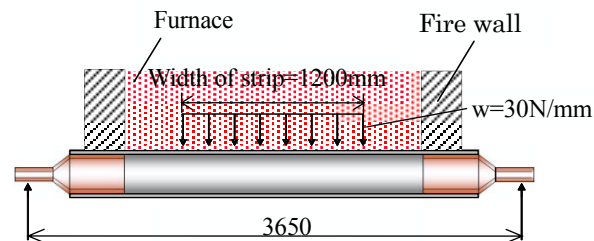
(b) Load condition

Figure 2.3 Boundary condition

2.3 Comparison between three types of joint for ceramic roller

To understand the most suitable mechanical design, ceramic/steel roller joint is considered under room temperature and high temperature. Here, three types of joints are investigated, namely, the adhesive bonding as Model 1, metal bonding as Model 2, and

shrink fitting as Model 3 in Figure 2.4.

For Model 1 and Model 2, interlayer materials are necessary to be considered to bond ceramic sleeve and steel shaft. Here, the interlayer material used for Model 1 is epoxy with 0.5mm of thickness as shown in Figure 2.4(a). Figure 2.5 shows the bonding strength of adhesive. It is seen that the bonding strength of epoxy decreases exponentially

Table 2.1 Properties of materials

Properties		Ceramic	Steel
Young's modulus [GPa]		300	210
Poisson's ratio		0.28	0.3
Mass density [kg/m^3]		3200	7800
Thermal conductivity [W/m·K]		62.5	25
Thermal expansion coefficient [1/K]		0.3×10^{-5}	1.2×10^{-5}
Specific heat [J/kg·K]		650	477
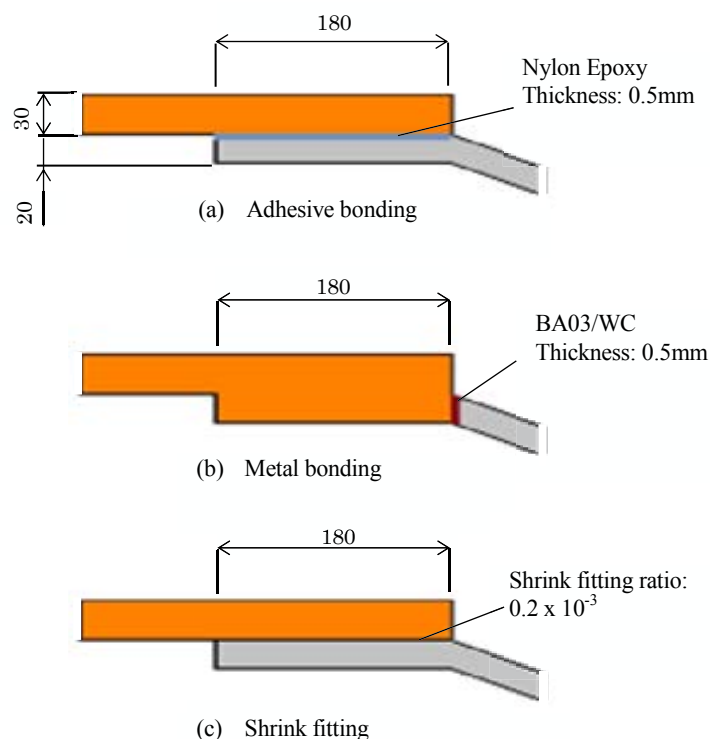
Figure 2.4 Three types of joints

with increasing temperature [11]. The bonding strength 55MPa at room temperature
(25°C) becomes almost 0MPa over temperature 150°C.

For Model 2, the ceramic sleeve is connected to steel shaft by metal bonding
(see Figure 2.4(b)). Contact length of the bonding is 180mm with inserted material
thickness of 0.5mm. The inserted material used for this method is aluminum alloy
(BA03/WC) because BA03/WC has high bonding strength as shown in Table 2.2 [12].
Figure 2.6 shows that the bonding strength of BA03/WC decreases over temperature [8].

For Model 3 (see Figure 2.4(c)), ceramic sleeve and steel shafts are connected
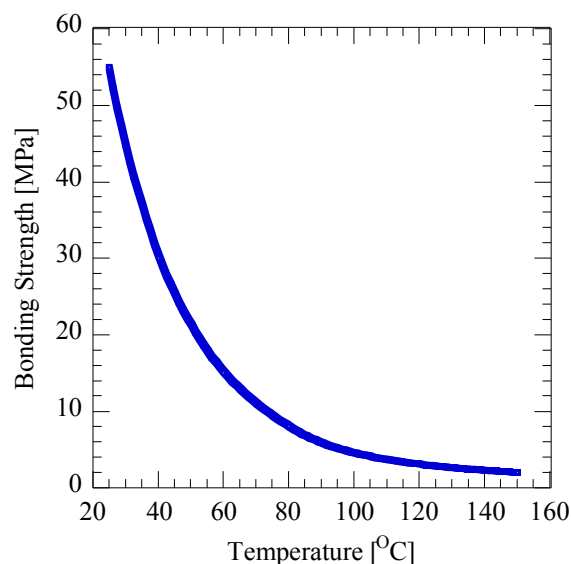
Figure 2.5 Bonding strength of the Nylon
epoxy vs. temperature

Table 2.2 Bonding strengths of the ceramic to metal bonding with varying
interlayer material [12]

Ceramic/Metal	Interlayer	Strength[*] (MPa)
Si$_3$N$_4$/Steel	BA03/WC	200
SiC/Steel	BA03/WC	150
Sialon/Steel	BA03/WC	300
Sialon/Steel	SUS 304/WC	150
Si$_3$N$_4$/SUS 405	Fe/W	60
SiC/Super alloy	Ni/Kovar/Cu	100
SiC/SUS 316	Ti/Mo	50

*) Tensile test
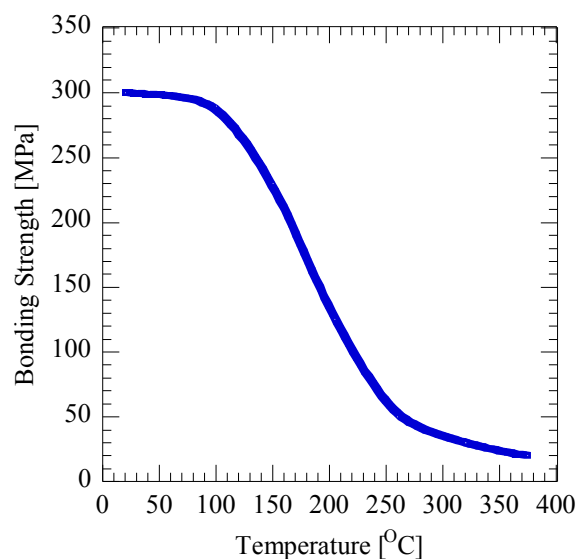
Figure 2.6 Bonding Strength of BA03/WC
vs. temperature

by shrink fitting. The fitting ratio is defined as δ/d. Here, δ is diameter difference and d is inner diameter of the sleeve. The shrink fitting ratio used in this study is assumed as 0.2×10^{-3}. Numerical analysis for all models is performed by finite element model (FEM). The smallest mesh size used at the joint parts is 0.05mm.

2.4 Results and discussion

2.4.1 Stress analysis for the adhesive bonding on the ceramic sleeve/steel shaft joint

Figure 2.7(a) shows stress distribution σ_r along the interface for Model 1 due to distributed load w under room temperature 20°C. It is seen that the stress is very small along adhesive surface at room temperature. Here, the maximum stress appearing on the bonding tip interface is about 9MPa, which is much lower than bonding strength of the epoxy 55MPa [11]. It can be concluded that the adhesive bonding is strong enough to resist the distributed load w under room temperature 20°C.

Next, stress along the interface is analyzed under high temperature. To understand effects of the temperature, in the first place, the temperature distribution should be investigated in Figure 2.8. It can be seen in that the temperature gradually

(a) σ_r under room temperature   (b) σ_r under high temperature
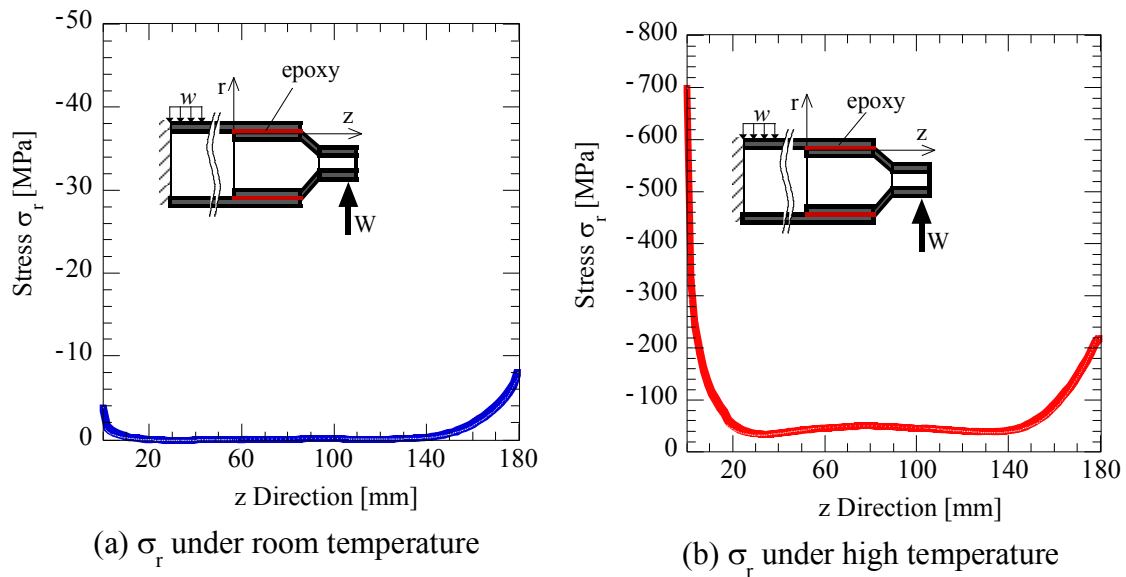
Figure 2.7 Stress σ_r at adhesive layer for Model 1
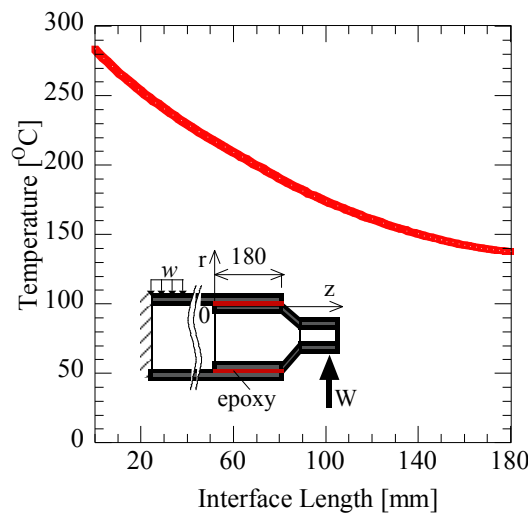
Figure 2.8 Temperature distributions at adhesive bonding surface

decreases from $z=0$ to $z=180$mm. The maximum temperature at $z=0$ is about 280°C, while at $z=180$mm the minimum temperature is 136°C.

Figure 2.7(b) shows stress distribution σ_r along the interface for Model 1 due to distributed load w under high temperature $1,200^{o}$C. The maximum stress about 700MPa appears at the end of the bonding. Also, it is found that stresses at the end of interface tend to infinity, which indicates that a singular stress field exists around the end of the

interface. Moreover, since the temperature distribution is in range 136°C~280°C, the bonding strength of the epoxy becomes approximately 0MPa (see Fig. 2.5). Therefore, the failure on the bonding part occurs. In other words, adhesive bonding cannot be used in the heating furnace under temperature 1,200°C.

2.4.2 Stress analysis for the metal boding on the ceramic sleeve/steel shaft joint

Figure 2.9(a) shows stress distributions along the interface under room temperature 20°C. In Figure 2.9(a), maximum stress σ_z=100MPa appears at the inserted material BA03/WC at room temperature, which is lower than bonding strength of the BA03/WC. It means that this condition is quite safe.

Figure 2.9 (b) shows stress distributions along inserted material surface of the metal bonding under high temperature conditions 1,200°C. The inserted material has two contacted sides, namely, ceramic contacting side and steel contacting side. Since the difference between both sides is less than 2%, the steel contacting side is considered. It is clear from the graph that stress around both edges of the metal joint goes to infinity. It means that the singular stress field exists around the edge of the joint structure. Since the temperature on the bonding surface is about 131°C, the bonding strength of the inserted

(b) σ_z under room temperature   (b) σ_z under high temperature
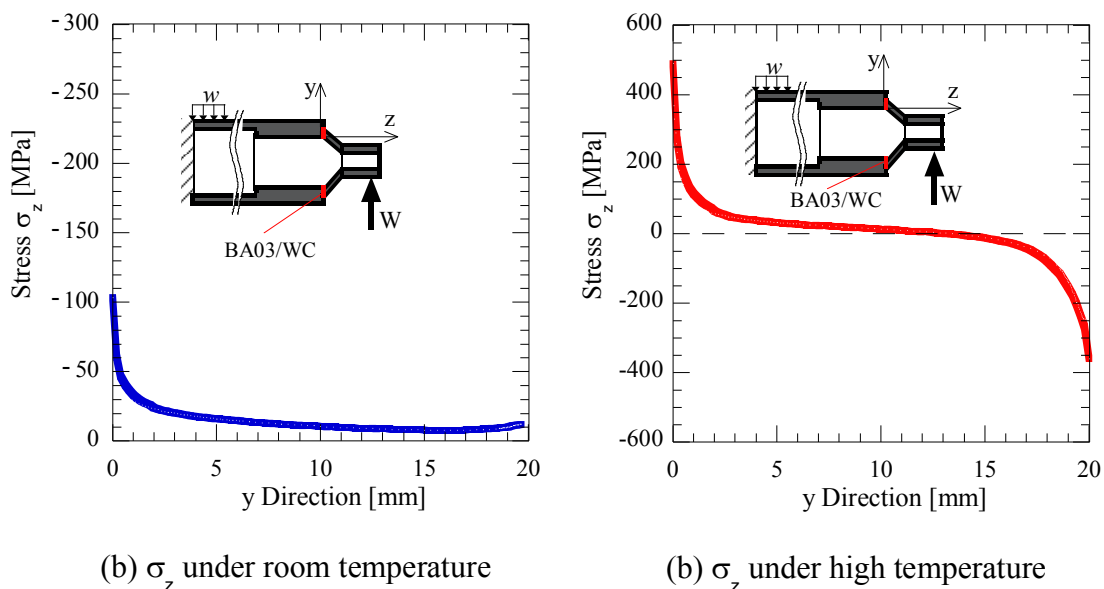
Figure 2.9 Stress σ_z at metal bonding layer for Model 2

material, BA03/WC becomes 252MPa [12]. Here, the maximum stress produced at the edge surface of the joint is 500MPa. This stress value is larger than bonding strength of the metal bonding BA03/WC at temperature 131°C. This condition shows that the metal bonding method is not suitable for the ceramic/steel roller used at high temperature. This is different material properties lead to failure at the bonding part in roller.

2.4.3   Stress analysis for the shrink fitting on the ceramic sleeve/steel shaft joint

Figure 2.10 shows stresses distribution at the joint for Model 3. Figure 2.10(a) shows stress distribution σ_θ for ceramic sleeve at room temperature. As can be seen in Figure 2.10(a), maximum stress σ_θ=34MPa appears at the end of ceramic sleeve. Maximum stress σ_θ is lower than allowable stress of the ceramic material σ_{al}= 333MPa [9, 10]. It indicates that the joint structure is quite safe.

Figure 2.10(b) shows the stress distribution for ceramic sleeve part at high temperature 1,200^{o}C. As shown in Figure 2.10(b), maximum stress σ_θ at ceramic sleeve portion is 192MPa, which is lower than allowable stress of ceramic material σ_{al}= 333MPa [9, 10]. It indicates that fracture does not happen for Model 3.

It is found that shrink fitting is the most suitable joint method for roller used in both room and high temperature operation.

2.5   Conclusions

In this study, appropriate joint selection was considered for ceramic roller used under room temperature and high temperature. The roller consists of ceramic sleeve and steel shaft subjected to both distributed load and thermal load. Since thermal expansion mismatch between ceramic and steel is a main problem, the appropriate joint method is considered in terms of joint strength. Here, three types of joints were investigated, namely, adhesive bonding as Model 1, metal bonding as Model 2, and shrink fitting as Model 3. The conclusions can be obtained as following.

(1) Since the maximum stresses are lower than allowable stress at joint portion for Model 1, 2, and 3, all joint methods can be applied to the ceramic roller used under room temperature.

(2) However, under high temperature, only the shrink fitting can be the appropriate

joint for hearth roller. This is because bonding strength becomes very small under high temperature for adhesive bonding and metal bonding.
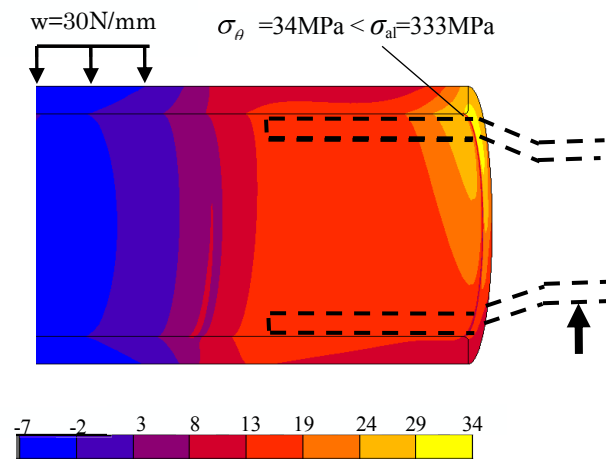
w=30N/mm σ_θ =34MPa < σ_{al}=333MPa

-7   -2   3   8   13   19   24   29   34

(a) σ_θ under room temperature

σ_θ =192MPa < σ_{al}=333MPa

w=30N/mm σ_θ =169MPa

-34   -16   10   32   55   78   100   124   192
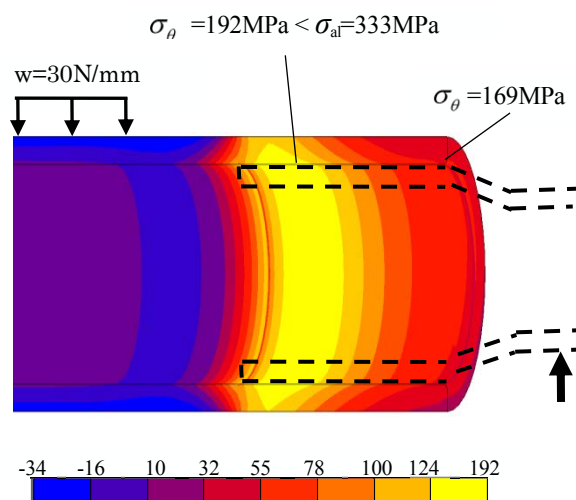
(b) σ_θ under high temperature 1200°C

Figure 2.10 σ_θ due to both heating load and distribution load

References

[1].   F. Bonollo, J. Urban, B. Bonatto, and M. Botter, "Gravity and low pressure die casting of aluminium alloys: a tachnical and economical benchmark," *Allumino E Lenge*, vol. 6, pp. 23-31, 2005.

[2].   N.A. Noda, Hendra, Y. Takase, W. Li, "Thermal stress analysis for ceramics stalk in the low pressure die casting machine," *Journal of Solid Mechanics and Material Engineering*, vol. 10, pp. 1090-1100, 2009.

[3].   N. A. Noda, Hendra, Y. Takase, and M. Tsuyunaru, "Maximum stress for shrink fitting system used for ceramics conveying rollers," *Journal of Solid Mechanics and Materials Engineering*, vol. 11, pp. 1410-1419, 2008.

[4].   N.A. Noda, M. Yamada, Y. Sano, S. Sugiyama and S. Kobayashi, "Thermal stress for all ceramics rolls used in the molten metal to produce stable high quality galvanized steel sheet," *Engineering Failure Analysis*, vol. 4, pp. 261-274, 2008.

[5].   Ogawa E, et al. Development of 100% ceramic pot rolls for continuous hot dip coating lines of the steel sheet, *Proceedings of 8th International Conference on Zinc and Zinc Alloy Coated Steel Sheet* 2011, vol. 6, pp. 1-8, 2011

[6].   Ogawa E, Shimizu K, and Hamayoshi S. "Practical evaluation of large ceramic rolls for continuous hot dipping steel sheet production line", *Hitachi Metals Technical Review,* vol. 28,   pp. 50-55, 2012. (in Japanese)

[7].   Matsuda S, Suryadi D, Noda NA, Sano Y, Takase Y, and Harada S. "Structural Design for Ceramics Rollers Used in the Heating Furnace", *Transactions of the JSME Series A,* vol. 79(803), pp. 989-999, 2013. (in Japanese)

[8].   N.A. Noda, Hendra, W. Li, and Y. Takase, "Thermal stress and heat transfer coefficient for ceramics stalk having protuberance dipping into molten metal," *Journal of Solid Mechanics and Material Engineering*, vol. 8, pp. 1198-1213, 2010.

[9].   136th Committee Processing Technology of Japan Society of Promotion and Science, "Fine Ceramics Research Handbook", 414-419, *Uchida Roukakuho*, Japan, 1998.

[10].   Ceramics editorial committee, "Mechanical properties of ceramics, 3rd edition", 65, *Ceramics Association*, Japan, 1982.

[11].   Nicholas, J. D., "Adhesive: Theory and Technology", *Industrial press inc.*, New York, 1970.

[12].   Suganuma, Katsuaki, "Recent advances in joining technology of ceramics to metals", *ISIJ International*, vol. 30(12), pp. 1046-1058, 1990.

Chapter 3

Proposal for Hearth Roller Consisting of Ceramic Sleeve and Steel Shafts Used in the Heat Treat Furnace

3.1   Introduction

Advanced structural ceramic has been used since 1970s as electrical insulator, automotive engines [1, 2], tribology components [3], cylinder head plates, pistons and turbocharger rotors, machine tools, rolling mills and low-pressure die casting machine. Several marketing researches for the advanced ceramic has been done in USA, Japan, and Germany. Under both thermal and mechanical loadings, however, structural ceramic is not very popular until now compared to functional ceramic widely used [4]. As an example, intense efforts have been done to develop ceramic gas turbine during 1950s-1990s, but only ceramic coatings are in use now. This is because all ceramic components may be too brittle to design turbine component. Generally speaking, advanced ceramic projects have not progressed very well as shown in this example.

On the other hand, for treatment of molten metal, ceramic die cast sleeves and ceramic stalks in the low-pressure die casting machine are commonly used now [5-8]. As an extension of those cylindrical components, large ceramic rolls are recently developed for galvanizing steel line, and other applications are being considered [9]. Since conventional cast iron and stainless steel rolls used in molten metal need high cost of maintenance [10], ceramic use may contribute reducing d costs significantly [11].

In this study therefore we will focus on hearth rollers used in the heating furnace whose atmosphere temperature is more than $1,000^{\circ}\text{C}$ as shown in Figure 3.1(a). Conventional rollers have ceramic coated steel sleeve and shafts connected each other by shrink fitting as shown in Figure 3.1(b). Although the inside of the roller is cooled by water circulation to reduce the temperature, the roller coating deteriorates in short period due to the thermal expansion difference between ceramic and steel. Then, finally, the conventional rollers are changed very frequently because of the wear induced by the hot conveyed strips.

In previous studies thermal stress was discussed for rolls consisting of ceramic sleeve and ceramic shaft used in molten metal [12]. Maximum stress for shrink fitting

system used for ceramic conveying rollers with steel shaft was considered under room temperature with varying shrink fitting ratio [13]. Regarding the conventional structure in Figure 3.1(b) used under high temperature, water cooling system was discussed as well as how to reduce joint stress by inserting buffer layer [14]. However few references are available for ceramic/steel joints under high temperature without inserting buffer and without water circulation.

In this study therefore a new roller is considered focusing on the joint structure as shown in Figure 3.1(c). Then the effects of roller geometry and the material difference will be considered in order to reduce the thermal stress and mechanical stress. Finally, most desirable geometry and materials will be proposed by considering the use at steel manufacturing machinery.

3.2   Small thickness structure can reduce thermal stress

In ref. [13], the ceramic roller structure was studied without considering thermal stress when a ceramic sleeve and steel solid shaft are connected by shrink fitting at both ends. Although detail dimensions are different from the ones in Figure 3.1(c), the results are useful in this study. Here, $\sigma_{\theta s}$ is the shrink fitting stress and $\sigma_{\theta max} = \sigma_{\theta s} + \sigma_{\theta b}$ is the maximum stress when the distributed load $w = 100N/mm$ is applied after shrink fitting. Therefore, $\sigma_{\theta b}$ is the stress due to distributed load.

(a) Layout of hearth roll

(b) Conventional rollers structure

(c) Proposed rollers structure
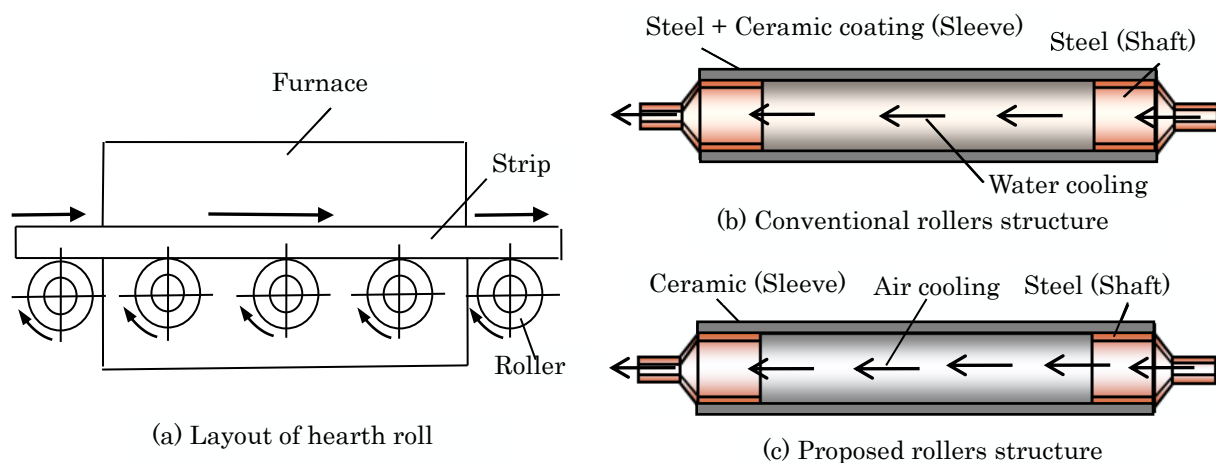
Figure 3.1 Conventional and proposed rollers for heating furnace

Figure 3.2 illustrates effects of shrink fitting ratio δ/d upon stress $\sigma_{\theta s}$, $\sigma_{\theta max}$, $\sigma_{\theta b}$ [13]. Figure 3.2(a) shows $\sigma_{\theta s}$, $\sigma_{\theta max}(= \sigma_{\theta s} + \sigma_{\theta b})$ vs. δ/d relationship when load distribution w = 100N/mm is applied after shrink fitting. To clarify the effect of distributed load, Figure 3.2(b) shows $\sigma_{\theta b} = \sigma_{\theta max} - \sigma_{\theta s}$ vs. δ/d relationship when load distribution w = 100N/mm is applied. From Figure 3.2(b) it is found that $\sigma_{\theta max}$ has a minimum value at $\delta/d = 0.050 \times 10^{-3}$. When $\delta/d \geq 0.150 \times 10^{-3}$, $\sigma_{\theta s}$ increases linearly with increasing δ/d. On the other hand, $\sigma_{\theta b}$ decreases with increasing δ/d, and becomes constant when $\delta/d \geq 0.150 \times 10^{-3}$. Detail investigations reveal that constant value $\sigma_{\theta b} = 10.5 MPa$ coincides with the value when the shaft and sleeve are perfectly bonded as a unit body. From Figure 3.2(b), it is found that the large δ/d reduces the contact stress $\sigma_{\theta b}$ by gripping the shaft tightly. It may be concluded that $\sigma_{\theta max} = \sigma_{\theta s} + \sigma_{\theta b}$ has a minimum value at a certain value of δ/d. This is because with increasing δ/d stress $\sigma_{\theta s}$ increases monotonously but $\sigma_{\theta b}$ decreases and becomes constant.

Figure 3.3(a) shows $\sigma_{\theta s}$, $\sigma_{\theta max}(= \sigma_{\theta s} + \sigma_{\theta b})$ vs. δ/d relationship when load distribution w = 100N/mm is applied after shrink fitting for different fitted length L [13]. Here, we assume the fitted length L=100mm, 150mm, and 210mm. Small value of L are desirable for the maintenance because exchanging the sleeve is easier for smaller L. Figure 3.3(b) the $\sigma_{\theta b}$ vs. δ/d relationship when load distribution w = 100N/mm is applied. When shrink fitting ratio $\delta/d \geq 0.2 \times 10^{-3}$, $\sigma_{\theta b}$ becomes constant and independent of δ/d. When shrink fitting ratio $\delta/d \geq 0.2 \times 10^{-3}$, the shaft and sleeve can be treated as unit body bonded perfectly.

(a) $\sigma_{\theta max}$ vs. δ/d and $\sigma_{\theta s}$ vs. δ/d (b) $\sigma_{\theta b}$ vs. δ/d

Figure 3.2 σ_θ vs. δ/d when L=210mm

($\sigma_{\theta max} = \sigma_{\theta s} + \sigma_{\theta b}$, $\sigma_{\theta s}$=stress due to shrink fitting, $\sigma_{\theta s}$=stress due to distributed load)

(a) $\sigma_{\theta max}$ vs. δ/d (b) $\sigma_{\theta b}$ vs. δ/d
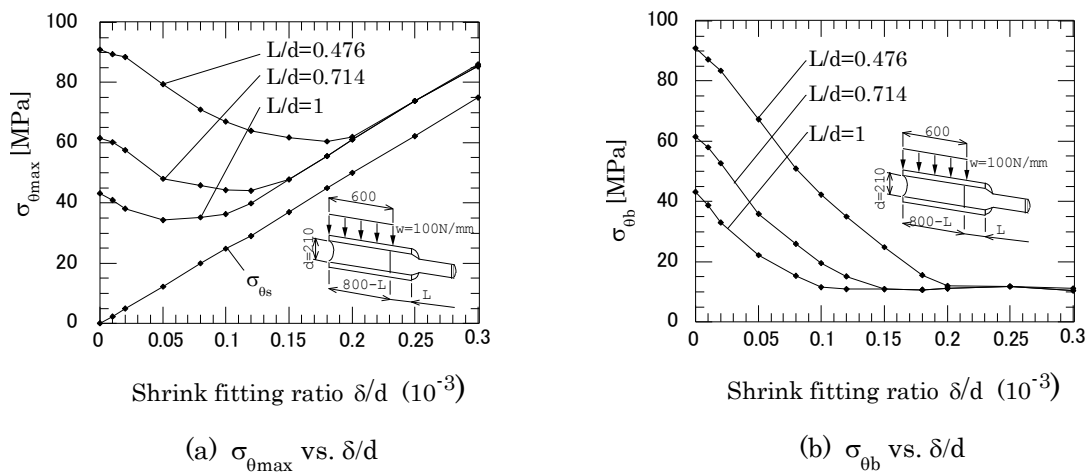
Figure 3.3 σ_θ vs. δ/d when L=100mm, L=150mm, L=210mm

($\sigma_{\theta max} = \sigma_{\theta s} + \sigma_{\theta b}$, $\sigma_{\theta s}$=stress due to shrink fitting, $\sigma_{\theta s}$=stress due to distributed load)

From Figure 3.3(a), it is found that $\sigma_{\theta max}$ has a minimum value 60.5MPa at $\delta/d = 0.18 \times 10^{-3}$ when L=100mm. Similarly, it is found that the optimum shrink fitting ratio is $\delta/d = 0.12 \times 10^{-3}$ when L=150mm, and also $\delta/d = 0.05 \times 10^{-3}$

when L=210mm. When shrink fitting ratio $\delta/d \geq 0.2 \times 10^{-3}$, $\sigma_{\theta b}$ becomes constant 10.5MPa independent of δ/d.

In the previous study [13], shrink fitting stress and mechanical stress were considered. Next, thermal stress should be considered. In Figure 3.1(c) all ceramic sleeve has high thermal resistance and wear resistance. The steel shaft is usually made of chromium molybdenum steel JIS SCM415, stainless steel JIS SUS304, or high chrome steel JIS STBA26. Since the thermal expansion coefficient of such steel is about four times larger than the one of ceramic, care should be taken for the risk of fracture due to the hoop stress appearing at the ceramic sleeve. Figure 3.4 shows 0.2% proof stress $\sigma_{0.2}$ depending on temperature for SCM415, SUS304, and STBA26.

To consider thermal stress approximately, a simple double cylinder roller consisting of outer ceramic and inner steel is considered as shown in Figure 3.5. Then, the effect of the inner cylinder thickness on the thermal stress σ_θ appearing at the outer cylinder will be investigated. The shrink fitting ratio between ceramic outer cylinder and steel inner cylinder is defined as δ/d, where δ is the diameter difference and d is the dimension of the inner diameter of the outer cylinder. Here, $\delta/d = 0.2 \times 10^{-3}$ is used for investigation, which is only about one fifth of the steel structures. In our previous study, if the shrink fitting ratio δ/d is larger than $\delta/d = 0.15 \times 10^{-3}$, the shaft and sleeve can be
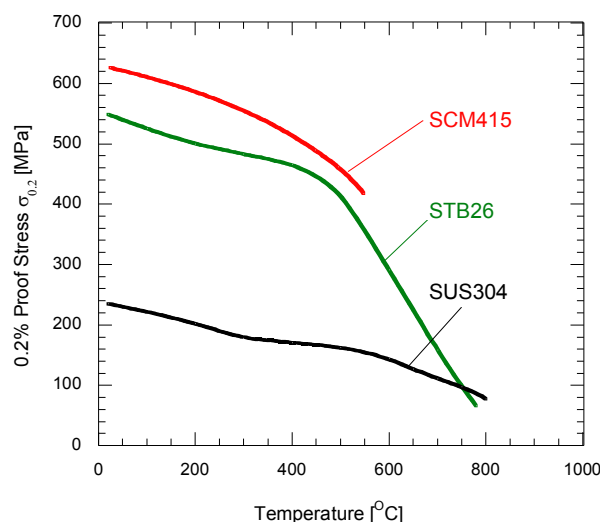
Figure 3.4 The 0.2% proof stress σ0.2 vs. temperature
for SCM415, SUS304, and STB26

treated as a unit body when thermal and mechanical stresses are considered [13]. Heating time is assumed as 0-5,000 s. The heating is applied on the outside surface of the outer cylinder, while the air cooling is applied on the inside surface of the inner cylinder in double cylinder roller. The connected part in Figure 3.5(a) is located at the wall of the furnace whose temperature is assumed about 500°C in Figure 3.5(b), which is about an average temperature between furnace temperature inside and room temperature outside in Figure 3.5(a). Since the thermal expansion coefficient of the steel is about four times larger than the one of the ceramic, the inner cylinder tends to expand more. The contact heat transfer coefficient is assumed as 1.0 X 10^9 W/m^2·K.

Figure 3.6 shows the σ_θ appearing at the inside surface of the outer cylinder. Here, the maximum thermal stress σ_θ is indicated with varying the thickness h of inner cylinder. It should be noted that the smaller thickness h has smaller thermal stress σ_θ because of the smaller rigidity of inner cylinder. For example, when h=30 mm is changed to h=10 mm, the maximum stress becomes less than allowable stress of ceramic σ_{al}=333MPa [15, 16] with safety factor of 1.5.

Figure 3.7 shows σ_θ at the inside surface of the outer cylinder vs. the thickness of the inner cylinder h normalized by $\sigma_{\theta solid}$. It is seen that $\sigma_\theta/\sigma_{\theta solid}$ increases with
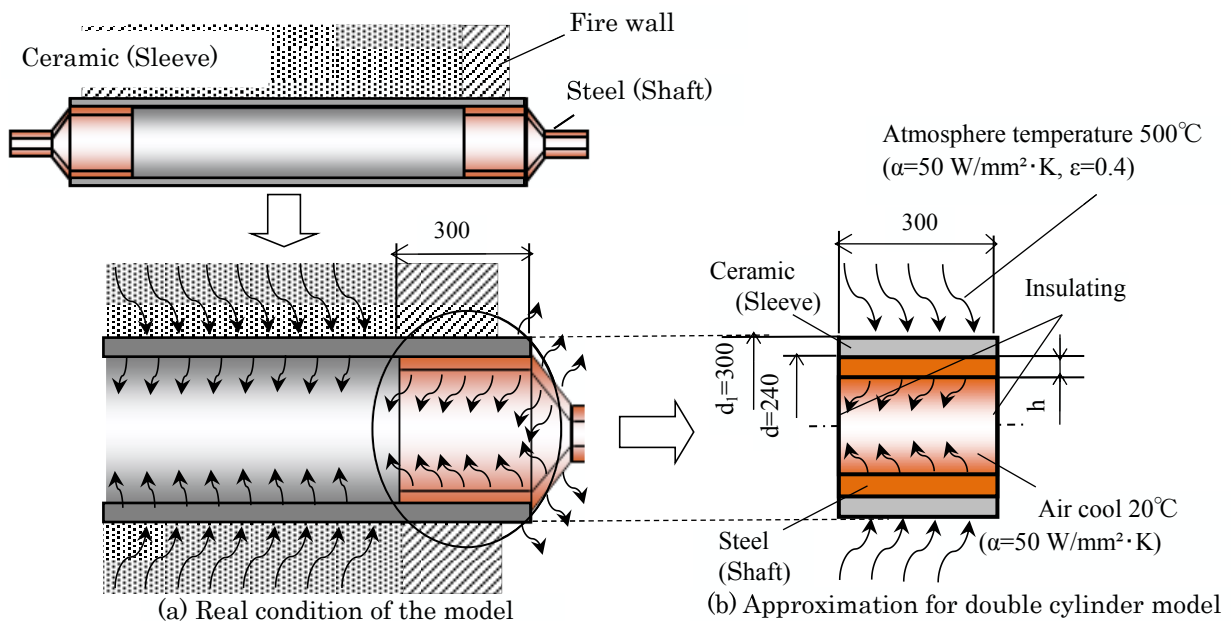
Figure 3.5 Thermal boundary condition on double cylinder

increasing the heating time. From Figure 3.7, $\sigma_\theta/\sigma_{\theta solid}$ becomes constant if h≥30mm when heat heating time t=1,000s. However, $\sigma_\theta/\sigma_{\theta solid}$ increases with increasing h when at heating time t=10,000s. Figure 3.7 indicates that the larger thickness of the inner cylinder leads to the large thermal stress when the heating time is large enough.

It should be noted that usually thicker structures are safer than thinner ones, but
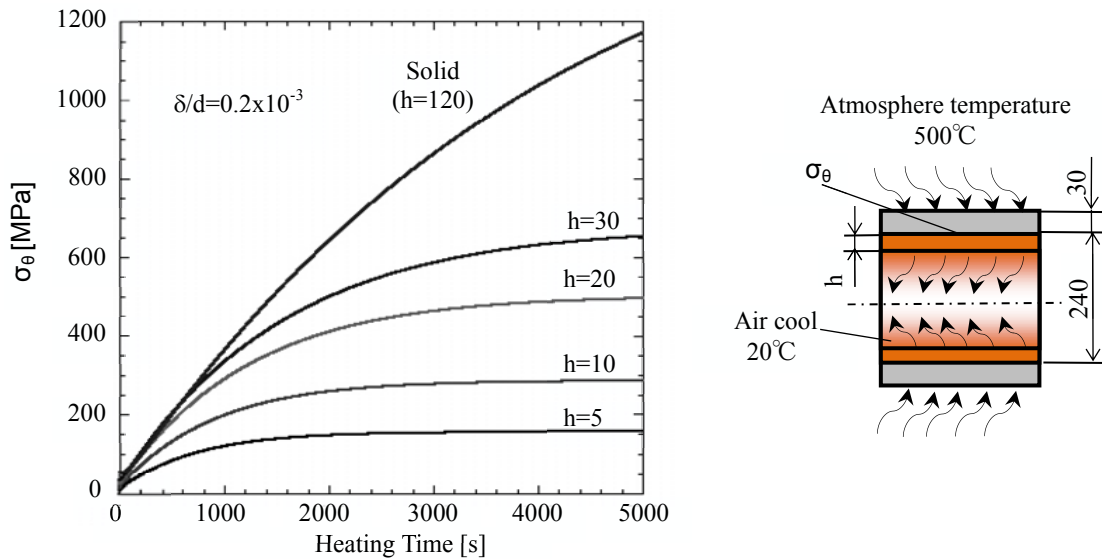
Figure 3.6 σ_θ at the inside surface of the outer cylinder vs. time with varying the thickness of the inner cylinder h
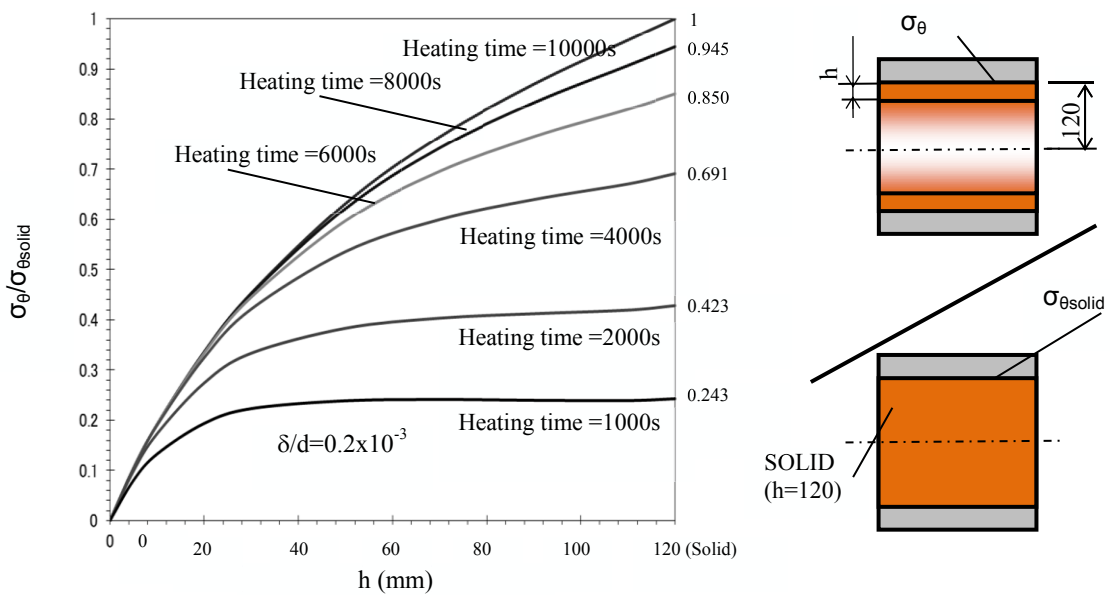
Figure 3.7 σ_θ at the inside surface of the outer cylinder vs. the thickness of the inner cylinder h normalized by $\sigma_{\theta solid}$

Figure 3.6 and 3.7 show that thinner ceramic/steel structures are safer than thicker ones.

3.3 Maximum thermal stress under 1,000°C is close to ceramic allowable stress

3.3.1. Boundary conditions

In this study, ceramic roller used in the furnace will be investigated under the temperature 1,000°C and 1,200°C. The previous chapter indicates that the smaller inner thickness produces smaller σ_θ at the outer cylinder. However, the extremely small thickness may be unsuitable for the bending load. For example, in Figure 3.6, h=30mm provides σ_θ=670MPa which is too large compared to allowable stress σ_{al}=333MPa, and h=10mm looks quite small. Therefore, we assume h=20mm to be used for the real roller in the first place. Fig.8 shows dimensions of the roller with h=20mm. Considering the previous study, Fig. 8 has shrink fitting ratio $\delta/d = 0.2 \times 10^{-3}$ and fitted length ratio L/d=1.22.

(a) The proposed roller length (Half model)

(b) Detail of contact position
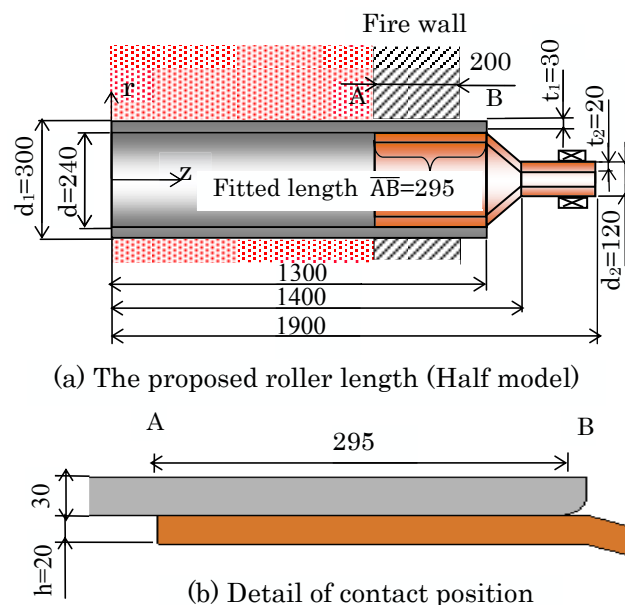
Figure 3.8 Dimensions of the proposed roller
with shrink fitting ratio δ/d=0.2 x 10⁻³

Figure 3.9 shows thermal and mechanical boundary conditions on the roller. As shown in Figure 3.9(a), the heating is applied on the outside surface of the sleeve with temperature 1,000°C, while air cooling is applied on the inside surface of roller. The atmosphere temperature in the furnace is obtained from the preheating experiments as shown in Figure 3.10. As shown in Figure 3.10, the heating time 10,000s is necessary to reach the saturation temperature. Here the roller consists of a ceramic sleeve and two steel shafts connected by shrink fitting with ratio $\delta/d = 0.2 \times 10^{-3}$, which is only about one fifth of the steel structures [13]. The inside of the roller is cooled by air instead of water used for conventional roller. The air temperature is approximately 20°C, and the roller is subjected to distributed load w=30N/mm as shown in Figure 3.9(b).
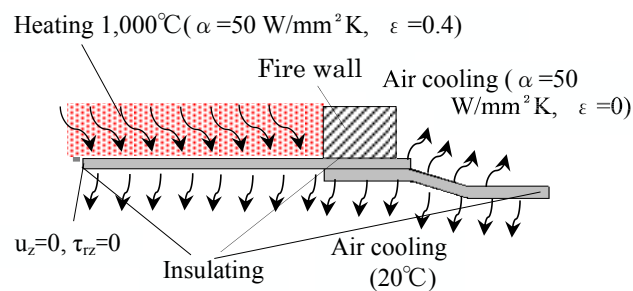
(a) Thermal boundary condition
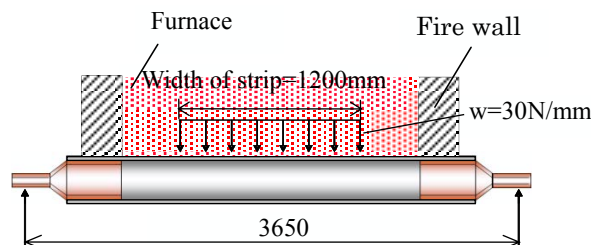
(b) Load condition

Figure 3.9 Boundary condition
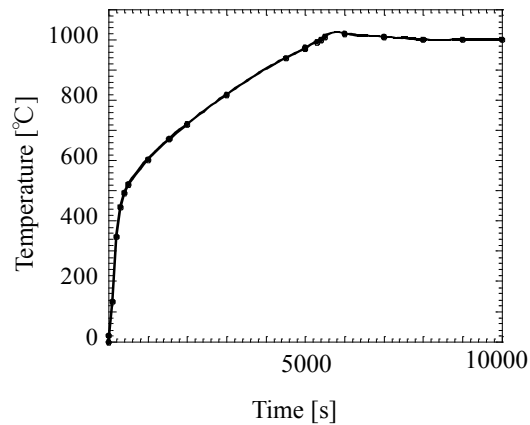
Figure 3.10 Atmosphere temperature in the furnace

Table 3.1 represents the material properties of the roller where the sleeve is silicon nitride and the shaft is SCM415. Tensile strength of ceramic 500MPa in Table 3.1 is estimated as the half value of the bending strength 1,000MPa [15, 16]. Figure 3.11 shows the finite element mesh where the 1/4 model is considered due to symmetry. Static structural analysis is performed to the models by using MSC. Marc Mentat2011 with full Newton-Raphson iterative spare solver of multifrontal method. The total number of elements is 25780 and the total number of the nodes of 31626.

Table 3.1 Properties of material of the proposed rollers at room temperature

Properties of Material	Ceramic	JIS SCM415	JIS SUS304	JIS STB26
Young's modulus [GPa]	300	210	200	210
Poisson's ratio	0.28	0.3	0.3	0.3
Mass density [kg/m^3]	3300	7800	7930	7550
Thermal conductivity [W/m·K]	62.5	25	14.5	45
Thermal expansion coefficient [1/K]	0.3×10^{-5}	1.2×10^{-5}	1.68×10^{-5}	1.15×10^{-5}
Specific heat [J/kg·K]	650	477	480	461
Allowable stress as 0.2%Proof stress [MPa]	333	600	235	549
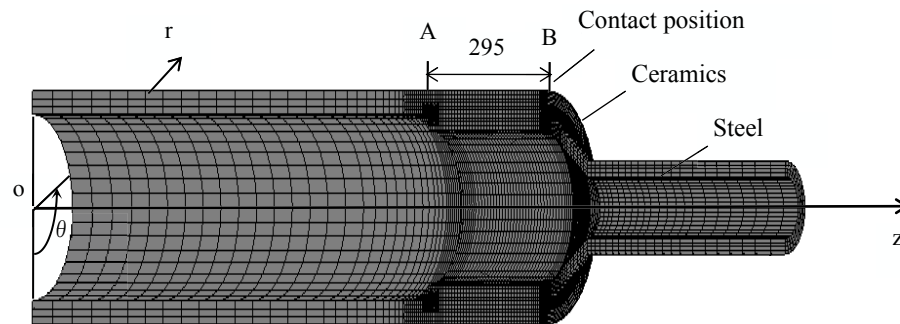
Figure 3.11 FEM model (3D model)

3.3.2. The maximum tensile stress appearing on the ceramic sleeve due to heating

Here, stress appearing on the ceramic sleeve is discussed under the atmosphere temperature 1,000°C. Figure 3.12 shows temperature variation on the outer surface of the ceramic sleeve vs. time. It is seen that a steady temperature appears after heating time 7,000s. Figure 3.12 shows the steady temperatures at points a-e, that is, $T_a = T_b = 900°C$, $T_c = 470°C$, $T_d = 260°C$, and $T_e = 110°C$. In the previous chapter, the atmosphere temperature was assumed as 500℃, which is close to the temperature at point C. Therefore, we have confirmed that the assumed double cylinder model is valid.

Figure 3.13 shows stress distribution σ_θ at 7,000s during heating with maximum stress $\sigma_{\theta max}$. In order to reduce the stress concentration, a radius curvature is put at the end of sleeve as $\rho = 5mm$.   Other stress component such as σ_z is smaller than $\sigma_{\theta max} = 345MPa$. To explain this, Figure 3.13 also indicates maximum stress $\sigma_{zmax} = 176MPa$ appearing at the joint portion and $\sigma_z = 84.2MPa$ appearing at the center of the roller. The maximum thermal stress occurs at point A as $\sigma_\theta = 345MPa$, which is close to allowable stress of ceramic $\sigma_{al} = 333MPa$ [15, 16].
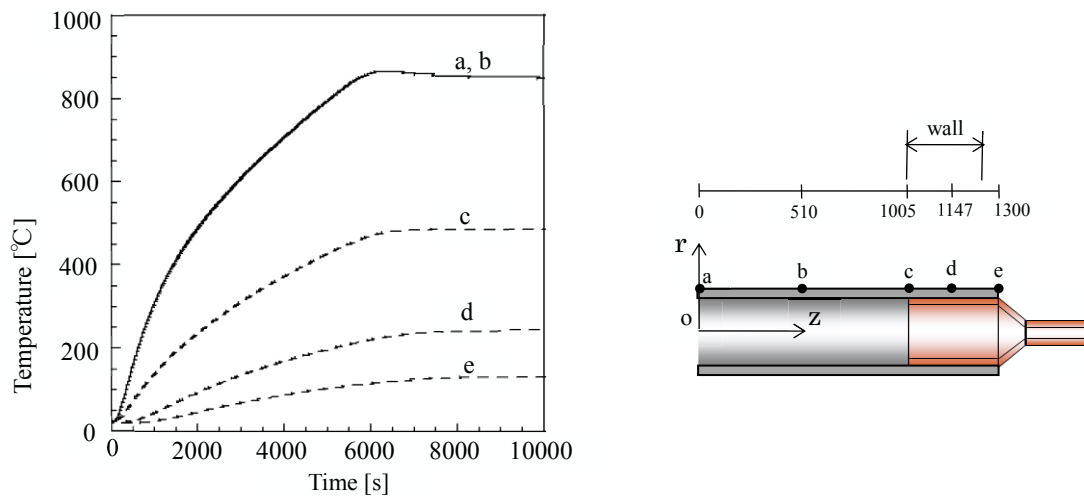
Figure 3.12 Temp. on the outer surface of the sleeve (point a, b, c, d, and e) vs. time

The stress value σ_θ = 420MPa in Figure 3.6 for h=20mm is larger than stress value σ_θ=345MPa at point c in Figure 3.12 although the temperature is nearly 500°C. This is because in the real roller in Figure 3.12, the average temperature along the wall is smaller than 500°C. We have confirmed that the double cylinder approximation is valid and useful.

3.3.3.   The maximum stress appearing on the ceramic sleeve under both heating and distributed loads

As shown in Figure 3.14, distributed load w=30N/mm is considered, which is representing the weight of steel sheets 36,000N. Figure 3.14 shows stress distribution σ_θ under both heating at 7,000s and distributed load w=30N/mm. Maximum tensile stress $\sigma_{\theta max}$=345MPa at the point A before applying distributed load becomes $\sigma_{\theta max}$=346MPa after applying distributed load. In other words, $\sigma_{\theta maxA}$ at A increases 1MPa. On the other hand, stress $\sigma_{\theta B}$=149MPa appearing at the point B before applying distributed load becomes $\sigma_{\theta max}$=160MPa after applying distributed load.. From Figure 3.13 and Figure 3.14, it is seen that $\sigma_{\theta B}$ at point B increases 11MPa.
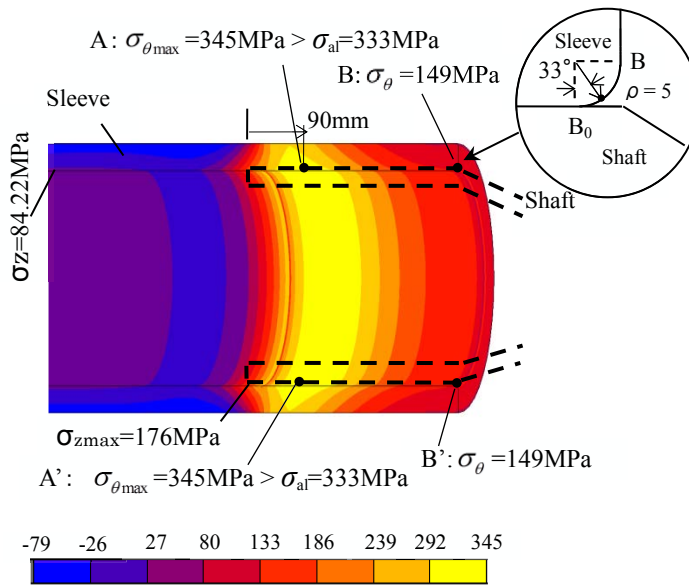
Figure 3.13 σ_θ due to heating load compared to σ_z
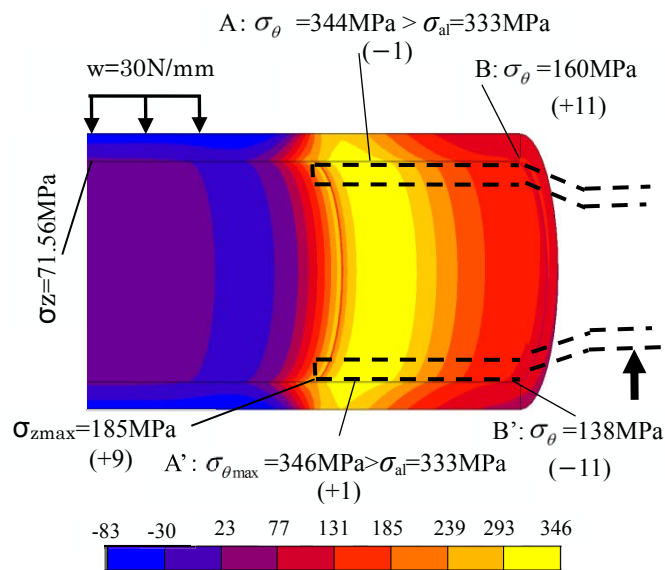
Figure 3.14 σ_θ due to both heating load and distribution

load compared to σ_z (Bending stress effects)

3.3.4.   Study on fatigue strength of the ceramic sleeve

In this study, fatigue strength is considered when the roller is rotating under distributed load. The fatigue problem due to stress fluctuation can be examined by using stress amplitude $\sigma_{\theta a}$ and average stress $\sigma_{\theta ave}$, which is defined by the following equation.

$$\sigma_{\theta ave:A,B} = \frac{\sigma_{\theta maxA,B} + \sigma_{\theta minA,B}}{2} \qquad \sigma_{\theta a:A,B} = \frac{\sigma_{\theta maxA,B} - \sigma_{\theta minA,B}}{2} \qquad (1)$$

The results obtained by Equation (1) at point A and B are plotted in the endurance limit diagram as shown in Figure 3.15. In this case, we focus on σ_{θ}=345±1MPa because other stresses are smaller, for example, σ_z=176±9MPa. Here, point A has the maximum tensile point, while point B has the highest stress amplitude point. Tensile strength of the ceramic is 333MPa [15, 16], while fatigue limit is 200MPa [17, 18] which are placed at vertical axis and horizontal axis, respectively.

The durability line is given by the stress amplitude and the average stress. The safety zone is within the durability line. As shown in Figure 3.15, stress amplitude point A is a little bit beyond the durability line. Stress amplitude at point B is within durability line.

3.4.   Thermal stress under 1,200°C can be reduced by applying tapered shaft

3.4.1.   Analysis of joint structure of the roller

In the previous section, the maximum stress on the ceramic sleeve under heating load 1,000°C was considered for the dimensions in Figure 3.8. Since the roll is
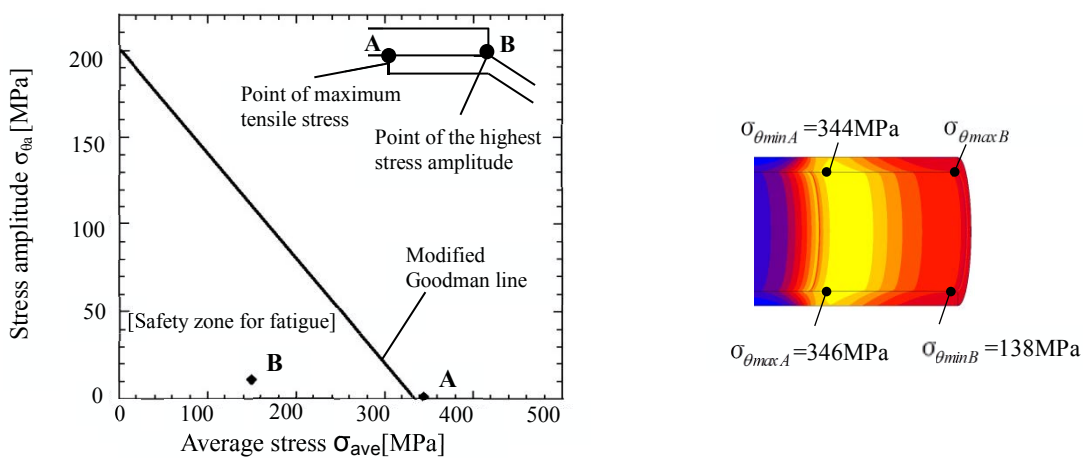
Figure 3.15 Endurance limits and stresses of ceramic sleeve

sometimes used under higher temperature, the heating temperature of 1,200°C will be considered in this section. In this study, three types of shaft models will be analyzed and the strength will be discussed. Table 3.2 and Figure 3.16 show the three models, namely, the uniform thickness of shaft model (Model 1), the tapered shaft model (Model 2), and the short tapered shaft model (Model 3). Table 3.2 represents the detail dimensions of those models.

Table 3.2 Thickness of structural joint of the roller for each model (see Fig. 9)

Model	Sleeve Thickness [mm]	Shaft Thickness [mm]	Fitted Length [mm]	Outer Diameter of the Shaft [mm]	Ratio Fitted Length (L/d)	Shape of The Shaft
Model 1 (standard)	30	20	295	240	1.22	Uniform
Model 2	30	5-30	295	240	1.22	Taper
Model 3	30	15-30	180	240	0.75	Short and taper

3.4.2.   The maximum tensile stress of the ceramic sleeve

It should be noted that even under heating temperature of 1,000°C, maximum tensile stress $\sigma_{\theta max}$ is larger than the allowable stress, that is, $\sigma_{\theta max}$=346MPa>σ_{al}=333MPa. Figure 3.16 shows stress distributions σ_{θ} for ceramic sleeve under heating load temperature 1,200°C. As can be seen in Figure 3.16, maximum stresses appear $\sigma_{\theta max}$ = 416MPa>σ_{al} for Model 1, $\sigma_{\theta max}$=263MPa<σ_{al} for Model 2, and $\sigma_{\theta max}$=216MPa<σ_{al} for Model 3. By applying tapered model, the maximum stress decreases by 37% for Model 2 and by 50% for Model 3. Maximum stress $\sigma_{\theta max}$ for Model 1 is higher than the tensile strength, while $\sigma_{\theta max}$ for Model 2 and 3 are lower. This is because the rigidity of shaft for Model 1 is the largest among the models.
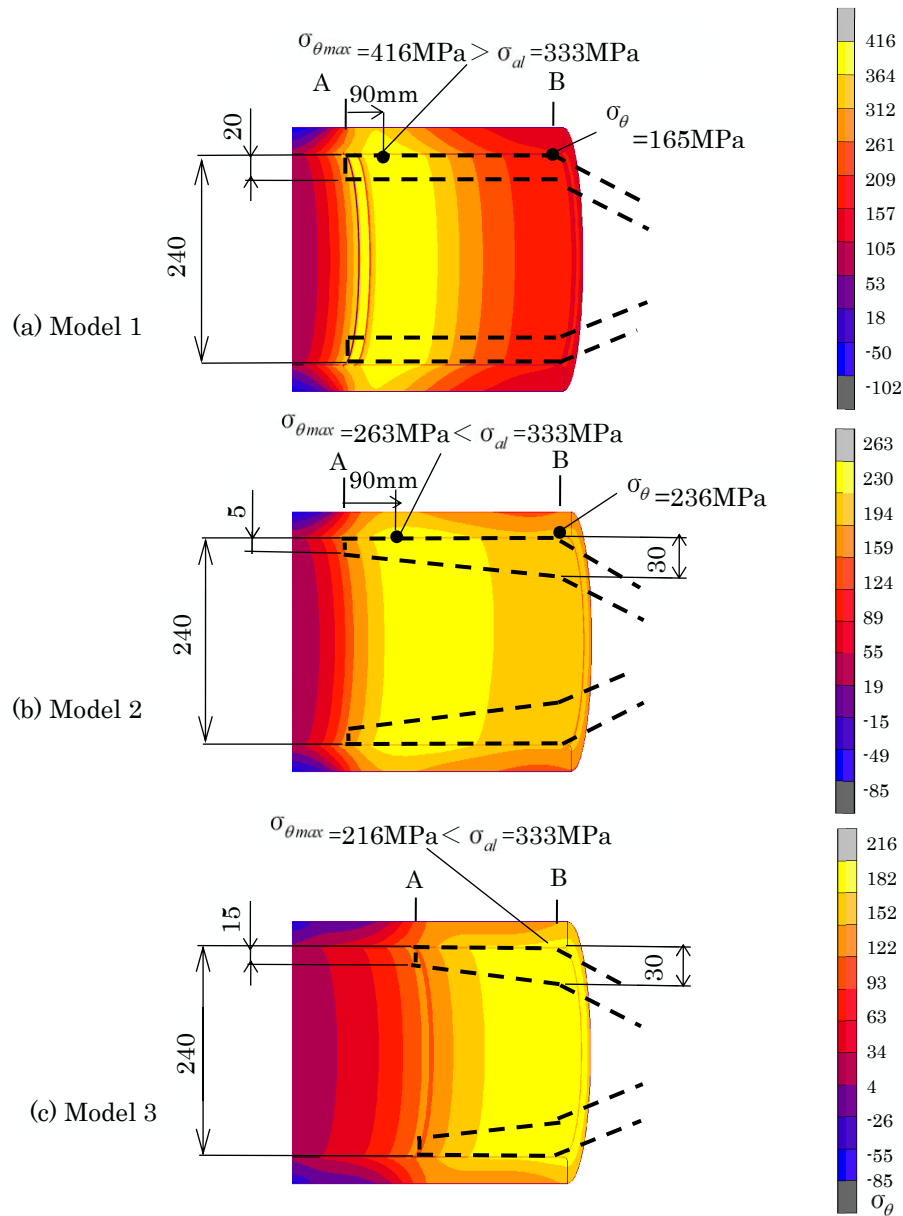
Figure 3.16 Thermal stress σ_{max} for ceramic sleeve with (a)uniform thickness, (b)tapered thickness, (c)short tapered thickness shaft model.

3.4.3.   Strength analysis of the steel shaft based on plastic deformation

Figure 3.17 illustrates stress $\sigma_\theta(z)$ and temperature distributions T(z) along the contact position of the shaft. In Figure 3.17, $\sigma_\theta(z)$ is compared with proof stress $\sigma_{0.2}(z)$ for SCM415 [19], which is depending on T(z). It is seen that temperature T(z) decreases from z=0 to z=300mm. Stress $\sigma_\theta(z)$ along contact surface decreases with decreasing temperature in a similar way. On the other hand, the 0.2% proof stress $\sigma_{0.2}(z)$ of material SCM415 increases with decreasing temperature T(z). Here, the proof stress $\sigma_{0.2}(z)$ is regarded as the allowable stress of the steel shaft. Since plastic deformation is not desirable, stress $\sigma_\theta(z)$ should be lower than the 0.2% proof stress $\sigma_{0.2}(z)$ at the shaft temperature T(z), that is $|\sigma_\theta(z)| < |\sigma_{0.2}(z)|$. In Figure 3.17, the region where $|\sigma_\theta(z)| > |\sigma_{0.2}(z)|$ is a critical region because plastic deformation occurs. While the other region where $|\sigma_\theta(z)| < |\sigma_{0.2}(z)|$ is a safe region because plastic deformation does not occur. It is seen that Model 1 and Model 2 have plastic deformation, and only Model 3 is elastic. Consequently, it is found that the short tapered shaft model (Model 3) is the most desirable.
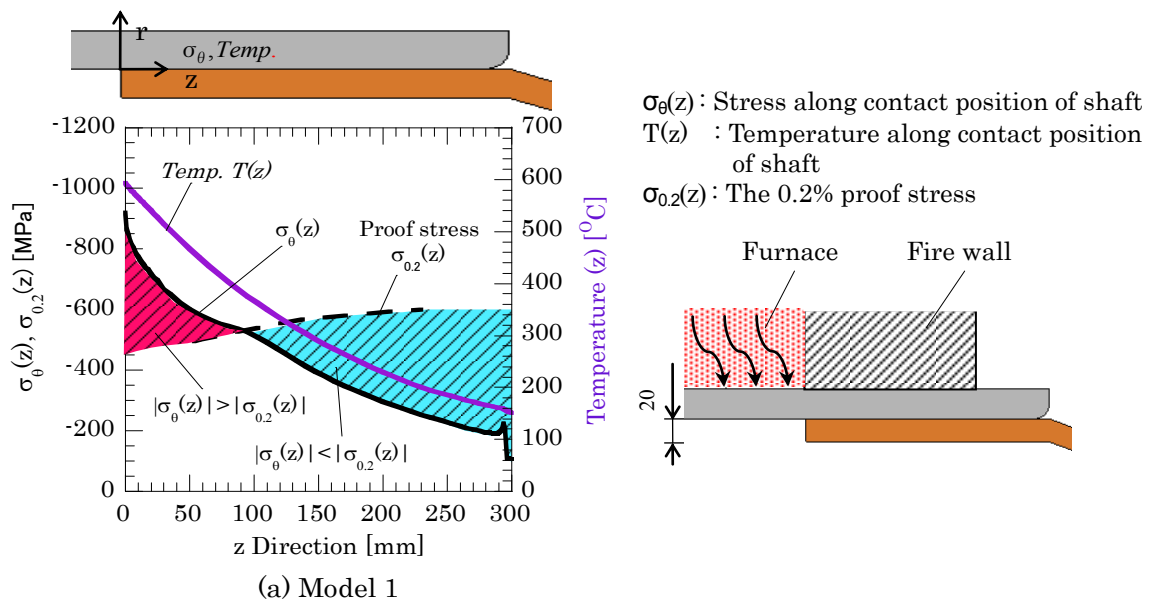
Figure 3.17 Stress and temperature distribution along contact position of shaft toward the 0.2% proof stress (a) uniform thickness shaft model   (cont.)

(b) Model 2
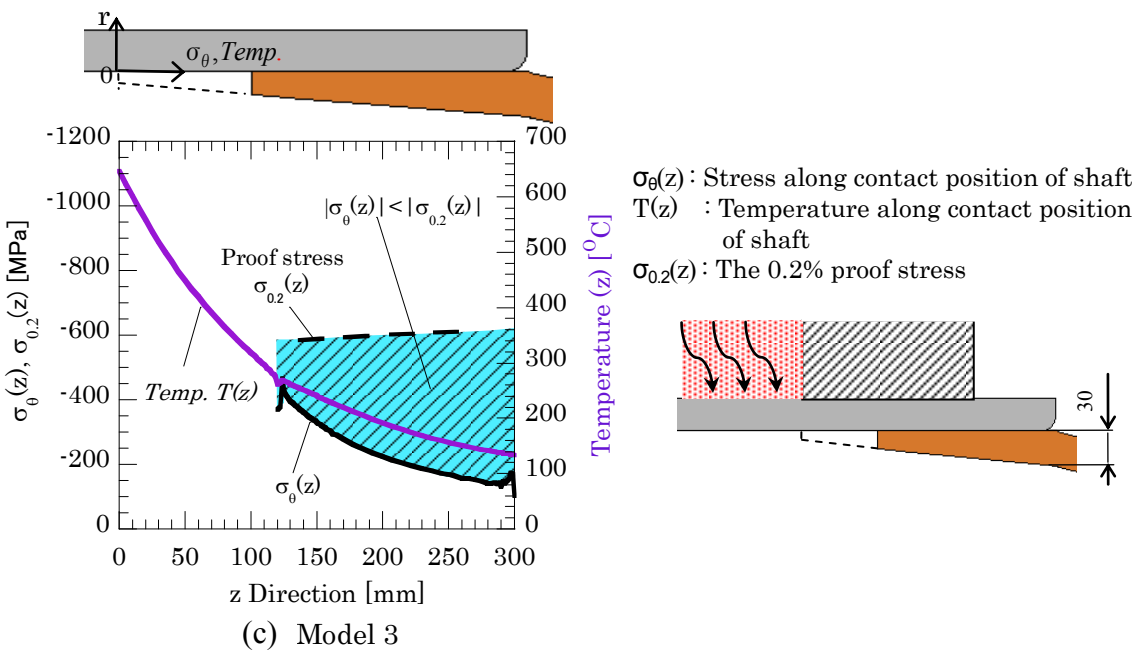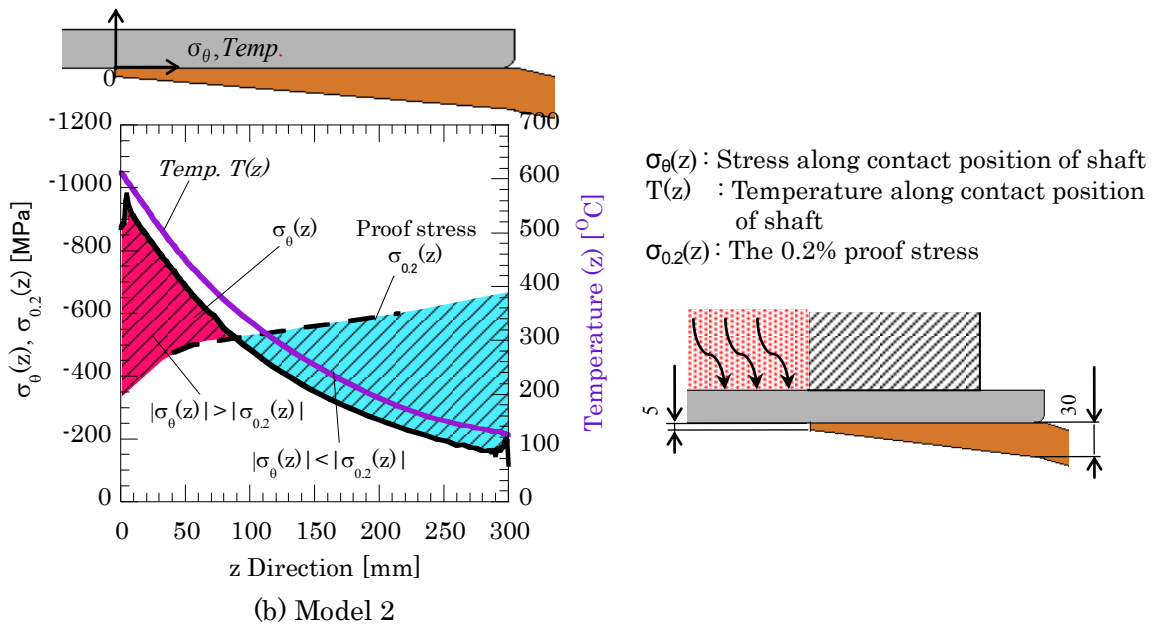
(c) Model 3

Figure 3.17 (continued) Stress and temperature distribution along contact position of shaft toward the 0.2% proof stress (b) tapered thickness shaft model; (c) short tapered thickness shaft model

3.4.4. Fatigue strength for ceramic sleeve

Figure 3.18(a), (b) show the endurance limit diagram. Figure 3.18(a) shows the

results at point A where maximum stress $\sigma_{\theta maxA}$ appears. Figure 3.18(b) shows the results at point B where maximum stress $\sigma_{\theta maxB}$ appears.

First we consider maximum average stress $\sigma_{\theta ave}$ at point A in Figure 3.18(a). The maximum values are $\sigma_{\theta ave}$=210~420MPa. The average stress for Model 1 is $\sigma_{\theta ave}$=420MPa, which is larger than the value of fatigue limit σ_{al}=333MPa. However, the stress amplitudes at point A for Model 1 and 2 is almost zero $\sigma_{\theta a} \cong 0$, and for Model 3 $\sigma_{\theta a}$=5MPa. It is seen that the results for Model 2 and Model 3 are below the durability line of the ceramic material.

Next, we consider maximum stress amplitude $\sigma_{\theta a}$ at point B in Figure 3.18(b). Stress amplitude $\sigma_{\theta a}$ for Model 1 and 2 is about $\sigma_{\theta a}$=10MPa, and for model 3 is about $\sigma_{\theta a}$=5MPa. From Figure 3.18(b), it is found that the results for Model 1, 2, and 3 are below the durability line of ceramic material. According to both Figure 3.18(a) and (b), the fatigue failure does not occur for although Model 1 has large average stress.
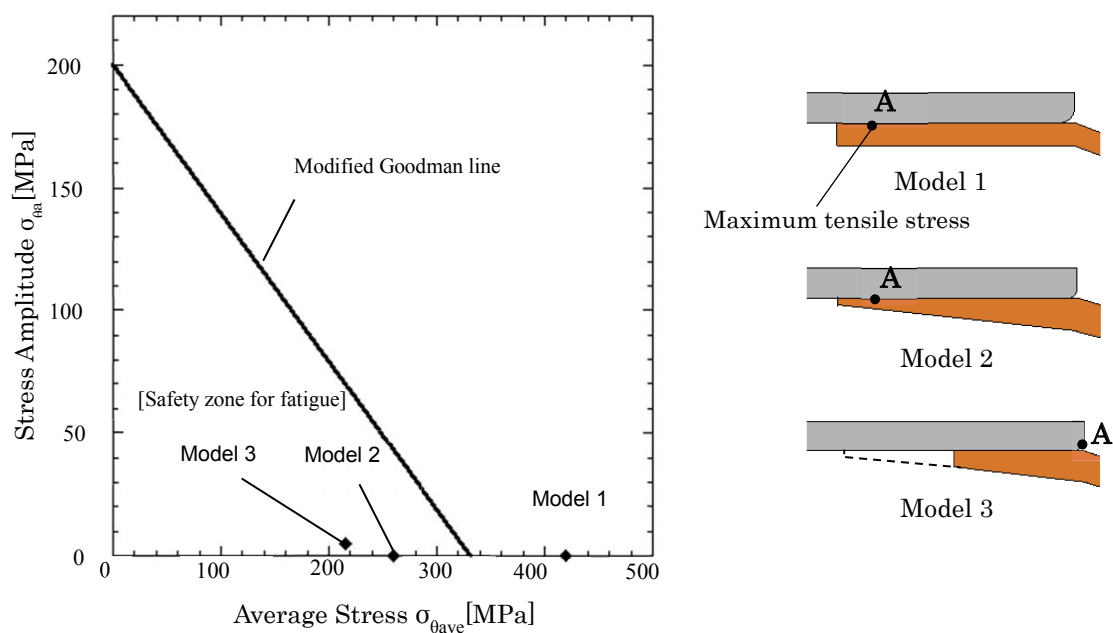
Figure 3.18 Endurance limits and stresses of ceramic sleeve (a) Point A where the maximum stress $\sigma_{\theta maxA}$ appears (continued)
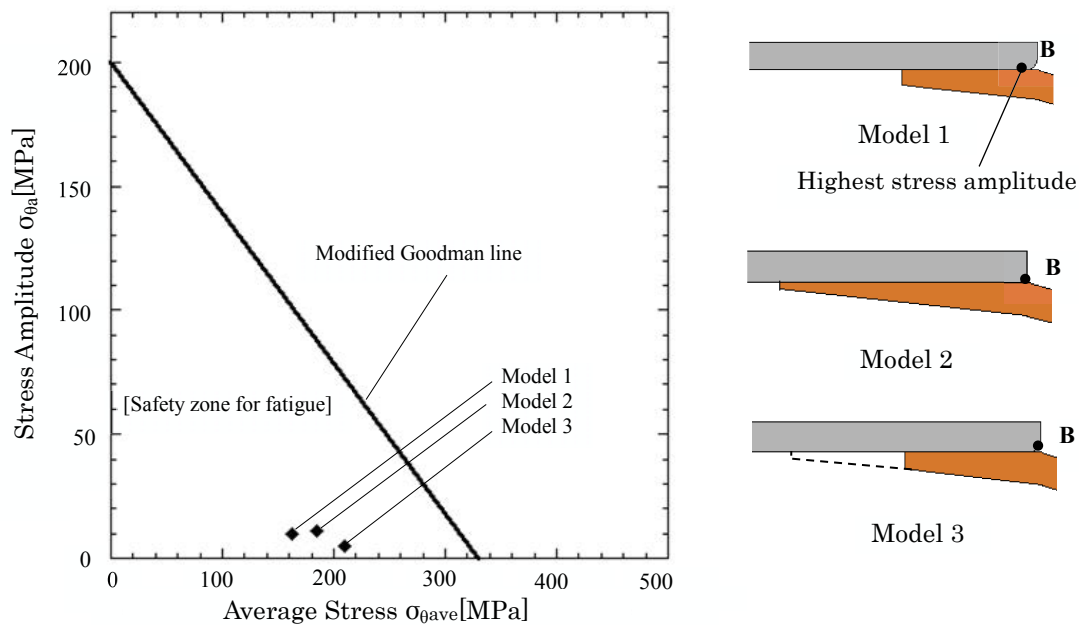
Figure 3.18 (continued) Endurance limits and stresses of ceramic sleeve

(b) Point B where the maximum stress amplitude $\sigma_{\theta maxB}$ appears

3.5 Application of ceramic/steel rollers to a real furnace in a steel manufacturing company

3.5.1 Models considered

In the previous chapters, a ceramic roller consisting ceramic sleeve with steel shaft was considered. In this chapter, an application of ceramic roller to a real furnace in a steel manufacturing company is considered. The company suggests that the roller should consist of three pieces, namely, main-sleeve, intermediate-sleeve, and shaft. The advantage of this three pieces structure is that the damaged components can be changed with low cost. The three components are assumed to be connected by shrink fitting with the ratio 0.2 x 10^{-3} [13].

Fig.19 shows dimensions of the stainless steel roller used in a steel company. The total length of the roller is 1680mm with outer diameter of 210mm, and thickness of the wall is 468mm. The wall is assumed to be insulated. In the first place, by using the dimension in Figure 3.19, the main-sleeve material is changed to ceramic and also the water cooling is changed to air cooling at the same time. This model is named
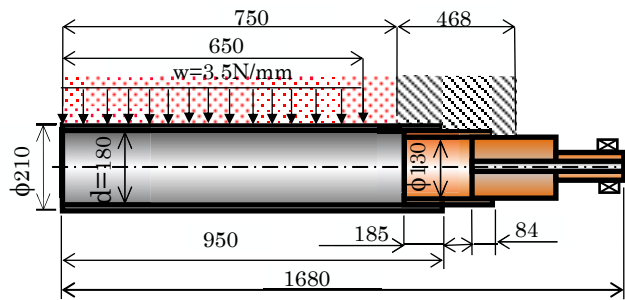
Figure 3.19 Dimensions of the roller considered in the company A
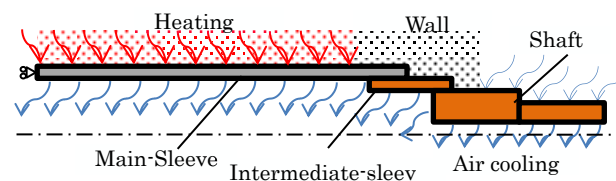
Figure 3.20 Boundary conditions of the real ceramic roller

Model4. Figure 3.20 shows the boundary conditions of the air cooling. The heating is applied on the outside surface of the ceramic sleeve. Here, atmosphere temperature in the furnace varies depending on the time. Also, the air cooling is applied on the inside surface of the roller.

Since the company has used all stainless steel rollers, in the first place, SUS304 is assumed as the intermediate-sleeve and shaft material because of economy. Since strength of SUS304 is low as shown in Figure 3.4, other materials are also considered. Table 3.3 shows comparison between SCM415, SUS304, and STB26. It is noted that the material SCM415 considered in the previous section cannot be used in here because of low oxidation resistance under high temperature.

Table 3.4 shows dimensions and materials four types of models. Model 4 is a basic model first we consider as described above. For Model 5, the joint position is shifted away from the core furnace in order to avoid high temperature effects although the total length of the roller 1680mm is the same as the length of Model 1. For Model 6, a tapered intermediate-sleeve is considered to reduce stress on the main-sleeve. The last model, Model 7, material of the intermediate-sleeve and shaft are changed from the stainless steel JIS SUS304 to the high chrome steel JIS STBA26.

Table 3.3 Comparison of materials

Items	SCM415	SUS304	STB26
Economical?	yes	no	no
High Strength under high temperature?	yes under 550°C	no	yes
High Oxidation resistance under high temperature?	no	yes	yes

Table 3.4 Four types of models for real application
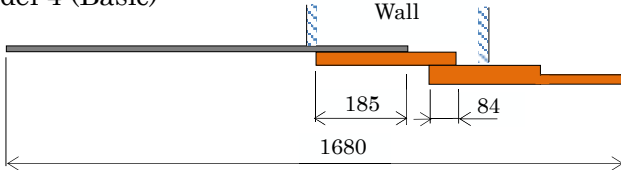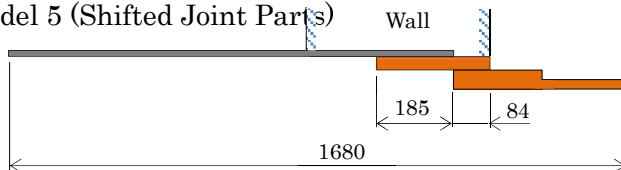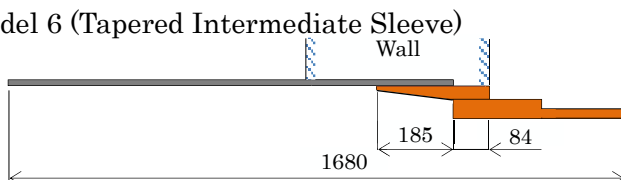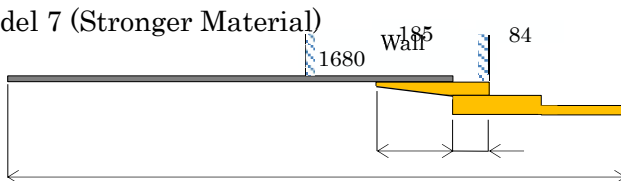
Model	Main Sleeve	Material Intermediate Sleeve	Shaft
Model 4 (Basic)	Ceramic	JIS SUS304 (18Ni-8Cr)	JIS SUS304 (18Ni-8Cr)
Model 5 (Shifted Joint Parts)	Ceramic	JIS SUS304 (18Ni-8Cr)	JIS SUS304 (18Ni-8Cr)
Model 6 (Tapered Intermediate Sleeve)	Ceramic	JIS SUS304 (18Ni-8Cr)	JIS SUS304 (18Ni-8Cr)
Model 7 (Stronger Material)	Ceramic	JIS STBA26 (9Cr-1Mo)	JIS STBA26 (9Cr-1Mo)

Table 3.1 provides properties of each material at room temperature. The allowable stress of ceramic material σ_{al}=333MPa, while 0.2% proof stress $\sigma_{0.2}$ for the stainless steel JIS SUS304 is $\sigma_{0.2}$=235MPa and for the high chrome steel JIS STBA26 is $\sigma_{0.2}$=549MPa.

3.5.2.   High chrome steel tapered model can be used in a real furnace

Table 3.5 shows the maximum stress appearing at three components. It is seen that the maximum stresses at the main-sleeve/intermediate-sleeve joint are always larger than the ones at intermediate-sleeve/shaft joint. This is because main-sleeve and intermediate-sleeve have different thermal expansion coefficients as well as the joint position is close to the core furnace.

From Table 3.5, Model 4 is unsuitable to be used in the furnace because $\sigma_{\theta max}$=954MPa appears at the main-sleeve, and $\sigma_{\theta max}$=-1,007MPa appears at the intermediate-sleeve. Also, it should be noted that the intermediate-sleeve/shaft joint is separated during heating [20]. By shifting joint portion in Model 5, the maximum stress on the main-sleeve/intermediate-sleeve contact part significantly decrease. However, maximum stress at the ceramic sleeve $\sigma_{\theta max}$=376MPa is still larger than allowable stress σ_{al}=333MPa although the intermediate-sleeve/shaft joint is not separated.

In Model 6, to reduce the maximum stress at the ceramic main-sleeve, the tapered intermediate-sleeve model is applied. Table 3.5 shows that maximum stress at the ceramic sleeve $\sigma_{\theta max}$=318MPa is lower than allowable stress σ_{al}=333MPa. However, the maximum compressive stress on the intermediate-sleeve $\sigma_{\theta max}$=450MPa is still larger than the 0.2% proof stress $\sigma_{0.2}$=220MPa. For Model 7, material is changed from the stainless steel JIS SUS304 to the high chrome steel JIS STBA26. Since thermal expansion coefficient of STB26 is lower than JIS SUS304, the maximum compressive stress $\sigma_{\theta max}$=204MPa becomes smaller, and therefore, Model 7 may be the most suitable.

Table 3.5 Maximum stress for all real models application

Model	Main-Sleeve/Intermediate-Sleeve Joints				Intermediate-Sleeve/Shaft-Joints			
	Main-Sleeve $\sigma_{\theta max}$ [MPa]		Intermediate-sleeve $\sigma_{\theta max}$ [MPa]		Intermediate-Sleeve $\sigma_{\theta max}$ [MPa]		Shaft $\sigma_{\theta max}$ [MPa]	
Model 4	954	✗	-1007	✗	Separated	✗	Separated	✗
Model 5	376	✗	-422	✗	-74	✓	-123	✓
Model 6	318	✓	-450	✗	-79	✓	-123	✓
Model 7	204	✓	-289	✓	-59	✓	-101	✓

✗ : dangerous,   ✓ : safe

3.6.   Conclusions

Developing advanced ceramic structure has been promoted in USA, Japan, and Germany since 1970s. Although most of the projects did not succeed substantially, large ceramic rolls and rollers are recently used at steel manufacturing machinery successfully. To promote those large cylindrical ceramic, this study considered the heath roller consisting of ceramic sleeve and steel shaft connected by shrink fitting. Since the thermal expansion of the steel shaft is larger than the one of the ceramic sleeve, the ceramic sleeve is subjected to large hoop stress at the contact portion. As a result of the joint structure analysis, the conclusions can be summarized in the following way.

1. Simple double cylinder model shows that the maximum stress can be reduced by using the small thickness of the steel shaft.

2. Finite element analysis shows that the maximum tensile stress can be reduced by using tapered thickness shaft because of the smaller rigidity at the high temperature portion. It is also found that the plastic deformation of the shaft does not appear by applying the short tapered shaft geometry on the structure.

3. An application of ceramic roller to a real furnace in a steel manufacturing company is considered. It is found that tapered shaft geometry with high chrome steel can be used in a real furnace.

References

[1]   Larsen, R. P. and Vyas, A.D., The outlook for ceramics in heat engines: 1900-2010, SAE Paper No. 880514, *Society of Automotive Engineers*, Dearborn, MI, 1998

[2]   Wray, P., Advanced structural ceramics: Tech Monitoring, *SRI International*, Japan, 1991

[3]   Jahanmir, S., Friction and wear of ceramics, *Marcell Dekker*, New York, 1994

[4]   Dworak, U., High-tech ceramics: Viewpoints and perspectives, ed. by K. Gernot, Academic Press Limited, London, 1, 1989.

[5]   Bonollo, F., Urban, JR., Bonatto, B., and Botter, M., Gravity and low pressure die casting of aluminium alloys: a technical and economical benchmark, *Alluminio E Leghe,*, **6**, pp.23-32, 2005.

[6]   Noda, N.A., Hendra, Takase, Y., Li, W., Thermal stress analysis for ceramics stalk in the low pressure die casting machine. Journal of Solid Mechanics and Material Engineering,, **3**, pp.1090-1100, 2009.

[7]   Noda, N.A., Hendra, Li, W., and Takase, Y., Thermal stress and heat transfer coefficient for ceramics stalk having protuberance dipping into molten metal. Journal of Solid Mechanics and Material Engineering, 4(8), pp.1198-1213, 2010.

[8]   Ryan, M.J., et al: Prestresse sialon aluminum-casting riser tubes. *JACS*, **49**(2013), 44.

[9]   Ogawa, E., et al., Proceedings of 8th International Conference on Zinc and Zinc Alloy Coated Steel Sheet, Hdg Process Technologies, (2011), 1.

[10]   Miki, E., High corrosion resistance and cost reduction by spraying methods, *Plant Engineer*, **21**(1), pp. 8, 1989.

[11]   Noda, N.A., Sano, Y., Takase, Y., Li, W., and Sakai, H., Application of large ceramics structures to steel manufacturing machinery, *International Journal of Engineering Innovation and Management*, **1**, pp.77-82, 2011.

[12]   Noda, N.A., Yamada, M., Sano, Y., Sugiyama, S., and Kobayashi, S., Thermal stress for all-ceramics rolls used in molten metal to produce stable high quality

galvanized steel sheet, *Engineering Failure Analysis*, **15**, pp.261-274, 2008.

[13]   Noda, N. A., Hendra, Takase, Y., and Tsuyunaru, M., Maximum stress for shrink fitting system used for ceramics conveying rollers, *Journal of Solid Mechanics and Materials Engineering*, 2(8), pp.1410-1419, 2008.

[14]   Yokoyama, N., Mori, A., Kono, M., Yoshida, M.: *Japan Patent* No. 2000-249472 (09. 14. 2000).

[15]   136th Committee Processing Technology of Japan Society of Promotion and Science.: Fine Ceramics Research Handbook. Uchida Roukakuho, Japan, (1998), 414.

[16]   Ceramics editorial committee: Mechanical properties of ceramics 3rd edition. Ceramics Association, Japan (1982), 65.

[17]   Sai, I., and Horibe, S.: Static fatigue of Ceramics and Cyclic Fatigue, Extra edition Metal, Japan (1993)

[18]   Japan Society of Mechanical Engineers Reviews: Material design of metal fatigue strength I (General, Size effect, Notch Effect), 2nd edition. JSME, Japan (2007)

[19]   129th Committee 3rd subcommittee of Japan Society of Promotion and Science.: Metal material high-temperature strength data collection Part 1 low alloy steel reviews. Yokendo, Japan (1964), 9.

[20]   Li W, Noda NA, Sakai H, and Takase Y. Analysis of Separation Conditions for Shrink Fitting System Used for Ceramics Conveying Rollers, *Journal of Solid Mechanics and Materials Engineering* 2011; 5(1): 14-24.

[21]   Truman CE, Booker JD. Analysis of a Shrink-fit Failure on a Gear Hub/Shaft Assembly, *Engineering Failure Analysis* 2007; 14: 557-572.

[22]   Antoni N, Contact Separation and Failure Analysis of a Rotating Thermo-elastoplastic Shrink-fit Assembly, *Applied Mathematical Modelling* 2003; 37: 2352-2363.

[23]   Noda, N.A., Sano, Y., Takase, Y., Harada, S., Suryadi, D., Kumasaki, S.: *Tetsu to Hagane*, **110**(2015), 284.

Chapter 4

Failure Analysis for Coming out of Shaft from Shrink-fitted Ceramic Sleeve

4.1   Introduction

Steel conveying rollers are used in the heating furnace as shown in Figure 4.1 to produce high-quality steel plates for automobiles. Figure 4.2(a) shows the conventional roller whose inside is cooled by water circulation to reduce the temperature although causing some energy loss and maintenance cost. The steel sleeve and steel shafts are usually connected by shrink fitting and bonded by welding, and the steel sleeve is coated by ceramic on the surface to improve wear resistance. However, the thermal expansion mismatch may induce surface failures such as crack, peeling, wearing resulting in short roller life [1].

Figure 4.2(b) shows a new ceramic roller consisting of steel shafts at both ends and ceramic sleeve having high heat resistance, wear resistance [2], and corrosion resistance [3]. All ceramic sleeve may prevent most of the defects observed at coated ceramic, and therefore, the roller life can be extended significantly. Since adhesive bonding and metal bonding have very low strength under high temperature, only shrink fitting can be applied for ceramic sleeve and steel shaft connection used in the heating furnace [4-7].   The thermal expansion coefficient of steel is about four times larger than that of ceramic having low fracture toughness [8, 9], attention should be paid to the risk of ceramic sleeve fracture.

In the previous study the authors have considered similar ceramic structures under high temperature environment in continuous galvanizing line [10, 11], in the continuous pickling line [12], and in the heating furnace [13]. It should be noted that only low shrink fitting ratio can be applied for those structures because of the ceramic brittleness.

As an example, similar all ceramic rolls have been successfully developed to be used in a molten metal bath in continuous galvanized steel line [9-11]; however, coming
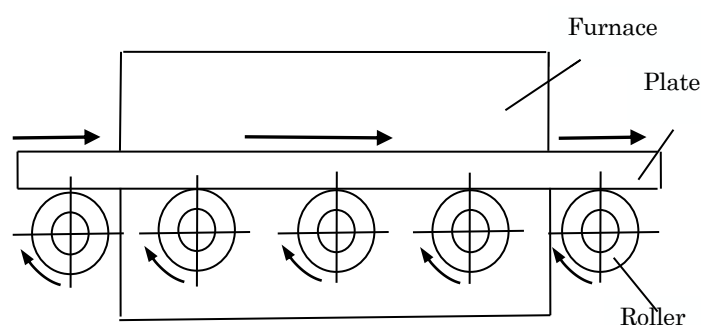
Figure 4.1 Layout of rollers in heating furnace
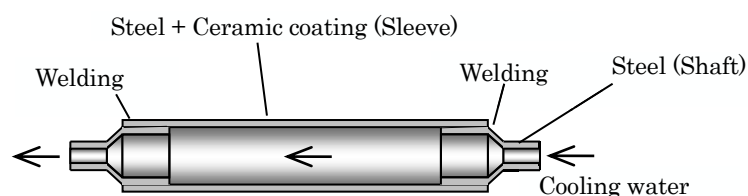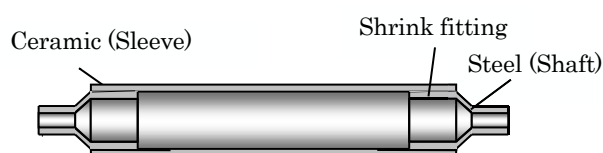
Figure 4.2 Roller structure

out of the shaft was observed several times in prototype rolls. Since sliding bearings for rolls and rollers do not restrict the axial movement of the shaft, the coming out can be problematic. Even when the shaft movement is restricted within a small allowable range, the coming out of the shaft may cause local thrust loading, frictional heat generation, and wear preventing smooth rotation of the roller. Previously, Truman and Booker investigated micro-slipping between the gear hub and shaft connected by shrink fitting [14]. Antony analyzed contact separation for rotating thermos-elastoplastic shrink fit assembly [15]. However, few failure studies are available for coming out of the shaft

from the shrink-fitted ceramic sleeve.

In this study, therefore, the coming out behavior of the steel shaft from the ceramic sleeve will be considered during operation. The finite element method is applied to simulate the behavior. Then, several mechanical factors will be considered to understand the coming out of the shaft.

4.2   Analysis conditions

4.2.1   Shrink fitting connection with roller dimensions

Figure 4.3 shows dimensions of the roller considered whose outer diameter D=300mm. Here, the roller consists of ceramic sleeve and steel shaft connected by shrink fitting. The shrink fitting ratio is defined as δ/d, where δ is the diameter difference and d is the inner diameter of the sleeve d=240 mm. The shrink fitting connection was analyzed in the previous studies [4-7, 12, 13, 16]. In ref. [4], the ceramic roller structure was studied without considering thermal stress when a ceramic sleeve and steel solid shafts are connected by shrink fitting at both ends. The results show that for larger shrink fitting ratio $\delta/d \geq 0.2 \times 10^{-3}$, the stress due to distributed load $\sigma_{\theta b}$ becomes constant independently from δ/d. The constant value coincides with the results when the sleeve and shafts are perfectly bonded. In other words, if $\delta/d \geq 0.2 \times 10^{-3}$, the sleeve and shafts can be treated as

$\delta/d=0.4 \times 10^{-3}$
μ =0.3
ν =0.28
ρ =3200 kg/mm^3
E_{sl} =300GPa
E_{sh} =210GPa
w =30N/mm
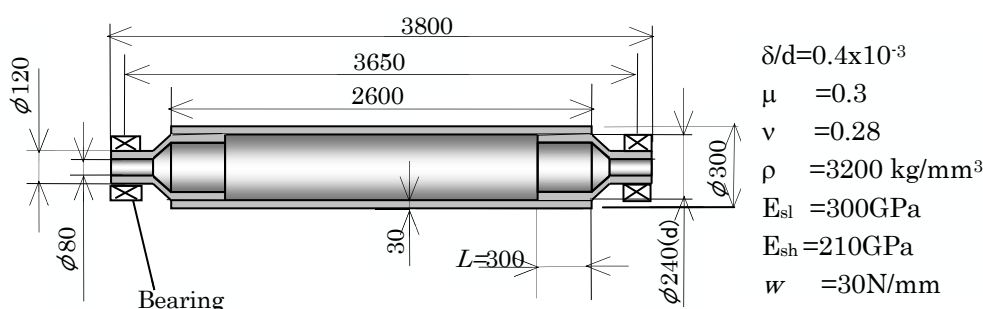
Figure 4.3 Structure and dimensions of the new roller model with standard dimensions (mm).

a unit body. Moreover, in ref. [13], the ceramic roller structure used in the heating furnace was studied focusing on thermal stress at the shrink fitting portion. The result shows that the maximum thermal stress can be reduced by using the small thickness of the steel shaft [13].

Table 4.1 shows mechanical properties of the materials. The shaft material is assumed as alloy steel, which is relatively inexpensive but tough enough, and the sleeve material is silicon nitride. Thermal expansion coefficients are also indicated in Table 4.1.

Table 4.1 Properties of materials

Properties	Ceramic	Steel
Young's modulus [GPa]	300	210
Poisson's ratio	0.28	0.3
Tensile strength [MPa]	500	600
Mass density [kg/m^3]	3200	7800
Thermal expansion coefficient [1/K]	0.3×10^{-5}	1.2×10^{-5}

4.2.2   Inertial force effect due to roller rotation

In the first place, inertial force effect during the roller rotation will be considered by assuming two-dimensional rotating disk model with a circular hole as shown in Figure 4.4. Here, the maximum rotating angular velocity ω=33 rad/s can be estimated from the data for the roughing mill [17]. Although the roller data for heating furnace are not available in [17], the carrying speed is nearly the same as the one of roughing mill. When the ceramic sleeve is rotating with the angular velocity ω, stresses $\sigma_\theta(r)$, $\sigma_r(r)$ appearing at r=r are expressed the equation (4.1) [18].

$$\sigma_\theta(r) = \frac{3+\nu}{8}\rho\omega^2 \left[b^2 + a^2 + \frac{a^2 b^2}{r^2} - \frac{1+3\nu}{3+\nu} r^2 \right],$$

$$\sigma_r(r) = \frac{3+\nu}{8}\rho\omega^2 \left[b^2 + a^2 - \frac{a^2 b^2}{r^2} - r^2 \right] \qquad (4.1)$$

where a is outer radius, b is inner radius, r is radius at the point, ν is Poisson's ratio, ρ is

a = outer radius [mm]
b = inner radius [mm]
r = radius at point [mm]
μ =0.3
ν =0.28
ρ =3200 kg/mm³
ω = angular velocity [rad/s]
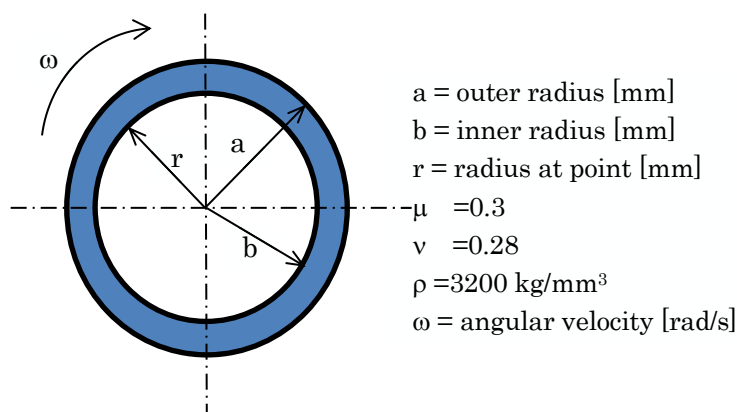
Figure 4.4 Two-dimensional of rotating disk with a circular hole

mass density. By substituting b=120mm, a=150mm, r=b=120mm, ν=0.28, ρ=3200 kg/mm³ in Fig. 3 into (4.1), we have $\sigma_\theta(b)$=0.073MPa, $\sigma_r(b)$=0 and radius expansion $\Delta b=\varepsilon_\theta \cdot b=\sigma_\theta(b)/E_{sh}$=2.94x10⁻⁵ mm.

Here we only consider the ceramic sleeve rotation without considering the shaft rotation to estimate the dynamic effect safely. Due to the inertial force effect, the inner radius of the ceramic sleeve may expand only Δb=2.94x10⁻⁵ mm. Then the shrink fitting ratio may be reduced by only 0.12%. Since the inertial force can be neglected, a quasi-static analysis will be proposed in the following section.

4.2.3 Coming out simulation for the rotating roller

In this study, the coming out of the shaft will be realized on the numerical simulation. Here, the coming out of the shaft is considered under room temperature because the coming out occurs more easily. When we consider the roller in the heating furnace, equivalent shrink fitting ratios may be applied by considering the shaft expansion because the thermal expansion coefficient of the steel shaft is four times larger than the one of ceramic (see Table 4.1). Here, the shrink fitting ratio is considered in the range δ/d=0.01x10⁻³-1.0x10⁻³ at room temperature.

Figure 4.5 shows the roller rotation under loading where Point A located at the bottom of the shaft moves to the top after rotating 180° as shown in Figure 4.5(b). To simulate the coming out behavior, the roll rotation is replaced by shifted load w in the

circumferential direction on the fixed roll as shown in Figure 4.6. The roller is subjected to distributed load w=30N/mm as the weight of the conveyed steel assuming the shaft ends are simply supported. As shown in Figure 4.6, the continuous load shifting can be replaced by discrete load shifting with load shift angle θ_0, which is usually used as a standard discretization numerical analysis. The suitable shift angle will be considered with the numerical results in section 3.3. In other words, the rotation of the roller under loading is replaced by the non-rotating roller subjected to load shifting in the circumferential direction. Then, to obtain the solution numerically, the continuous load shifting is replaced by discrete load shifting in the circumferential direction at the interval θ_0. Here, the initial load position θ_0=0° is corresponding to number of cycle N=0, and θ=360° is corresponding to number of cycle N=1.
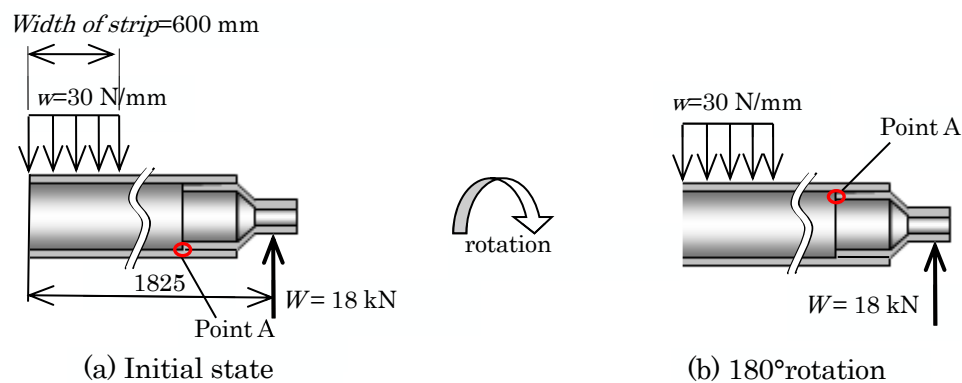
Figure 4.5 Dimensions and loading condition of new roller
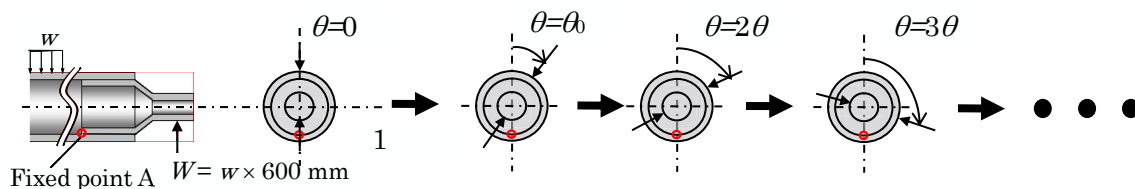
Figure 4.6 Rotation of the roller replaced by the shifted load at the interval of the load shift angle θ_0. When θ=0° number of cycle N=0, and when θ=360° number of cycle N=1.

Figure 4.7 shows the load conditions. Here, a sliding bearing is assumed for the model, which does not constrain the shaft movement. Due to the symmetry Figure 4.7 shows the half model considered with the total number of element 154 320.The smallest element size at the contact portion between sleeve and shaft is 1.25mm x 1.25mm x 6mm. Static structural analysis is performed to the roller by using MSC Marc Mentat 2011 [19] with full Newton-Raphson iterative sparse solver of multifrontal method. In this study, a three-dimensional elastic FEM analysis can be applied because the loading condition does not exceed the yielding stress for the steel shaft, and the macroscopic plastic deformation does not appear for ceramic sleeve until failure.

The effect of the torsional load at the contact portion can be ignored because the shear stress $\tau_{r\theta}$ is very small compared to the shear stress τ_{rz} [13]. In contact analysis, it is known that two types of friction models, that is, stick-slip model and bilinear model have good accuracy [19]. However, since the stick-slip model needs large amount of data to determine friction force during repetitive calculation process, in this study the bilinear model is applied where the friction force is simply determined from the displacement. The friction coefficient between sleeve and shaft at joint portion is assumed as $\mu=0.3$. All conditions above are used as a reference condition.
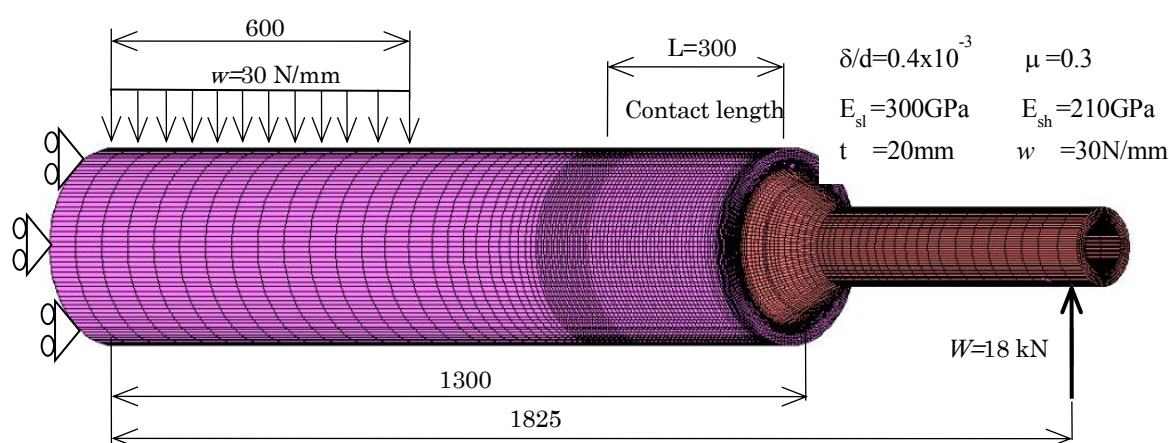
Figure 4.7 Standard half model with FEM mesh.

4.3 Evaluation for the coming out and deformation of the shaft due to the distributed load and shrink fitting

4.3.1 Deformation and stresses of the shaft caused by shrink fitting

In order to consider coming out behavior, the shaft deformation due to shrink fitting is investigated in the first place. Figure 4.8 illustrates the shaft deformation with the (r,z) coordinate defined before shrink fitting. The displacement u_{zC} in the z-direction is determined from the values at 4 points as $u_{zC}^{sh}=(u_{zA}^{sh}+u_{zA'}^{sh}+u_{zB}^{sh}+u_{zB'}^{sh})/4=u_{zA}^{sh}<0$ as shown in Figure 4.8(a). Then, since the shaft is under compression in the r-direction; we have $u_{zA}^{sh}=u_{zC}^{sh}<0$.

(a) Displacement due to shrink fitting $u_{zC}^{sh}=(u_{zA}^{sh}+u_{zA'}^{sh}+u_{zB}^{sh}+u_{zB'}^{sh})/4$

(c) Stress τ_{rz} due to shrink fitting

(b) Stress σ_r due to shrink
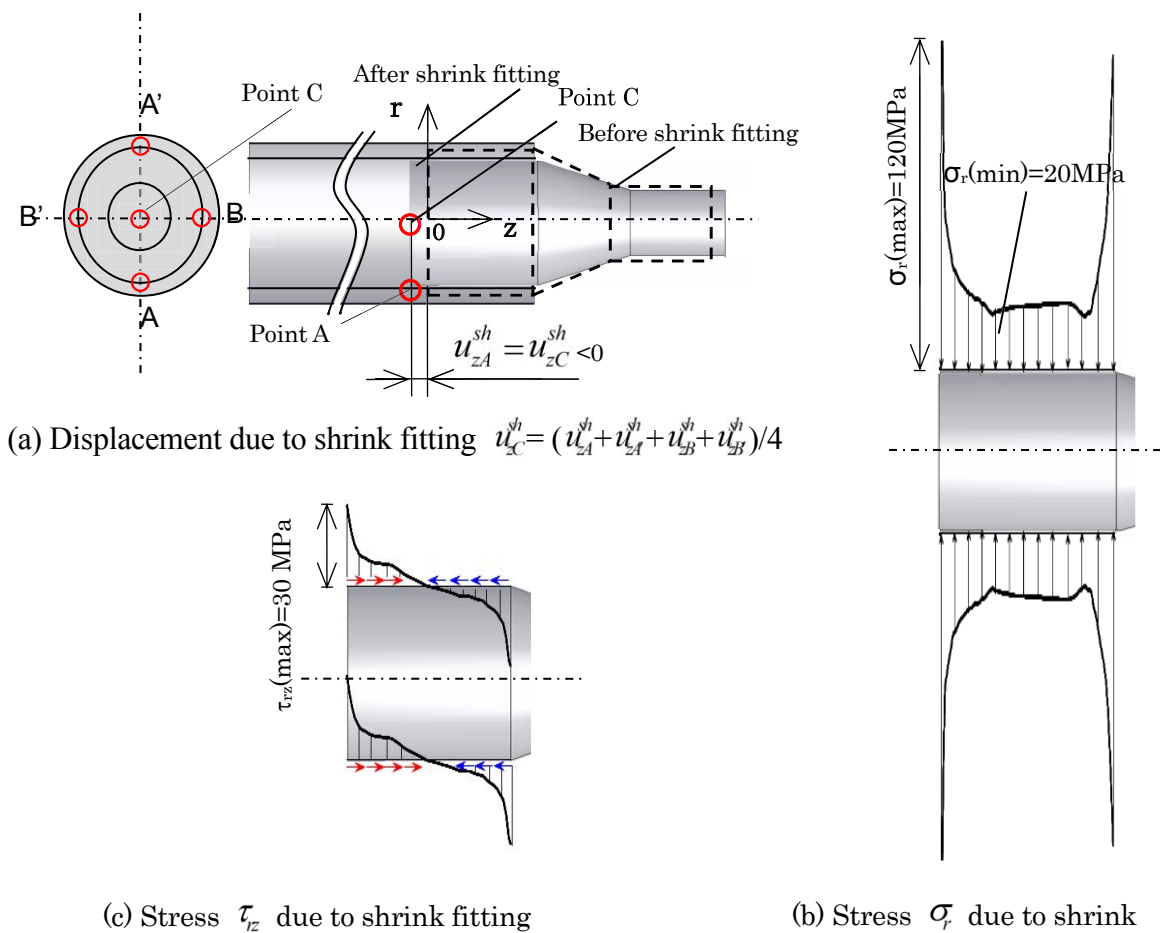
Figure 4.8 The z-displacement and stress of the shaft due to shrink fitting

Figure 4.8(b) shows stress σ_r distribution appearing along the contact surface due to shrink fitting with the maximum compressive stress σ_r=120MPa. Figure 4.8(c) shows shear stress τ_{rz} distribution due to shrink fitting with the maximum stress τ_{rz} = 30MPa. The shaft is extended in the z-direction by the compressive stress σ_r due to shrink fitting, but the shear stress τ_{rz} may prevent the elongation. Since the shaft end surface tends to be significantly deformed by the compressive stress, the maximum shear stress may be important.

4.3.2 Displacement and deformation of the shaft due to the initial load

Figure 4.9(a) shows the shaft after several number of loading cycle N, which defines displacement u_{zA} at point A and u_{zC} at point C in the (r,z) coordinate. Figure 4.9(b) shows the shaft due to initial distributed load N=0 focusing on the displacement $u_{zA}^{N=0}$. As shown in Figure 4.9(b), positive displacement $u_{zA}^{N=0}$ ($>0>u_{zA}^{sh}$) appears at point A although the displacement due to shrink fitting was negative u_{zA}^{sh} <0 as shown in Figure 4.8(a). On the other hand, at point C, displacement $u_{zC}^{N=0}$ ($> u_{zC}^{sh}$) appears but usually

(a) Definition of z-displacement u_{zA}, u_{zC} after several number of cycle N

(b) The z-displacement due to shrink fitting and initial load
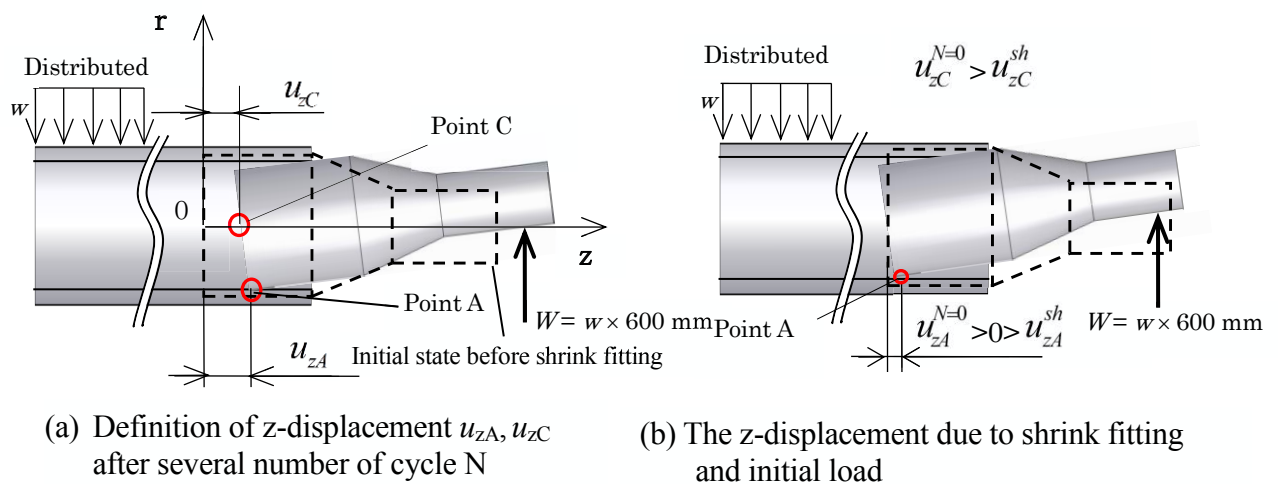
Figure 4.9 The z-displacement of the shaft due to bending load

still negative $u_{zC}^{N=0} < 0$. Those values $u_{zA}^{N=0}$ and $u_{zC}^{N=0}$ are defined as the initial displacement at N=0 considering both shrink fitting and initial loading.

Figure 4.10 and Figure 4.11 show the results of u_{zA} for extremely small δ/d =0.01×10^{-3} and for standard δ/d =0.2×10^{-3}. Here, friction coefficient μ=0.3 during N=0 to N=3 and load shift angle θ_0=30° is applied. In Figure 4.10, Point a' refers to the displacement of shaft due to shrink fitting, while point a represents the initial displacement of the shaft at N=0. Under the small shrink fitting ratio in Figure 4.10, the average value of u_{zA} at each cycle increases with increasing N. Under the standard shrink fitting ratio in Figure 4.11, the average value of u_{zA} at each cycle is almost constant although the amplitude of u_{zA} increases slightly with increasing N.

Next, the positions of peak and valley of u_{zA} are considered. Figure 4.10 shows the angle of rotation at point (a), (b), (c), and (d). It is seen that the peak occurs at each
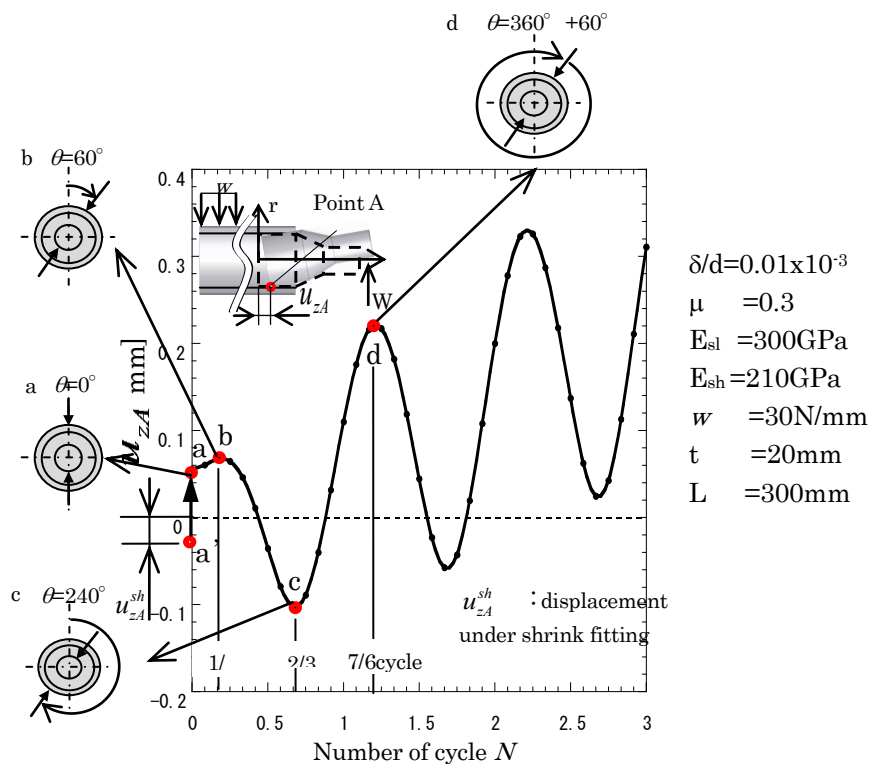
Figure 4.10 The z-displacement at point A u_{zA} vs. number of cycle N for δ/d=0.01×10^{-3} and μ=0.3when θ_O＝30°

number of cycle $N\cong n+1/6$ (n=0,1,2,..) corresponding to the rotation angle $\theta\cong 2\pi n+\pi/3$, while the valley occurs at each number of cycle $N\cong n+2/3$ (n=0,1,2,..) corresponding to rotation angle $\theta\cong 2\pi n+4\pi/3$. In other words, the peak and valley do not occur at $\theta=0°$ and $\theta=180°$. This is because the relative displacement between the sleeve and shaft cannot follow the load direction change immediately due to the irreversible effect of friction force.

Figure 4.10 shows displacement u_{zA} of the shaft under low shrink fitting ratio δ/d =0.01×10^{-3}. It is seen that the average displacement u_{zA} increases in the z-direction with increasing the cycle N, that is, the shaft moves in the coming out direction. Under large shrink fitting ratio δ/d =0.2×10^{-3} in Figure 4.11, although the amplitude of displacement u_{zA} slightly increases with increasing N, the coming out is not seen.

Next, the displacement at point C is considered since at the central point C the cyclic change does not appear. Figure 4.12 shows the displacement u_{zC} at point C, which
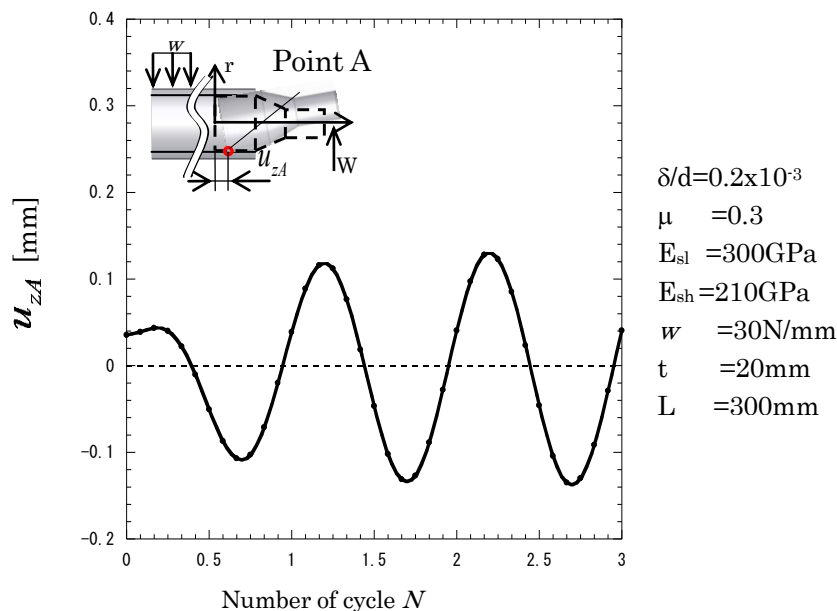
Figure 4.11 The z-displacement at point A u_{zA} vs. number of cycle N for δ/d=0.2×10^{-3} and μ=0.3when θ_A＝30°.
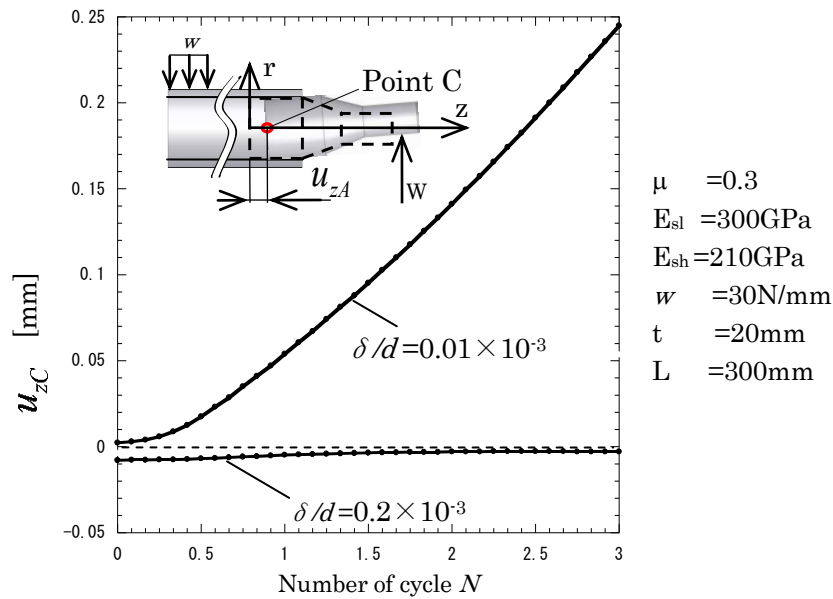
Figure 4.12 The z-displacement at point C u_{zC} vs. number of cycle N for different shrink fitting ratio when $\theta_0 = 30°$.

increases slightly at the beginning and increases significantly later under $\delta/d = 0.01 \times 10^{-3}$. On the other hand, the displacement u_{zC} increases slightly at first and becomes constant under $\delta/d = 0.2 \times 10^{-3}$. The possibility of the coming out of the shaft looks small in this case.

4.3.3 Load shifting angle θ_0 selection

In this study, the roller rotation under bending load is replaced by the non-rotating roller subjected to the load shifting in the circumferential direction. As a standard method of discretization in numerical analysis, the continuous load shifting can be expressed by discrete loads at a certain interval θ_0. Here, a smaller angle θ_0 provides accurate results but large computational time. Therefore, the optimal angle θ_0 should be discussed by investigating u_{zC} with varying the shift angle, $\theta_0 = 30°$, $\theta_0 = 18°$, $\theta_0 = 12°$, and $\theta_0 = 6°$.

Figure 4.13 shows u_{zA} under $\delta/d = 0.2 \times 10^{-3}$ with varying θ_0. Figure 4.13 shows that smaller θ_0 provides the results for smaller amplitude of u_{zA}. However, the results converge if $\theta_0 \leq 12°$. Discrete load shift angle $\theta_0 = 12°$ provides 30 data in one cycle, which
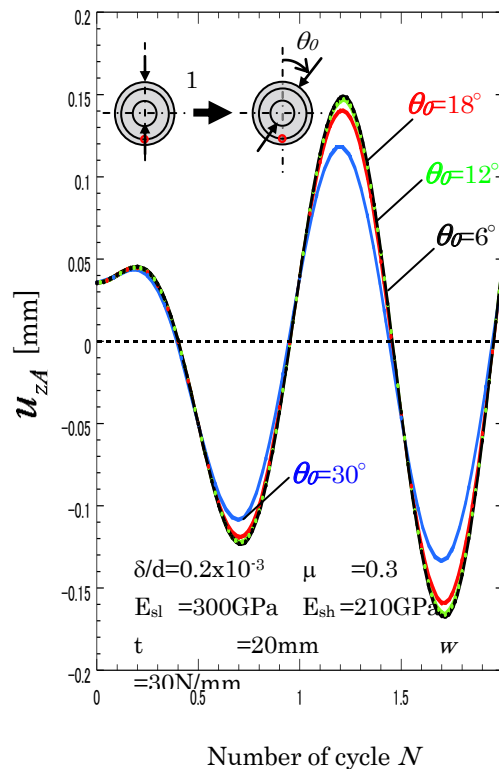
Fig.4.13 The z-displacement at point A vs. number of cycle N for different θ_0 at $\delta/d = 0.2 \times 10^{-3}$ and μ=0.3

is enough number to present continuous displacement as shown in Figure 4.13. Figure 4.14 shows u_{zC} focusing on the coming out behavior. Although the result for θ_0=30° is very different from others, the results for θ_0=6° and θ_0=12° almost coincide with each other. Since the effect of discrete load shifting is less than 1% if $\theta_0 \leq 12^o$, it may be concluded that load shifting angle θ_0=12° is the most suitable to reduce large calculation time without losing accuracy. In the following calculation load shift angle θ_0=12° will be used consistently.

4.4 Effect of mechanical properties on the coming out

In this chapter, effects of several fundamental parameters, such as the shrink fitting ratio, magnitude of the load, Young's modulus, and friction coefficient are considered for the standard model whose geometry of the roller is fixed. Here, the standard model has the following:
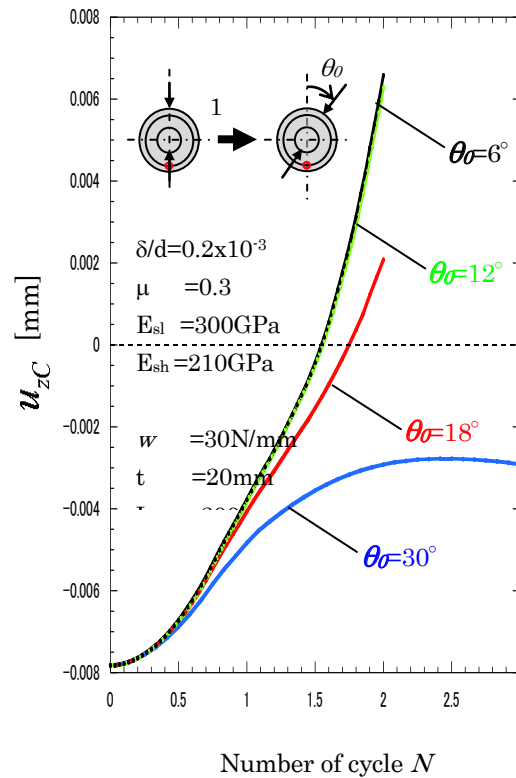
Figure 4.14 The z-displacement at center point C vs. number of cycle N for different θ_0 when $\delta/d = 0.2 \times 10^{-3}$ and $\mu=0.3$

the shrink fitting ratio $\delta/d = 0.4 \times 10^{-3}$

the contact length L=300mm,

the friction coefficient between sleeve and shaft $\mu = 0.3$,

the sleeve thicknesses T=30mm,

the shaft thickness t=20mm,

the distributed load on the roller surface is about w=30N/mm,

Young's modulus of the ceramic sleeve $E_{sl} = 300$GPa,

Young's modulus of steel shaft $E_{sh} = 210$GPa.

4.4.1   Effect of shrink fitting ratio

In this study, the shrink fitting ratios are considered in the range $\delta/d=0.01 \times 10^{-3}$-$1.0 \times 10^{-3}$. Here, $\delta/d=0.01 \times 10^{-3}$ is an example of low shrink fitting ratio.

Next, δ/d =0.1×10^{-3}, 0.2×10^{-3}, 0.4×10^{-3} may be used for real ceramic roller. Finally, δ/d =1.0×10^{-3} is an example of a larger shrink fitting ratio used for steel rollers.

Figure 4.15(a) shows the results for u_{zC}. With increasing the shrink fitting ratio, the compressive stress increases causing the negative initial value of u_{zC} as shown in Figure 4.15(a) at N=0. Under low shrink fitting ratio, displacement u_{zC} increases significantly with increasing N. The coming out speed is shown in Figure 4.15(b). To clarify the coming out behavior, the speed of the coming out is defined as ($u_{zC}|_N-u_{zC}|_{N-0.5}$)/0.5. Under δ/d =0.01×10^{-3}-0.1×10^{-3}, the speed increases with increasing N at N=0-5. Under δ/d =0.2×10^{-3} the coming out speed is small, then increases after N=4. Under δ/d =0.4×10^{-3} although the speed increases slightly at the beginning, but after N=3

(a) u_{zC} vs. number of cycle N   (b) Speed of the coming out
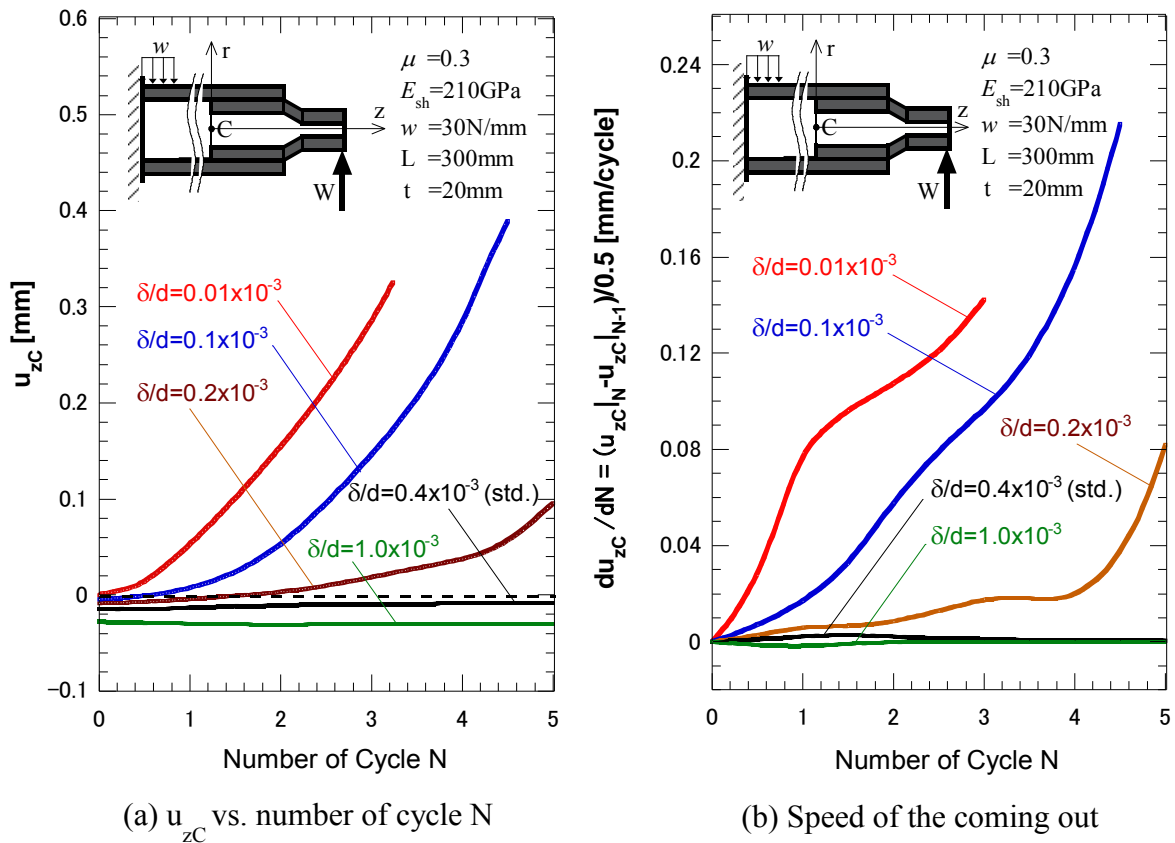
Figure 4.15 Effect of the shrink fitting ratio on the coming out of the shaft

the speed becomes almost zero. Under $\delta/d = 1.0 \times 10^{-3}$ the displacement u_{zC} is always negative and the speed is always zero independent of N. In the following analysis $\delta/d = 0.4 \times 10^{-3}$ is considered as a reference condition.

4.4.2   Effect of the magnitude of the load

Distributed load w=30N/mm is applied to the sleeve from conveyed steel as shown in Figure 4.7. In Figure 4.16 the effects of the magnitude of load is investigated for w=15, 45, 60N/mm. The coming out speed significantly increases with increasing the magnitude of the load. It is seen that the coming out accelerates at N=0-4. In other words, the coming out easily occurs when distributed load $w \geq 45$N/mm.
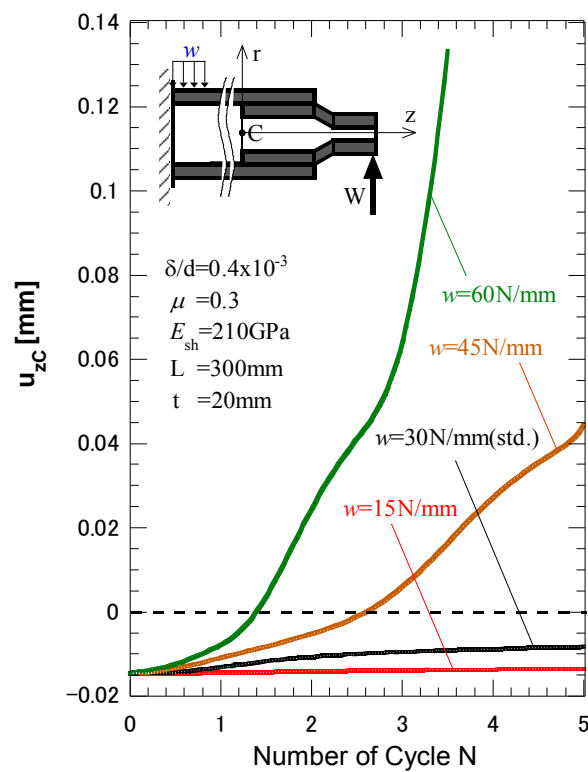
Figure 4.16 Effect of distributed load when $\delta/d = 0.4 \times 10^{-3}$

4.4.3   Effect of Young's modulus of the Shaft

Figure 4.17 shows the effect of Young's modulus of the shaft. Three types of Young's modulus are considered, namely E_{sh} = 210GPa corresponding to steel, E_{sh} = 300GPa corresponding to the silicon nitride ceramic, and E_{sh} = 100GPa corresponding to flake graphite cast iron. The smaller Young's modulus causes larger displacement u_{zC} as well as the larger initial value in the negative at N=0 as shown in Figure 4.17 because of the larger deformation of the shaft. It is seen that when Young's modulus of shaft $E_{sh}\leq$100GPa, u_{zC} increases significantly with increasing number of cycle N.

4.4.4   Effect of the friction coefficient

Figure 4.18 (a) shows the effect of the coefficient of friction between the ceramic sleeve and steel shaft. The displacement u_{zC} increases with increasing N especially under
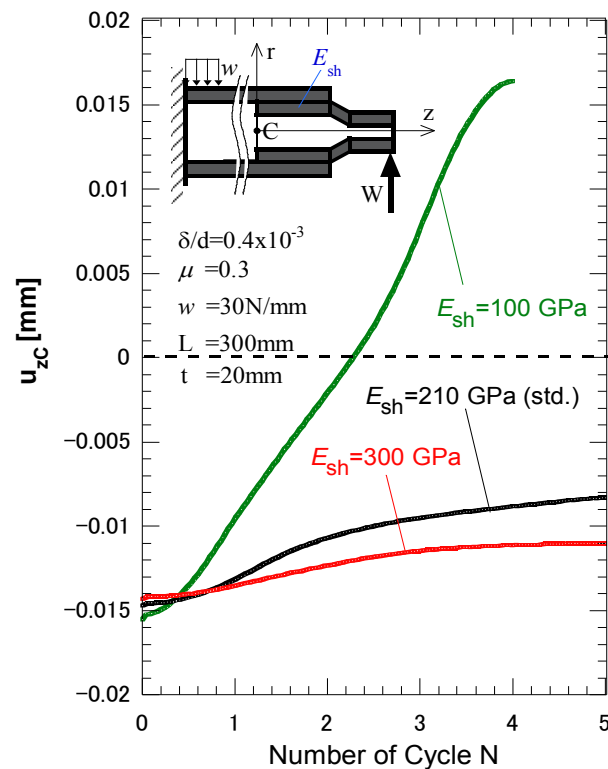
Figure 4.17 Effect of Young's modulus of the shaft
when δ/d=0.4×10^{-3}

smaller value of μ. However, when μ=0.1, the behavior of u_{zc} is quite different from others because u_{zc} has a peak at N=1.5 and increases again at N=2.5 and finally increases rapidly after N=3. Figure 4.18(b) shows the coming out speed clearly although most of the speed is nearly zero except for the result of μ=0.1 after N=3. Figure 4.18 indicates that when μ≤0.1 the coming out happens very easily.

4.5   Effect of shaft geometry on the coming out
4.5.1   Effects of the shaft thickness

In the real ceramic rollers, the shaft should be designed so as to prevent the coming out. The effect of shaft geometry is considered in this chapter. Similar to the previous discussion of the shaft Young modulus, the rigidity of the shaft can be also

(a) u_{zC} vs. number of cycle N   (b) Speed of the coming out
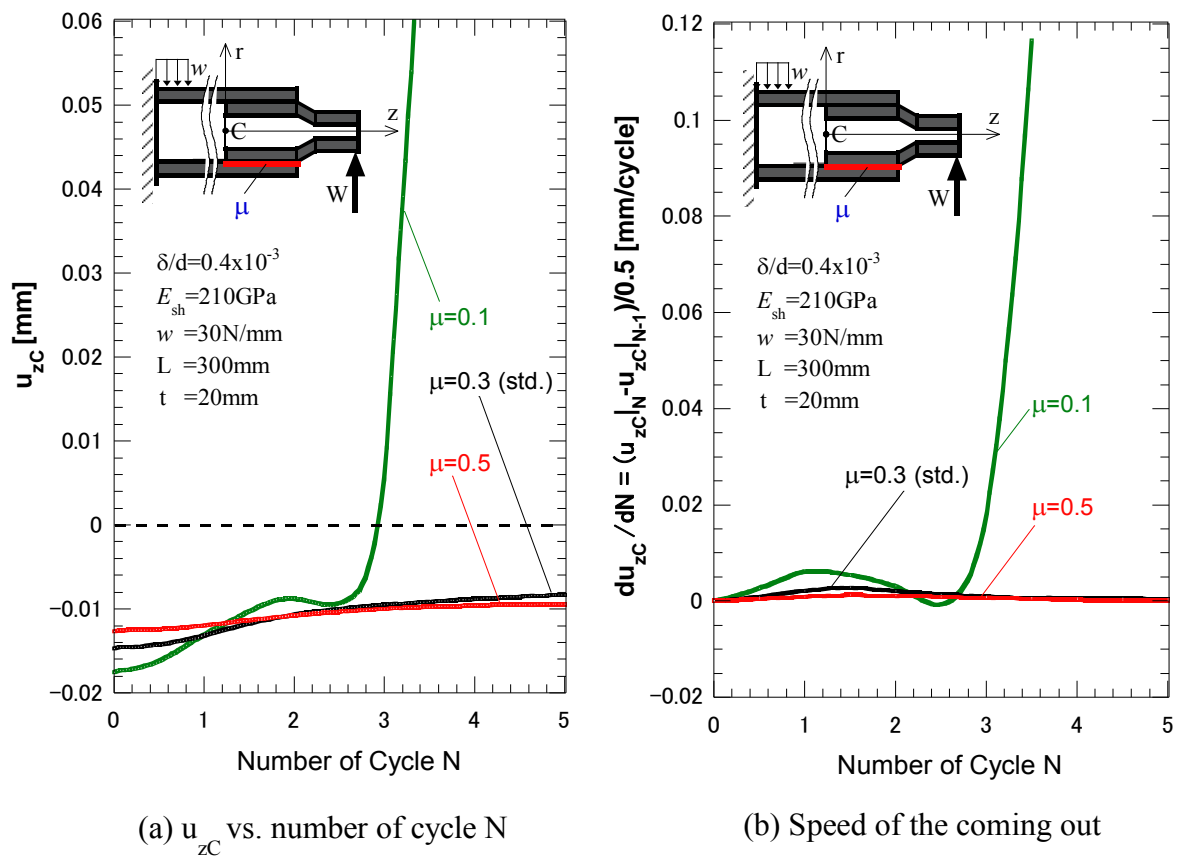
Figure 4.18 Effect of friction coefficient when δ/d=0.4×10⁻³

considered by varying the shaft thickness t. Figure 4.19(a), (b) show the results for different shaft thickness t=10mm, t=20mm, t=40mm under δ/d =0.4×10^{-3}. It is seen that u_{zC} becomes larger for smaller thickness t. The difference between the results for t=10mm and t=20mm is much larger than the one for t=20mm and 40mm. For t=10mm, the coming out speed tends to increase during N=0-4 but becomes stable at about 0.02mm/cycle after N=4. Therefore Figure 4.19(b) suggests that steady coming out may appear if the number of cycle N is large enough. Since the coming out speeds for t=20 and t=40mm are very small, the rigidity may be enough to prevent the coming out. From Figure 4.19(a) and 4.19(b), it may be concluded that when t≤10mm the coming out occurs.

(a) u_{zC} vs. number of cycle N   (b) Speed of the coming out
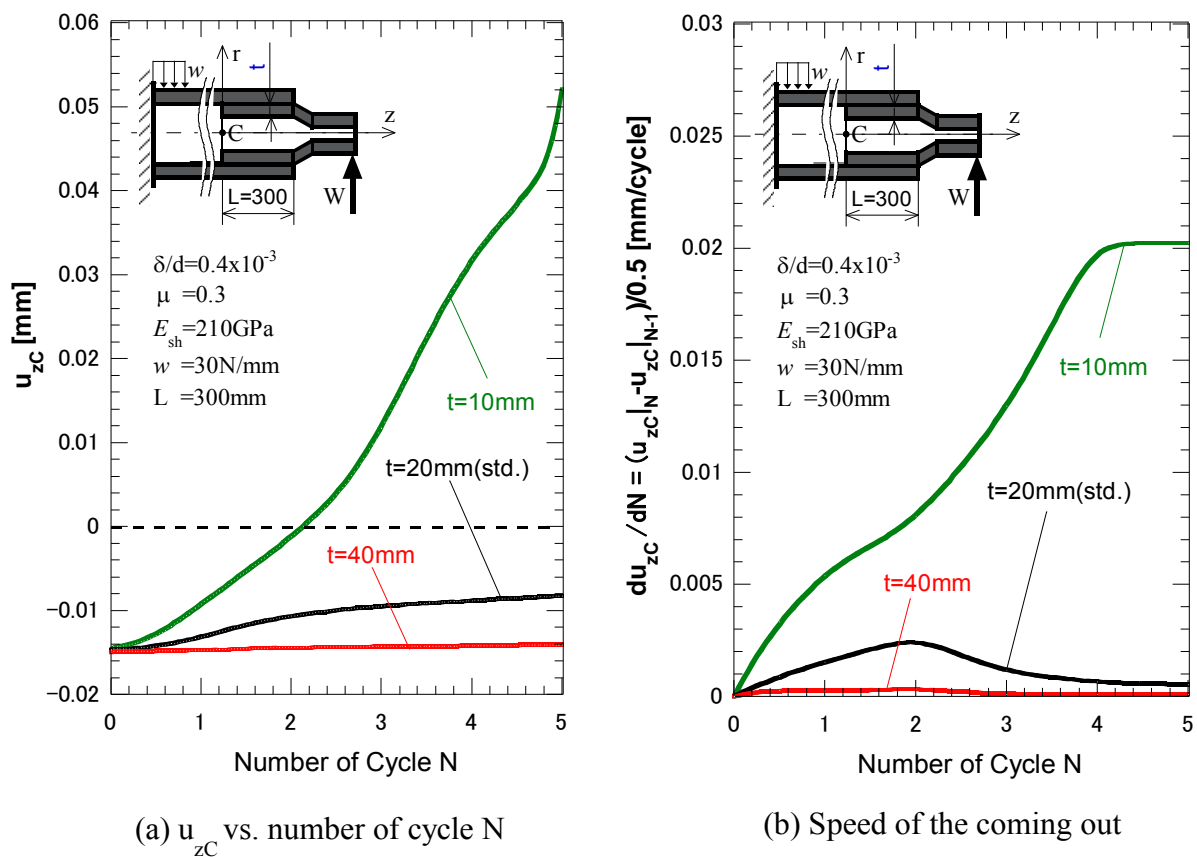
Figure 4.19 Effect of the contacted shaft thickness when δ/d=0.4×10^{-3} and μ=0.3

4.5.2 Effects of the contact length of the shaft

The standard model has contact length L=300mm. To investigate the effect of L on u_{zC}, Figure 4.20(a) shows the results for L=120mm, L=150mm, L=240mm, L=480mm. Figure 4.20(a) shows when L is smaller, the displacement u_{zC} becomes larger. This is due to the larger contact length L having larger friction force.

Figure 4.20(b) shows the speed of the coming out. To clarify the coming out behavior, the speed of the coming out of the shaft is defined as $(u_{zC}|_N - u_{zC}|_{N-0.5})/0.5$. The speed of the coming out becomes steady if N is large enough except for L=150. For L=450mm, the speed is zero from N=0. And for L=300mm, the steady speed appears after N=3. The results for L=480mm and L=300mm indicate that the coming out is hard to occur. On the other hand, the speed increases with increasing number of cycle for L=225mm and L=150mm after N=4, which means the coming out occurs easily.

(a) u_{zC} vs. number of cycle N
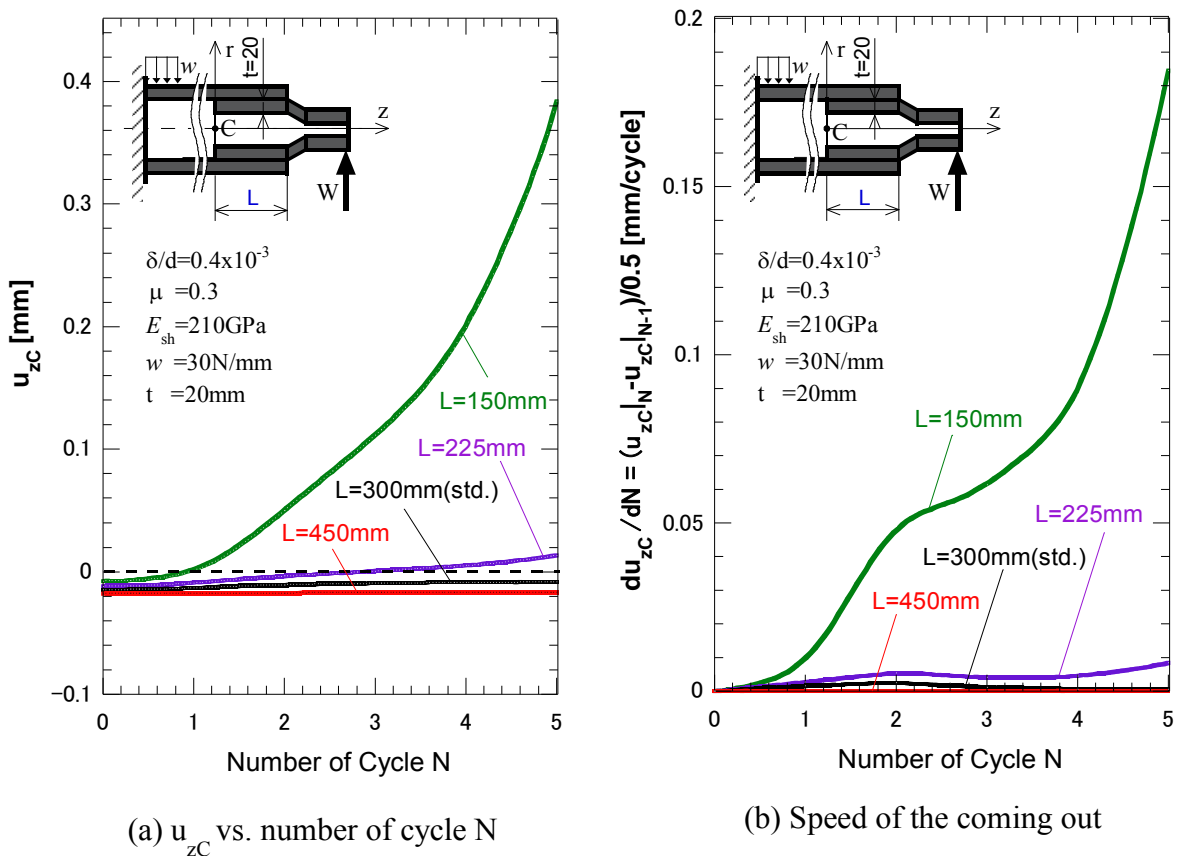
(b) Speed of the coming out

Figure 4.20 Effect of the contact length when $\delta/d=0.4\times10^{-3}$ and $\mu=0.3$

4.6 The coming out mechanism

The coming out of the shaft has been realized in the numerical simulation as shown in previous chapters. The results are different depending on the shrink fitting ratio and other parameters. Since it is difficult to obtain the results for large number N because of large calculation time, it is desirable that we can judge the coming out appears or not even when N is small. In this chapter, the coming out mechanism is considered by focusing on the stress distribution appearing at the contact portion.

4.6.1 Investigation of shear stress τ_{rz} at contact portion due to small friction coefficient

Effects of the mechanical properties and shaft geometry on the coming out have been investigated in section 4.4 and 4.5. However, the unique result appears for small friction coefficient effect as shown in Figure 4.18. Here, the result for $\mu=0.1$ shows that the behavior of u_{zc} is quite different from others. This phenomenon is interesting to be investigated.

To understand the result for $\mu=0.1$ in Figure 4.18, shear stress τ_{rz} is investigated along the contact surface. Figure 4.21 shows the shear stress distribution at the lower portion $\tau_{rz}(z)|_{\theta=180°}$ for different N. Note that the value of $\tau_{rz}(0)|_{\theta=180°}$ increases with decreasing the FEM mesh size, but if $z \geq 4mm$ the value of $\tau_{rz}(z)|_{\theta=180°}$ becomes mesh-independent. Figure 4.22 shows the value of $\tau_{rz}(z=5mm)|_{\theta=180o}$ for friction coefficient $\mu=0.1, 0.3, 0.5$. Differently from the results for $\mu=0.3, 0.5$, the shear stress for $\mu=0.1$ becomes zero after N=3. It should be noted that the average value of shear stress $\tau_{rz}(z)|_{\theta=180°}$ is nearly zero after N=3. Since the average value is nearly zero, the coming out of the shaft occurs easily without resisting the friction force due to small μ.
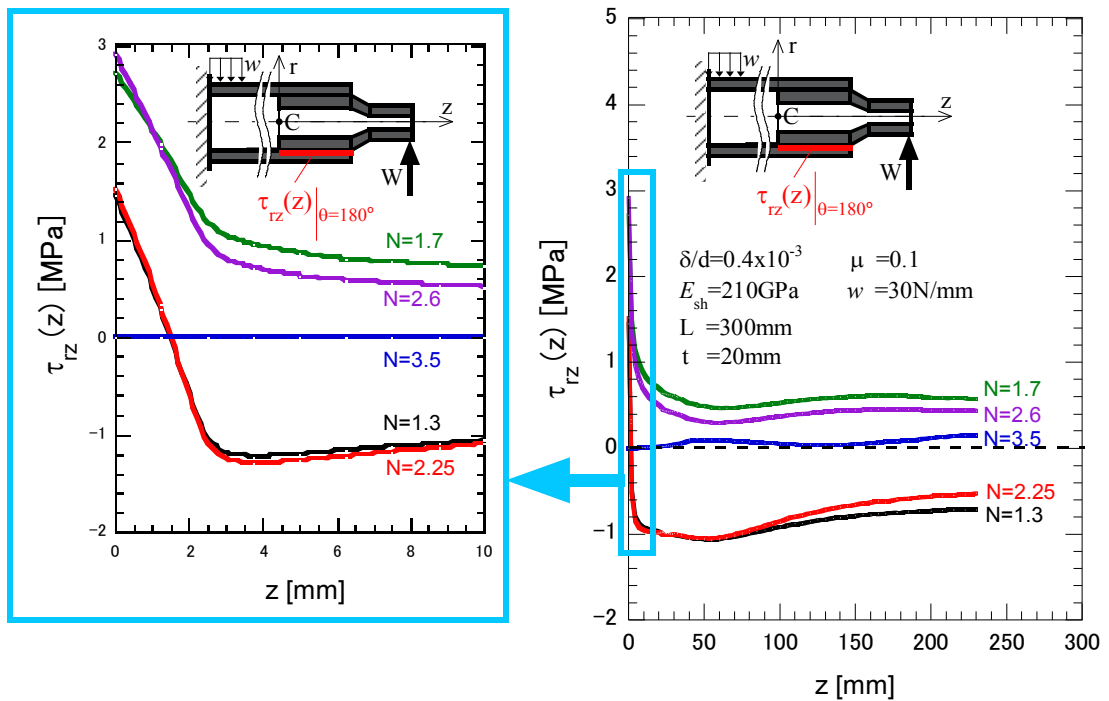
Figure 4.21 Shear stress distribution along contact portion with variation of number of cycle N when δ/d=0.4×10⁻³ and μ=0.3
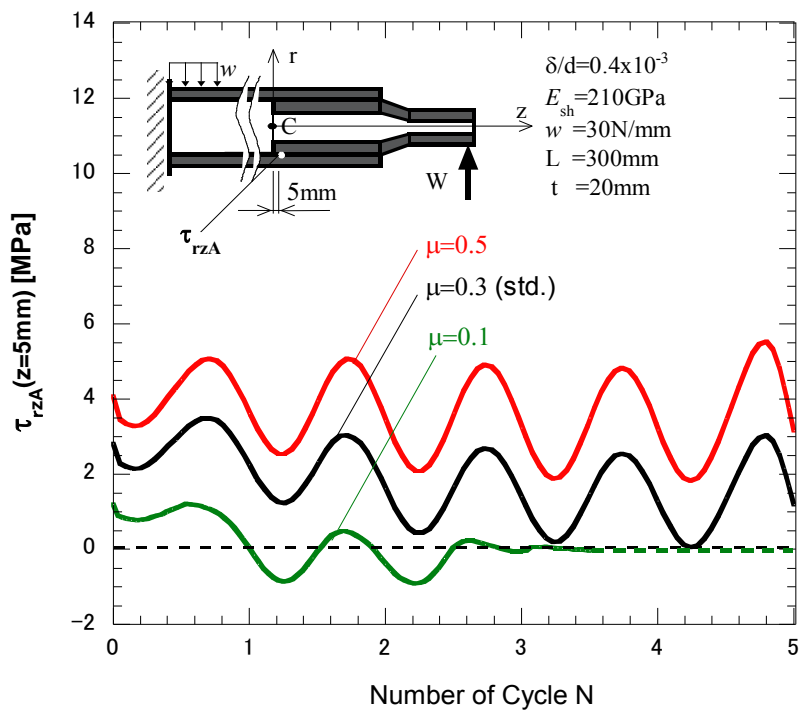
Figure 4.21 Shear stress τ_{rzA} vs. number of cycle N when δ/d=0.4×10⁻³ and μ=0.3

4.6.2   The coming out judgement based on shear stress distribution along contact surface

Figure 4.23 shows shear stress distribution τ_{rz} along the shaft half surface for θ =0°~180° when N=3. Figure 4.23(a) shows shear stress distribution under low shrink fitting ratio δ/d =0.01×10^{-3} where the coming out is likely to occur, and Figure 4.23(b) shows the result under large shrink fitting ratio δ/d =1.0×10^{-3} used for steel components. Figure 4.23 shows the stress distributions are very different each other. For example, in

(a) δ/d =0.01×10^{-3}
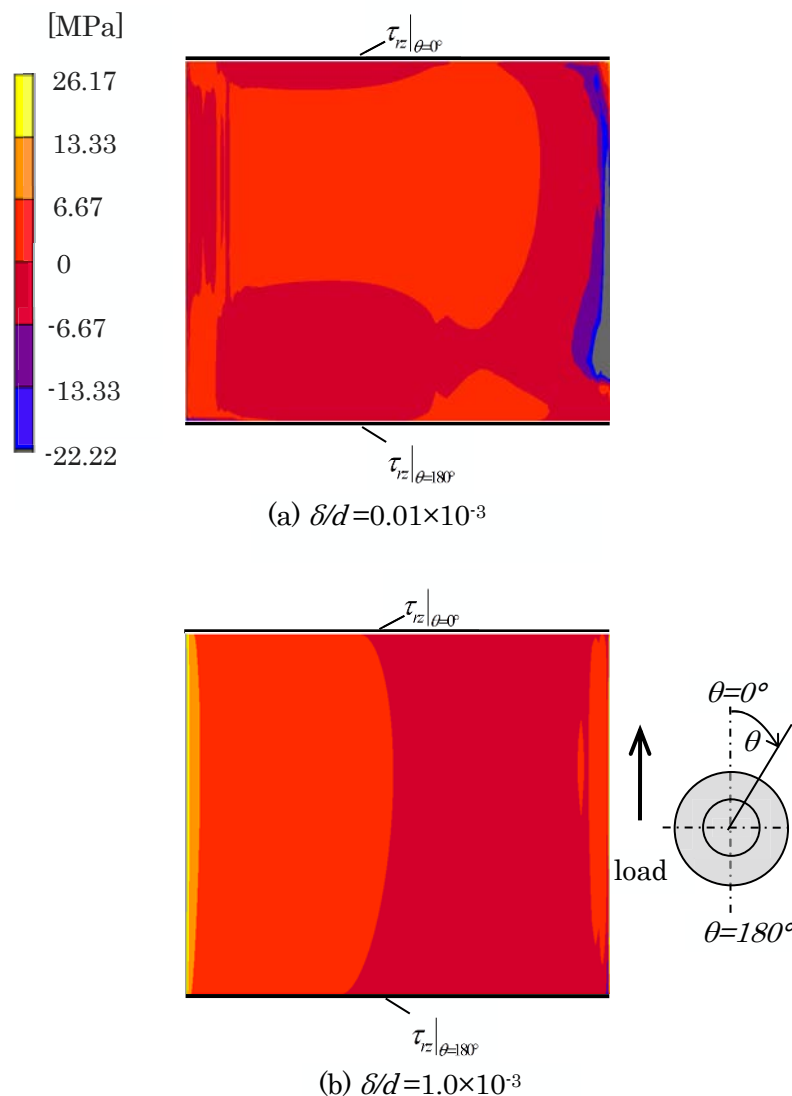
(b) δ/d =1.0×10^{-3}

Fig.23   Shear stress distribution τ_{rz} from θ=0° to θ=180° at N=3 for (a) δ/d =0.01×10^{-3} and (b) δ/d =1.0×10^{-3}.

Figure 4.23(a), shear stress τ_{rz} changes in the circumferential direction quite largely. On the other hand in Figure 4.23(b), shear stress τ_{rz} does not change in the circumferential direction. The stress variation in Figure 4.23(a) is due to the effect of the bending load. Figure 4.23(b) is depending on the large shrink fitting stress with small effect of bending load.

Figure 4.24(a) focuses on the stresses along the lines $\theta=0^{\circ}$ and 180°. Here, $\tau_{rz}|$

Fig.24   Shear stress distribution τ_{rz} from $\theta=0°$ to $\theta=180°$ at shrink fitting and N=3 for (a) $\delta/d =0.01\times10^{-3}$ and (b) $\delta/d =1.0\times10^{-3}$.

$\theta=0°$ and $\tau_{rz}\big|_{\theta=180°}$ are compared between N=0 and 3 under δ/d =0.01×10^{-3}. The shear stress due to shrink fitting is approximately equal to zero except at both ends when N=0. Therefore, when N=3, the shear stress at shrink fitting is greatly changed, and the shear stress directions are reversed at both shaft ends. The shear stress at the left end tries to prevent the coming out of the shaft.
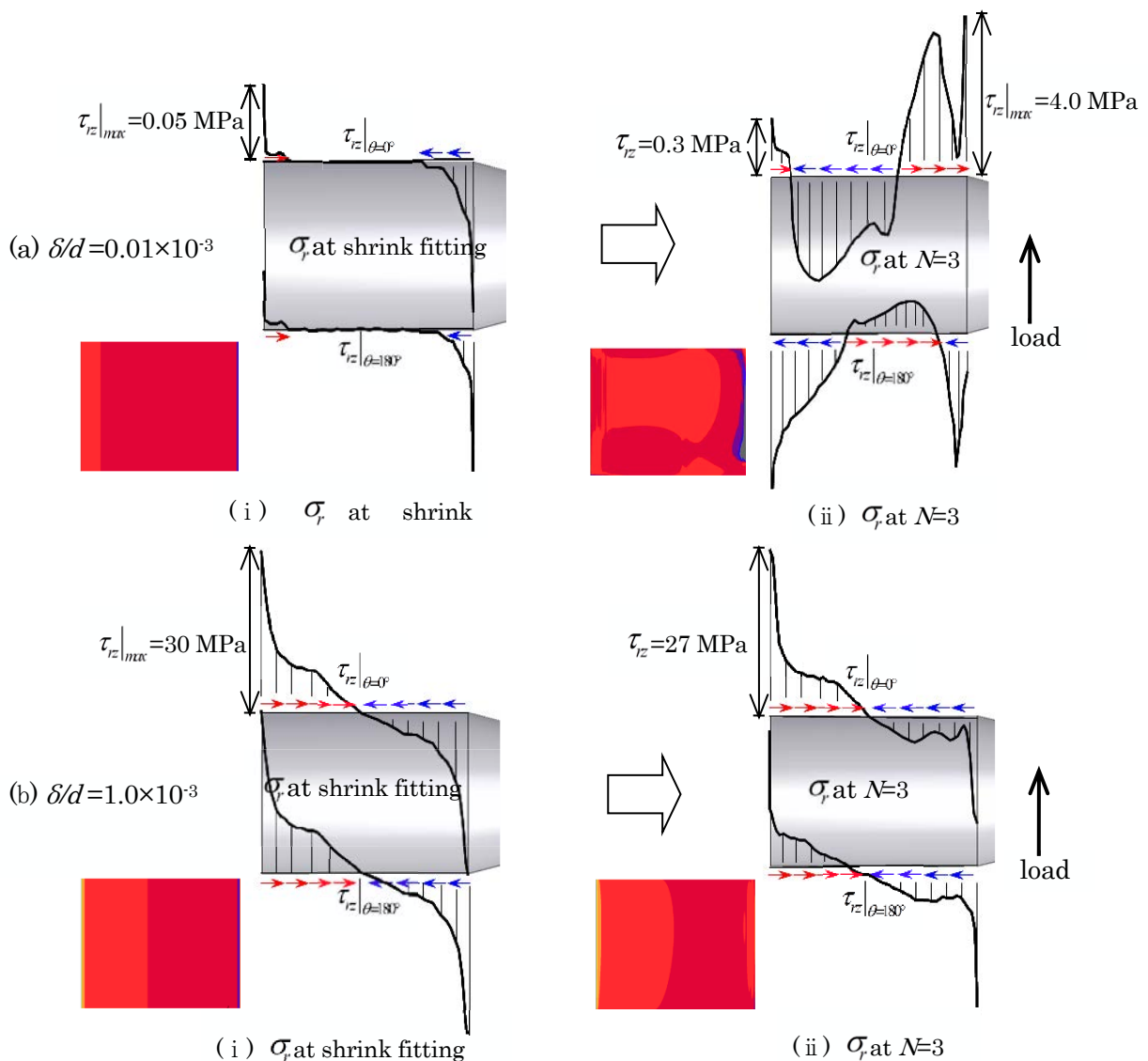
In Figure 4.24(b), $\tau_{rz}\big|_{\theta=0°}$ and $\tau_{rz}\big|_{\theta=180°}$ are compared between N=0 and N=3 under δ/d =1.0×10^{-3}. When N=0, it is seen maximum value $\tau_{rz}\big|_{max}$=30 MPa is about 600 times larger than maximum value $\tau_{rz}\big|_{max}$=0.05 MPa in Figure 4.24(a). Although not indicated, the maximum compressive stress in Figure 4.24(b) is about 180 times larger than the maximum compressive stress in Figure 4.24(a). Due to those large shrink fitted stresses, as shown in Figure 4.24(b), the effect of the bending load becomes smaller and stress does not change very much between N=0 and N=3 under δ/d =1.0×10^{-3}.

4.7   Conclusions

This study dealt with failure analysis for coming out of the steel shaft from ceramic sleeve connected by shrink fitting. Here, inner diameter of the sleeve d=240mm is considered. Only low shrink fitting ratio can be applied because of the brittleness of the ceramic sleeve. In this study, the coming out behavior of the roller during rotation was analyzed by the finite element method. The conclusions can be summarized as follows:

1. In the numerical analysis the rotation of the roller under loading is replaced by the non-rotating roller subjected to shifting load in the circumferential direction. As a standard method of discretization in numerical analysis, the continuous load shifting can be replaced by discrete load shifting with less than 1% error if the load shifting interval angle $\theta_0 \leq 12°$.

2. It is confirmed that the inertial force can be neglected and the quasi-static analysis presented in this study is accurate enough.

3. The coming out of the shaft can be realized by numerical simulation. The coming out of the shaft appears under smaller shrink fitting ratio $\delta/d \leq 0.2 \times 10^{-3}$ and does not appear under larger shrink fitting ratio $\delta/d \geq 0.4 \times 10^{-3}$ as shown in Figure 4.15.

4. The coming out happens easily for smaller Young's modulus of the shaft $E_{sh} \leq$ 100GPa, smaller friction coefficient $\mu \leq 0.1$, and larger distributed load $w \geq 45$N/mm.

5. The speed of coming out can be prevented by increasing thickness of the shaft t $\geq$ 20mm in Figure 4.21 and contact length $L \geq 300$mm as shown in Figure 4.22.

6. The shear contact stress is changed largely between N=0 and N=3 if the coming out happens, and does not change very much if no coming out. The shear contact stress change may be useful information to judge the coming out appears or not.

References

[1]   Fujii M, Yoshida A, Ishimaru J, Shigemura S, and Tani K. Influence of sprayed layer thickness on rolling contact fatigue of ceramics sprayed roller, *Transactions of the JSME Series C* 2006; 72(716): 1354-1360. (in Japanese)

[2]   Ono T. Current status and future prospect of the development of high performance ceramics, *Journal of the Japan Society of Mechanical Engineers* 1983; 86(774): 470-475. (in Japanese)

[3]   Liou CR, Mori T, Kobayashi H, Mitamura T. Influence of Various Atmosphere on the Corrosion resistance of Si3N4 sintered bodies against steel making slag and its main components, Journal of Ceramic Society of Japan 1990; 98(4): 348-354.

[4]   Noda NA Hendra, Takase Y, and Tsuyunaru M. Maximum stress for shrink fitting system used for ceramics conveying rollers, *Journal of Solid Mechanics and Materials Engineering* 2008; 2(8): 1410-1419.

[5]   Li W, Noda NA, Sakai H, and Takase Y. Analysis of Separation Conditions for Shrink Fitting System Used for Ceramics Conveying Rollers, *Journal of Solid Mechanics and Materials Engineering* 2011; 5(1): 14-24.

[6]   Li W, Noda NA, Sakai H, and Takase Y. Thermal Stress Analysis for Shrink fitting System used for Ceramics Conveying Rollers in the Process of Separation, *Key Engineering Materials* 2011; 452-453: 241-244.

[7]   Dedi S, Noda NA, Sano Y and Takase Y. Ceramics/steel joint selection for the ceramics roller used at high temperature, *Proceeding of the 4th ACEE 2014*; 221-222

[8]   Harada S, Noda NA, Uehara O, and Nagano M. Tensile strength of hot isostatic pressed silicon nitride and effect of specimen dimension, *Transactions of the JSME Series A* 1991; 57(539): 1637-1642. (in Japanese)

[9]   Ogawa E, Shimizu K, and Hamayoshi S. Practical evaluation of large ceramic rolls for continuous hot dipping steel sheet production line, *Hitachi Metals Technical Review* 2012: 28: 50-55. (in Japanese)

[10]   Noda NA, Yamada M, Sano Y, Sugiyama S, and Kobayashi S. Thermal Stress for All-Ceramics Rolls Used in Molten to Produce Stable High Quality Galvanized Steel Sheets, *Engineering Failure Analysis* 2008; 15(4): 261-274.

[11]   Ogawa E, et al. Development of 100% ceramic pot rolls for continuous hot dip coating lines of the steel sheet, *Proceedings of 8th International Conference on Zinc and Zinc Alloy Coated Steel Sheet* 2011; 6: 1-8.

[12]   Noda NA, Hendra, Oosato M, Suzumoto K, Takase Y, and Li W. Strength Analysis for Shrink Fitting System Used for Ceramics Rolls in the Continuous Pickling Line, *Key Engineering Materials* 2011; 462-463: 1140-1145.

[13]   Matsuda S, Suryadi D, Noda NA, Sano Y, Takase Y, and Harada S. Structural Design for Ceramics Rollers Used in the Heating Furnace, *Transactions of the JSME Series A* 2013; 79(803): 989-999. (in Japanese)

[14]   Truman CE, Booker JD. Analysis of a Shrink-fit Failure on a Gear Hub/Shaft Assembly, *Engineering Failure Analysis* 2007; 14: 557-572.

[15]   Antoni N, Contact Separation and Failure Analysis of a Rotating Thermo-elastoplastic Shrink-fit Assembly, *Applied Mathematical Modelling* 2003; 37: 2352-2363.

[16]   Rusin A, Nowak G, Piecha W. Shrink connection modelling of the steam turbine rotor, Engineering Failure Analysis 2013; 34: 217-227.

[17]   Iron and Steel Institute of Japan. Steel Handbook. pp. 886-887, Tokyo: Maruzen co., Ltd.: 1962

[18]   Timoshenko SP and Goodier JN. Theory of Elasticity. pp. 81-82, Tokyo: McGraw-Hill Kogakusha Ltd.: 1970

[19]   Marc Mentat team. Theory and User Information. Vol. A. pp.532, Tokyo: MSC. Software: 2008.

Chapter 5

Conclusions of Present Study

Ceramic materials have advantageous properties, including capability to withstand high temperatures, strength at high temperature, high melting point, and good mechanical properties such as hardness, elastic modulus, and compressive strength. In this study, we will focus on hearth rollers used in the heating furnace whose atmosphere temperature is more than $1,000^{\circ}C$. Here, a new roller consisting of ceramic sleeve and steel shafts at both ends will be considered. The objectives of this research are: (1) to select appropriate joint for ceramic/metal roller, (2) to design ceramic roller used in the heating furnace, and (3) to investigate effect of the shrink fitting ratio on the coming out of the shaft from the ceramic sleeve as well as some other parameters. The conclusion can be obtained as follows.

(1) In chapter 1, explanation about advanced ceramic material was given briefly including classification and properties of advanced ceramic. The advanced ceramic is divided into five important classes such as Alumina ceramic (Al_2O_3), Zirconia ceramic (ZrO_2), Silicon nitride ceramic (Si_3N_4), Sialon ceramic (SiAlON), and Silicon carbide ceramic (SiC). In present work, Si_3N_4 is considered because Si_3N_4 can be used at high temperature up to $1,500^{\circ}C$. Chapter 1 also provides a review of the recent research on ceramic rolls. The objectives and thesis layout are also available at the end of this chapter.

(2) In chapter 2, appropriate joint selection was considered for ceramic roller used

under room temperature and high temperature. The roller consists of ceramic sleeve and steel shaft subjected to both distributed load and thermal load. Since thermal expansion mismatch between ceramic and steel is a main problem, the appropriate joint method was considered in terms of joint strength. Here, three types joints were investigated, namely, adhesive bonding as Model 1, metal bonding as Model 2, and shrink fitting as Model 3. For Model 1 and Model 2, interlayer material is necessary to be considered to bond ceramic sleeve and steel shaft. Interlayer material used for Model 1 is epoxy, and the one for Model 2 is BA03/WC. For Model 3, ceramic sleeve and steel shaft are connected by shrink fitting with shrink fitting ratio 0.2×10^{-3}. The conclusions can be obtained as following.

1. The stress analysis was investigated for Model 1, 2, and 3 due to distributed load under room temperature. For Model 1, maximum stress σ_r=9MPa appears on the bonding surface, which is smaller than bonding strength of epoxy σ_{al}=55MPa. For Model 2, maximum stress σ_z=100MPa appears on the bonding surface, which is also smaller than bonding strength of BA03/WC σ_z=100MPa<σ_{al}=300MPa. For Model 3, maximum stress σ_θ=34MPa appears on the ceramic sleeve surface. This value is also smaller than allowable stress of ceramic σ_θ=34MPa<σ_{al}=333MPa. It is found that Model 1, 2, and 3 are quite safe under room temperature.

2. Investigation was also conducted for Model 1, 2, and 3 under high temperature. It is found that only shrink fitting as Model 3 can be applied to ceramic roller under high temperature.

(3) In chapter 3, the hearth roller was considered. The roller consists of ceramic sleeve

and steel shaft connected by shrink fitting. Here, shrink fitting ratio $\delta/d=2.0\times10^{-4}$ was used for investigation. Although all ceramic sleeve has high temperature resistance and high corrosion resistance, attention should be paid for the risk of fracture due to the thermal expansion of the steel shaft that is much larger than the one of ceramic. To consider thermal stress approximately, in the first place, a simple double cylinder roller consisting of outer ceramic and inner steel is considered. Then, stress analysis on the joint portion of the real ceramic roller has been conducted by varying geometry of the fitted steel shaft. Finally, an application of ceramic roller to steel manufacturing machinery has also been considered. The conclusions can be summarized in the following way.

1. In order to obtain effect of inner cylinder thickness on the maximum thermal stress σ_θ appearing at contact portion, simple double cylinder model consisting of ceramic outer and steel inner was considered by varying inner cylinder thickness h. It is found that the maximum stress σ_θ can be reduced by using the small thickness of the steel shaft. For example, h=30mm is changed to h=10mm, the maximum stress σ_θ becomes less than the allowable stress of ceramic (see Figure 3.6).

2. Design of a real ceramic roller subjected to both heating load and distributed load was carried out by considering maximum stress and fatigue strength at joint portion. Three models have been investigated, that is, uniform thickness of shaft as Model 1, tapered shaft as Model 2, and short tapered shaft as Model 3. It is found that the maximum tensile stress σ_θ can be reduced by using tapered thickness shaft because of the smaller rigidity at the high temperature portion. It is also found that the plastic deformation of the shaft does not appear

by applying the short tapered shaft geometry on the structure as Model 3.

3. An application of ceramic roller to a real furnace in a steel manufacturing company was considered. The roller consists of three pieces structure, namely, main-sleeve, intermediate-sleeve, and shaft as suggested by company. The advantage of this structure is that the damaged components can be replaced with low cost. It is found that tapered shaft geometry with high chrome steel is suitable to be used in a real furnace because high chrome steel has smaller thermal expansion coefficient, therefore, the maximum compressive stress σ_θ becomes smaller.

(4) In chapter 4, failure analysis for coming out of the steel shaft from ceramic sleeve connected by shrink fitting was investigated. It should be noted that only low shrink fitting ratio can be applied to the roller because of the brittleness of the ceramic sleeve. In this study, effects of some parameter on the coming out behavior of the roller during rotation were studied. The conclusions can be summarized as follows.

1. The coming out of the shaft has been realized by the numerical simulation. In this study, the coming out of the shaft was considered under room temperature because the coming out occurs more easily. The coming out phenomenon is indicated by the z-displacement u_{zC}. In the numerical analysis the rotation of the roller under loading was replaced by the non-rotating roller subjected to moving load w=30N/mm in the circumferential direction. The continuous load shifting could be replaced by discrete load shifting less than 1% error if load shift interval angle $\theta_0 \leq 12^o$. Therefore, for the next simulation, load shifting angle $\theta_0 = 12^o$ was used.

2. Effect of the shrink fitting ratio on the coming out of the shaft was studied. The shrink fitting ratio was considered in the range $\delta/d = 0.01 \times 10^{-3} \sim 1.0 \times 10^{-3}$. It is found that the coming out of the shaft appears under smaller shrink fitting ratio $\delta/d \leq 0.2 \times 10^{-3}$ and does not appear under larger shrink fitting ratio $\delta/d \geq 0.4 \times 10^{-3}$.

3. Effects of some other parameters were also investigated such as Young's modulus of steel shaft, friction coefficient between ceramic sleeve and steel shaft, and distributed loads. By varying values for each parameter, it is found that the coming out happens easily for smaller Young's modulus of the shaft $E_{sh} \leq 100$GPa, smaller friction coefficient $\mu \leq 0.1$, and larger distributed load $w \geq 45$N/mm.

4. In order to prevent the coming out, the effect of shaft geometry was considered by varying fitted shaft thickness t=10mm, t=20mm, and t=40mm as well as fitted shaft length L=120mm, L=150mm, L=240mm, and L=480mm. The results show that z-displacement u_{zC} becomes smaller for larger shaft thickness. It is found that speed of coming out can be prevented by increasing thickness of the shaft t $\geq$ 20mm. Moreover, z-displacement u_{zC} becomes smaller for larger fitted shaft length. In other words, the coming out does not occur when contact length L $\geq$ 300mm.

5. The coming out mechanism was also considered by focusing on the stress distribution along fitted shaft portion. Since it is difficult to obtain the results for large number of cycle N because of large calculation time, it is desirable that the coming out can be judged even when N is small. In this chapter, the stress distribution at fitted shaft surface at N=0 and N=3 was compared and

analyzed. It is found that the shear contact stress changes largely between N=0 and N=3 if the coming out happens, and does not change very much if no coming out. It may be concluded that the shear contact stress change may be useful information to judge the coming out appears or not.